UNIVERSITÀ DEGLI STUDI DI PALERMO
Dipartimento di Fisica e Chimica (DiFC)
S.S.D. Astronomia e Astrofisica (FIS/05)
Dottorato in Scienze Fisiche

SORBONNE UNIVERSITÉ
LERMA - Campus Pierre et Marie Curie
E.D. 127: Astronomie & Astrophysique

Radiation hydrodynamic and magnetohydrodynamic models of plasma flows accreting onto Classical T Tauri Stars

IL DOTTORE
Salvatore Colombo

IL COORDINATORE (Italy)
Prof. Gioacchino Massimo Palma

LA COORDINATRICE (France)
Dr. Florence Durret

TUTORS
Dr. Salvatore Orlando (Italy)
Prof. Chantal Stehlé (France)

CO-TUTOR
Dr. Laurent Ibgui

CICLO XXXII
ANNO CONSEGUIMENTO TITOLO 2019
2019

"A numerically correct solution is often the wrong physical solution"
Mark Krumholz

Contents

List of Figures

List of Tables

Summary

Context

Classical T Tauri Stars (CTTSs) are young low-mass stellar objects that accrete mass from their circumstellar disks. The disks extend internally up to the truncation radius, where the magnetic field is strong enough to lift up the material from the disk plane and to funnel the material forming accretion columns (Koenigl 1991). The funneled plasma falls down onto the star and hits the stellar surface. The impacts generate hot shocks. CTTSs are, also, characterized by high levels of coronal activity, as revealed by X-ray observations (e.g. Favata et al. 2005). This coronal activity is mainly produced by energetic flares.

Aims of this work

In this work we investigated the mass accretion process in CTTSs. We studied if accretion from the disk to the star might occur as a result of a coronal activity, and we analyzed the structure and the dynamics of the accretion column plasma in the impact regions. We developed numerical models that describe: a star-disk system subject to the effects of a coronal activity in proximity of the disk surface; the impact of an accretion column onto the surface of a CTTS.

We investigated if an intense coronal activity due to flares that occur close to the accretion disk may perturb the stability of the inner disk, disrupt the inner part of the disk, and possibly trigger accretion phenomena with mass accretion rates comparable with those observed in CTTSs (Colombo et al. 2019c). To this end, we modeled a magnetized protostar surrounded by an accretion disk through 3D magnetohydrodynamics simulations. The model takes into account the gravity from the central star, the effects of viscosity in the disk, the thermal conduction (including the effects of heat flux saturation), the radiative losses from optically thin plasma, and a parameterized heating function to trigger the flares. We explored cases characterized by a dipole plus an octupole stellar magnetic field configuration and by either different densities of disk or different levels of flaring activity.

As it concerns the study of accretion impacts, we analyzed the effects of radiation emerging from the shock-heated plasma at the base of accretion columns on the structure of the pre-shock downfalling material. To this end, we upgraded a module handling the local thermodynamic equilibrium (LTE) radiation-hydrodynamics (RHD) in the PLUTO code (Mignone et al. 2007, 2012), which we have extended to handle also the non-LTE regime (Colombo et al. 2019a). Then, we investigated if a significant absorption of radiation arising from the shock heated plasma occurs in the unshocked downfalling material, and if it leads to a pre-shock heating of the accreting gas. We developed a radiation hydrodynamics model that describes an accretion column impacting onto the surface of a CTTS (Colombo et al. 2019b). The model takes into account the stellar gravity, the thermal conduction, and the effects of both radiative losses and absorption of radiation by matter in non local thermodynamic equilibrium conditions.

Results

As it concerns the effects of flaring activity on the disk stability, we observed, as a result of the simulated intense flaring activity, the formation of several magnetic loops confining hot plasma that link the star to the disk. All these loops build up a hot extended corona with an X-ray luminosity comparable to typical values observed in CTTSs (Colombo et al. 2019c). The intense flaring activity close to the disk can strongly perturb the disk stability. The flares trigger overpressure waves which travel through the disk and modify its configuration. Accretion funnels may be triggered by the flaring activity, thus contributing to the mass accretion rate of the star. Accretion rates derived from the simulations range from 10^{-10} to $10^{-9} M_{\odot} yr^{-1}$ (Colombo et al. 2019c). The accretion columns can be perturbed by the flares and can interact with each other, possibly merging together in larger streams. As a result, the accretion pattern can be rather complex: the streams are highly inhomogeneous, with a complex density structure, and clumped. This inhomogenity may be the origin of the variability observed in the structure of the accretion columns (Alencar et al. 2018).

The non-LTE radiation module developed to study the dynamics and structure of the impact region of CTTSs has been validated through different tests. In particular, we modeled the structure of a radiative shock, simulating a simple shock case as described by Ensman (1994). The agreement between our solutions and the semi-analytical solutions (when available) is good, with a maximum error of 7%. Moreover, we have proven that a non-LTE approach change significantly the structure and the dynamics of the impact regions, leading to a radiative precursor and a greater extension of the post-shock region compared to the LTE case (Colombo et al. 2019a).

Our radiative model describing the impact of an accretion column onto the stellar chromosphere shows that part of radiation emitted by the post-shock plasma ($\approx$ 70%) is absorbed by the pre-shock accretion column immediately above the slab. The irradiation heats the downfalling unshocked material up to $\approx 10^5$K. This hot material forms a precursor region that emits in the UV band.

The results of this PhD project may address some open questions regarding CTTSs. For instance, we proved that an intense flaring activity in proximity of the disk may perturb its stability and may generate accretion columns highly structured in density and characterized by clumps as recently observed, for example, by Alencar et al. (2018).

Moreover, with our radiation model we may naturally explain the origin of the complex UV spectra arising from impact regions (Ardila et al. 2013) and the fact that accretion rates derived from UV observations are systematically higher than rates inferred from X-ray observations (Curran et al. 2011). In fact, our model predicts the presence of a precursor region emitting in the UV. This region: 1) would increase the UV flux arising from the impact without assuming higher accretion rates and 2) may generate an UV flux produced by plasma at free fall velocity, thus with Doppler shifts stronger than those generated by the post-shock plasma. This may explain the high redshifts and broadening observed in emission lines of UV spectra (Ardila et al. 2013).

Résumé

Contexte

Les étoiles T Tauri classiques (CTTSs) sont des objets stellaires jeunes et de faible masse qui accrètent de la matière de leur disque circumstellaire. Le disque s'étend jusqu'au rayon de troncature où le champ magnétique est suffisamment fort pour extraire la matière et la canaliser pour former des colonnes d'accrétion. Le plasma ainsi canalisé vers l'étoile tombe sur la surface stellaire. L'impact génère un choc. Les CTTSs sont aussi caractérisées par une activité coronale importante, comme révélé par les observations dans le domaine des X (Favata et al. 2005). Cette activité coronale est principalement produite par des éruptions de haute énergie.

Objectif de ce travail

Nous avons étudié le processus d'accrétion dans les CTTSs. D'une part, nous avons examiné la possibilité que l'accrétion du disque vers l'étoile résulte de l'activité coronale; d'autre part, nous avons analysé la structure et la dynamique du plasma de la colonne d'accrétion au niveau de l'impact sur la surface stellaire. Nous avons développé des modèles numériques qui décrivent: un système étoile – disque sous l'influence d'une activité coronale au voisinage de la surface du disque; la zone d'impact d'une colonne d'accrétion sur la surface d'une CTTS.

Nous avons examiné si une activité coronale intense, créée par les éruptions au voisinage du disque d'accrétion, pouvait perturber la stabilité du disque interne, déstabiliser cette zone interne, et éventuellement déclencher des phénomènes d'accrétion à des taux d'accrétion comparables à ceux déduits des observations (Colombo et al. 2019c). Pour cela, nous avons modélisé une protoétoile magnétisée entourée par un disque d'accrétion, à l'aide de simulations 3D de magnétohydrodynamique. Le modèle prend en compte la gravité de l'étoile, les effets de viscosité dans le disque, la conduction thermique (y compris les effets de saturation de flux), les pertes radiatives du plasma optiquement mince, et une fonction de chauffage paramétrable pour permettre le déclenchement des éruptions. Les cas que nous avons explorés sont caractérisés par un champ magnétique stellaire composé d'un dipôle et d'un octopôle, avec, ou bien différentes densités du disque, ou bien différents niveaux de l'activité éruptive.

Lors de notre étude de la zone d'impact de la colonne, nous avons analysé l'effet du rayonnement, produit par le plasma chauffé par le choc d'accrétion, sur la structure de la matière en chute en amont du choc. Pour cela, nous avons perfectionné un module d'hydrodynamique radiative initialement implémenté dans le code PLUTO (Mignone et al. 2007, 2012) dans l'hypothèse de l'équilibre thermodynamique local (ETL) (Kolb et al. 2013). Nous avons étendu ce module pour qu'il puisse gérer un régime hors ETL (Colombo et al. 2019a). Ensuite, nous avons étudié si la partie de la colonne d'accrétion en amont du choc pouvait absorber de façon significative le rayonnement créé par la partie de la colonne en aval du choc, de telle sorte que cela puisse créer un pré-chauffage de la colonne en amont du choc. Nous avons développé un modèle d'hydrodynamique radiative décrivant une colonne d'accrétion et son impact sur la surface d'une CTTS (Colombo et al. 2019b). Le modèle prend en compte la gravité stellaire, la conduction thermique, ainsi que les pertes radiatives et l'absorption du rayonnement par la

matière dans des conditions hors ETL.

Resultat

L'étude des éruptions stellaires et leur incidence sur la stabilité du disque circumstellaire a mis en évidence la formation de plusieurs boucles magnétiques confinant le plasma chaud qui relie le disque à la surface stellaire. Ces boucles s'accumulent pour former une couronne chaude étendue dont la luminosité dans le domaine des X est comparable aux valeurs typiques observées dans les CTTSs (Colombo et al. 2019c). L'activité éruptive intense au voisinage du disque peut fortement perturber sa stabilité. Les éruptions déclenchent des ondes de surpression qui se propagent dans le disque et modifient sa configuration. Des colonnes d'accrétion peuvent alors être créées, et donc contribuer à l'accrétion de matière sur l'étoile. Nous avons déduit de nos simulations des taux d'accrétion variant de 10^{-10} à 10^{-9} $M_{\odot}yr^{-1}$ (Colombo et al. 2019c). Les colonnes d'accrétion peuvent être perturbées par les éruptions et peuvent interagir entre elles et éventuellement fusionner pour former des colonnes plus larges. En conséquence, le schéma d'accrétion peut être assez complexe: les colonnes sont fortement inhomogènes, avec des structures de densité complexes, et forment des agrégats. Une telle inhomogénéité pourrait être à l'origine de la variabilité observée dans la structure des colonnes d'accrétion (Alencar et al. 2018).

Le module non-ETL développé pour étudier la dynamique et la structure de la zone d'impact à la surface d'une CTTS a été validé par plusieurs tests. En particulier, nous avons modélisé la structure d'un choc radiatif, dans la configuration simple décrite par Ensman (1994). Notre modèle est en bon accord avec les solutions semi-analytiques (lorsqu'elles existent) à 7% près. De plus, nous avons prouvé qu'une approche non-ETL change de façon drastique la structure et la dynamique de la zone d'impact, avec la création d'un précurseur radiatif et une extension plus importante de la zone post-choc en comparaison avec le cas á l'ETL (Colombo et al. 2019a). Selon notre modèle, une partie ($\approx 70\%$) du rayonnement émis par le plasma de la zone post-choc est absorbée par la zone pre-choc située juste en amont du choc. Cette zone est alors chauffée à une température de l'ordre de 10^5 K, formant ce que l'on appelle un précurseur radiatif qui émet dans le domaine UV.

Les résultats de ce travail de thèse peuvent permettre d'aborder des questions ouvertes ayant trait aux CTTSs. Par exemple, nous avons prouvé qu'une activité éruptive intense au voisinage du disque peut perturber sa stabilité et générer des colonnes d'accrétion fortement structurées en densité et regroupées sous forme d'agrégats, en accord avec les observations récentes par (Alencar et al. 2018).

Par ailleurs, il sera peut-être possible, à partir de notre modèle d'hydrodynamique radiative, d'expliquer l'origine des spectres UV complexes observés provenant des zones d'impact (Ardila et al. 2013), ainsi que la raison pour laquelle les taux d'accrétion obtenus à partir des observations UV sont systématiquement plus grands que ceux déduits des observations dans les X (Curran et al. 2011). En effet, notre modèle prédit la présence d'un précurseur émettant dans l'UV. Ainsi, une telle structure: 1) accroît l'émission UV en provenance de la zone d'impact

sans besoin de supposer un plus grand taux d'accrétion; 2) génère un rayonnement UV produit par du plasma à la vitesse de chute libre, créant ainsi des décalages Doppler plus importants que ceux générés par le plasma du post-choc. Ceci peut expliquer les composantes à fort décalage, vers le rouge, observés dans les spectres UV (Ardila et al. 2013).

Sommario

Contesto scientifico

Le stelle T Tauri classiche (CTTSs) sono oggetti stellari giovani poco massivi che accrescono massa dal loro disco circumstellare. Il disco si estende internamente fino al raggio di troncamento, ovvero dove il campo magnetico è abbastanza intenso da sollevare il materiale dal piano del disco e da incanalarlo formando delle colonne di accrescimento (Koenigl 1991). Il materiale incanalato precipita sulla stella e impatta sulla superficie stellare. Gli impatti generano shocks caldi. Le CTTSs sono anche caratterizzate da un alto livello di attività coronale, come rivelato dalle osservazioni in banda X (e.g. Favata et al. 2005). Questa attività coronale è prodotta principalmente da flares energetici.

Obiettivo di questo lavoro

In questo lavoro abbiamo investigato il processo di accrescimento di massa nelle CTTSs. Abbiamo studiato se l'accrescimento dal disco puó essere il risultato di un' attività coronale e abbiamo analizzato la struttura e la dinamica della colonna di accrescimento nella regione di impatto. Abbiamo sviluppato modelli numerici che descrivono: un sistema stella disco sotto gli effetti di un'attività coronale in prossimità della superficie del disco; l'impatto di una colonna di accrescimento su una CTTS.

Abbiamo investigato se un'intensa attività coronale causata da flares che avvengono in prossimità del disco di accrescimento puó perturbare la stabilità del disco interno, distruggere la parte interna del disco e possibilmente innescare fenomeni di accrescimento con tassi di accrescimento confrontabili con quelli osservati nelle CTTSs (Colombo et al. 2016). A tal fine, abbiamo sviluppato delle simulazioni 3D magnetoidrodinamiche di una protostella magnetizzata circondata da un disco di accrescimento. Il modello considera gli effetti della gravità della stella, della viscosità nel disco, della conduzione termica (considerando pure gli effetti della saturazione del flusso), delle perdite radiative da parte di plasma otticamente sottile e una funzione parametrizzata per descrivere i flares. Abbiamo esplorato casi caratterizzati da una configurazione di campo magnetico stellare costituita da un ottupolo più un dipolo e da diverse densità o differenti livelli di attività di flaring.

Per quanto riguarda lo studio degli impatti di accrescimento, abbbiamo analizzato gli effetti della radiazione emergente dal plasma riscaldato dallo shock sulla struttura del materiale pre-shock in caduta. A tal fine abbiamo aggiornato un modulo radiativo implementato nel codice PLUTO (Mignone et al. 2007, 2012) che assume il regime termodinamico locale (LTE). Il modulo è stato generalizzato anche al caso non-LTE (Colombo et al. 2019a). Abbiamo studiato se la radiazione emergente dalla regione di shock viene significativamente assorbita dal materiale ancora non scioccato in caduta libera, e se questo assorbimento puó generare un riscaldamento del materiale pre-shock. Abbiamo sviluppato un modello radiativo magnetoidrodinamico che descrive una colonna di accrescimento che impatta sulla superficie di una CTTS (Colombo et al. 2019b). Il modello considera gli effetti della gravità della stella, della conduzione termica, delle perdite radiative e anche dell'assorbimento della radiazione dal ma-

teriale nel regime non-LTE.

Risultati

Per quanto riguarda gli effetti sulla stabilità del disco dell'attività di flaring, abbiamo osservato, come risultato delle simulazioni di una attività flaring intensa, la formazione di diverse loops di plasma caldo confinate dal campo magnetico che collegano la superficie della stella al disco. Tutte queste loops costituiscono una calda corona estesa che produce una luminosità in banda X confrontabile con i valori tipici osservati nelle CTTSs (Colombo et al. 2019c). L'intensa attività di flaring vicina al disco puó perturbarne significativamente la stabilità. I flares generano un'onda di pressione, la quale viaggia attraverso il disco e ne modifica la configurazione. In questo modo, delle colonne di accrescimento vengono generate dall'attività di flaring, contribuendo cosi al rate di accrescimento sulla stella. I rates di accrescimento derivati dalle simulazioni assumono valori compresi tra 10^{-10} e 10^{-9} $M_{\odot}yr^{-1}$ (Colombo et al. 2019c). Le colonne di accrescimento possono essere perturbate a loro volta dai flares e interagiscono l'una con l'altra, fondendosi per formare colonne più grandi. Il risultato di questa dinamica è che le colonne di accrescimento hanno una struttura molto disomogenea, costituita da blob densi. Questa disomogeneità potrebbe essere l'origine della variabilità osservata nelle strutture di accrescimento (Alencar et al. 2018).

Il modulo radiativo in non-LTE che è stato sviluppato per studiare le dinamica e la struttura della regione d'impatto nelle CTTSs è stato validato utilizzando diversi test. In particolare, abbiamo realizzato un modello per analizzare la struttura di un semplice shock radiativo come descritto da Ensman (1994). Le nostre soluzioni sono in accordo con le soluzioni semi-analitiche (quando disponibili) con una discrepanza massima del 7%. Inoltre, abbiamo provato che un approccio in non-LTE cambia significativamente la struttura e la dinamica della regione di impatto, dando origine ad un precursore radiativo e ad una maggiore estensione della regione post-shock rispetto al caso LTE (Colombo et al. 2019a).

Il nostro modello radiativo, che descrive la regione di impatto di una colonna di accrescimento sulla cromosfera stellare, prova che parte della radiazione emessa dal plasma post-shock ($\approx 70\%$) viene assorbita dal materiale freddo pre-shock in caduta sulla stella. L'irraggiamento riscalda il materiale, in caduta sulla stella, ancora non scioccato fino a temperature di 10^5K. Il materiale caldo forma un precursore termico che emette nella banda UV.

I risultati di questo progetto di dottorato potrebbero aiutare nella soluzione di alcune questioni aperte sulle CTTSs. Per esempio, abbiamo provato che un'intensa attività di flaring in prossimità del disco puó perturbarne la stabilità e generare colonne di accrescimento con una forte strutturazione in densità come quelle recentemente osservate da Alencar et al. (2018).

Inoltre, utilizzando il nostro modello radiativo possiamo spiegare naturalmente l'origine dei complessi spettri in banda UV provenienti dalle regioni di impatto (Ardila et al. 2013) e anche il fatto che i rates di accrescimento ottenuti dalle osservazioni in banda UV sono sistematicamente più grandi di quelli ottenuti in banda X (Curran et al. 2011). Infatti, il nostro modello radiativo predice la presenza di un precursore termico che emette in banda UV. Questo pre-

cursore: 1) Aumenterebbe il flusso UV prodotto dalla regione di impatto senza assumere un più alto rate di accrescimento e 2) potrebbe generare un flusso UV prodotto da plasma a velocità di caduta libera sulla stella, quindi con Doppler shifts molto più grandi di quelli generati dalla regione post-shock. Questo potrebbe spiegare le componenti ad alto redshift osservate in banda UV (Ardila et al. 2013).

CHAPTER I

Introduction

Stars are the fundamental constituents of the universe, they are responsible for the production of all the elements and, in some peculiar cases, they also give birth to life.

In this chapter, we introduce briefly the star formation theory. We explain the different stages of evolution of young stellar objects. Then, we describe the most important features of CTTSs. We review the magnetospheric accretion scenario and all the results obtained from the modeling of these systems. In the last part of this chapter, we discuss the motivations of this work and we give an outline of this manuscript.

I.1 Star formation theory

Stars form from the gravitational collapse of cold massive clouds. These clouds are mainly composed of molecular hydrogen, they are rarefied with typical density of $\approx 10^4$ cm^{-3} and cold, at temperatures $\approx$ 10 K. Initially, a cloud is in equilibrium between gravity and the forces that prevent the collapse (such as thermal pressure and turbulence). When the equilibrium breaks, the cloud starts to collapse under the effect of gravity. The collapse causes the fragmentation of the cloud in smaller molecular cores that cover a wide range of masses, and from which one or more stars can form.

Star formation theory is, typically, divided in high mass ($M_\star > 8M_\odot$) and low mass stars. The former form more rapidly and they dissipate the surrounding environment in around 10^6 yr. The latter spend more time in the pre-main sequence (PMS) evolution (more details in McKee & Ostriker 2007). In this work we focused on formation of low-mass stars

According to the virial theorem a cloud is in equilibrium if

$$2K + U = 0 \tag{I.1}$$

where

$$U = -\frac{3GM^2}{5R} \tag{I.2}$$

is the potential energy, G is the gravitational constant, M the cloud mass, R the cloud radius, and

$$K = \frac{3}{2}Nk_BT = \frac{3Mk_BT}{2\mu m_H} \tag{I.3}$$

is the kinetic thermal energy, where N is the number of particles, k_B the Boltzman constant, T is the cloud temperature, μ the mean molecular weight of the cloud, and m_H the hydrogen mass.

The cloud collapses if $2K + U < 0$. This condition is verified if the radius R of the cloud with a mass density ρ is smaller than the so-called Jeans radius R_j, i.e.

$$R < R_j = \sqrt{\frac{15 k_B T}{4\pi G \rho \mu m_H}} \tag{1.4}$$

or, analogously, if the total mass of the cloud overcomes the Jeans mass M_j given by:

$$M_j = \frac{5}{2}\sqrt{\frac{15}{\pi\rho}}\left(\frac{k_B T}{\mu m_H G}\right)^{3/2} \tag{1.5}$$

From Eq.(1.4) and (1.5) it is clear that, for higher density, the collapse occurs for a smaller cloud mass or for a smaller radius. A cloud in equilibrium can be compressed by an external source, such as a close supernova explosion, and begins the gravitational collapse. During the collapse, the density of the cloud increases, but the temperature remains constant due to efficient mechanisms of cooling by emission in the infrared band. Inside the cloud, the critical Jeans mass value decreases and smaller regions of the cloud overcome it, and start to collapse individually. The result of this dynamics is a region with several new stars called cluster.

1.2 CLASSIFICATION OF YOUNG STELLAR OBJECTS

During the collapsing phase of the cloud and the formation of the star, we can define four different intermediate stages. Here, I will summarize the most important characteristics of these phases, for a more exhaustive description please refer to Feigelson & Montmerle (1999).

Fig. 1.1 shows the four phases of stellar formation. Initially, the protostar is surrounded by a massive and cold collapsing cloud. From the cloud, due to conservation of angular momentum, a protodisk starts to form. These objects are extremely weak in optical and near-IR emission, while they are strong sources in sub-millimeter, because the protostar is completely embedded into the cloud which absorbs most of the radiation. These objects are called Class 0 objects (see Fig. 1.1).

Class I objects (see Fig. 1.1) are the consequence of the evolution of Class 0 objects. In these systems the protostar is more evolved and most part of the surrounding cloud accretes onto the star or onto the disk. However, the envelope that surrounds the star is optically thick, the radiation arising from these objects is mainly produced by the dust and the protostellar disk. In this phase the disk starts to accrete onto the star, and outflows develop.

During the Class II phase (see Fig. 1.1) the mass of the star is a few percents less than the final mass. The envelope of gas and dust is dispersed through winds and outflows or is accreted onto the star or onto the disk. The star is visible and the emission is mainly composed of a black body part plus an infrared (IR) excess due to the disk that is heated up by the irradiation from the central star. These objects are also called CTTSs.

Class III objects are the last stage of evolution (see Fig. 1.1). The envelope is completely gone, and the star does not show any sign of accretion or outflow. The emission is that of a black body originating from the central star.

The PhD project focused on accretion phenomena in class II objects or CTTSs.

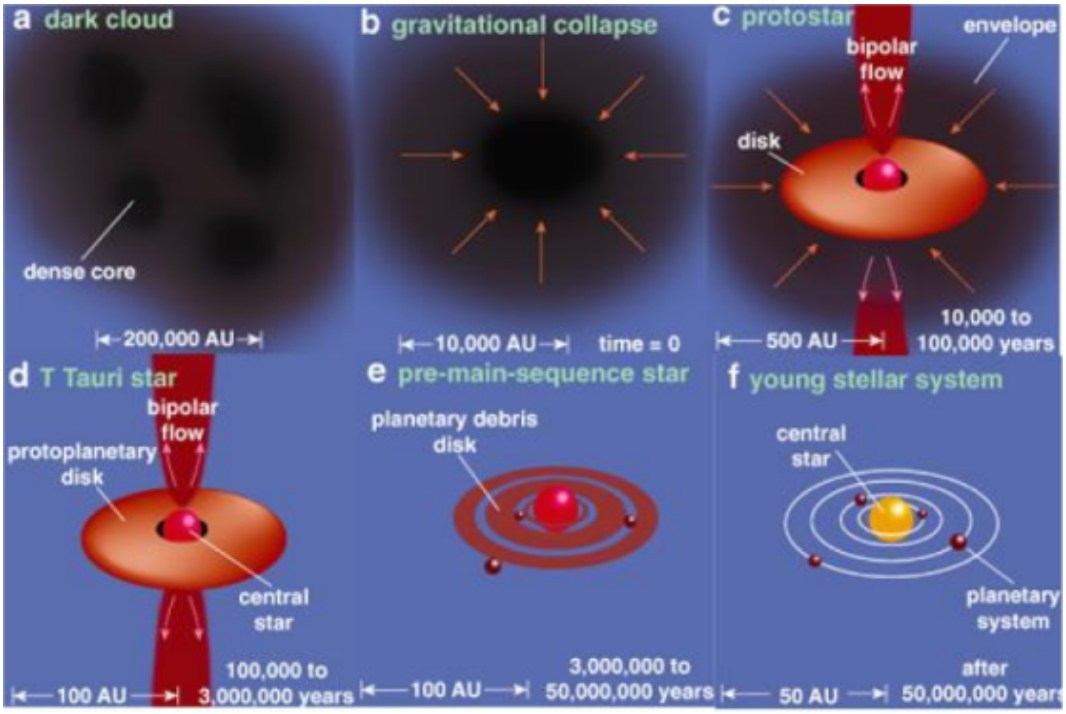

Figure 1.1 – Schematic evolution of YSOs. The picture shows the process of star formation. Initially, the dark cloud is composed of several dense cores (Panel a). Each of them collapses under the effect of gravity and the temperature of the core increases forming a class 0 object (panel b). Then part of the cloud is dispersed, collapses onto the star or forms a disk, this phase is called class 1 object (panel c). When the cloud is completely disappeared, it remains a star surrounded by a dense disk called class 2 objects or CTTS (panel d). The disk material accrete onto the star or forms planets. The planetary debris disk and the star form a class 3 object (panel e). The evolution of this system results in a young stellar system (panel f). Credit: Greene, American Scientist, (Jul-Aug 2001).

1.3 Classical T Tauri stars

CTTSs are pre-main sequence stars that have consumed the opaque envelope from their parent cloud, and that show strong emission lines in their spectra. A variety of different phenomena occur in these objects. Fig. 1.2 illustrates a typical star-disk system.

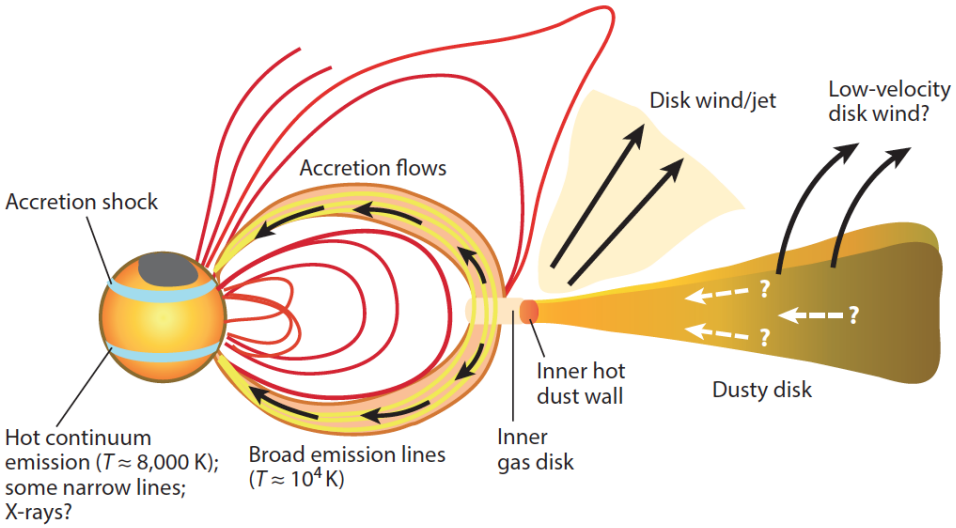

Figure 1.2 – Schematic view of a typical classical T Tauri star. The disk extends internally up to the truncation radius (some stellar radii), where it is disrupted by the magnetic field originating from the star ($\approx$ 1kG at the stellar surface; Donati et al. 2007). Jets and winds can be launched from the star and the disk. The disk plasma accretes onto the star, funneled by the magnetic field, forming accretion columns. Credit: Hartmann et al. (2016).

The obscuration shown by most CTTSs was originally attributed to an unaccretted cloud of dust around the object. However, the millimiter emission proved unambiguously the presence of a optically thick disk (Lada 1987; Andre & Montmerle 1994). Nowadays, these protoplanetary disks can be directly imaged with millimeter interferometers, like the Atacama Large Millimeter Array (ALMA) observatory (see an example in Fig. 1.3).

CTTSs interact with their disks exchanging mass and angular momentum. Understanding the physics of disks is extremely important. Among other things, they represent the initial and boundary conditions for the whole process of planet formation. In fact, it is expected that planets form inside the disks, accreting material from the disk (Boss 1997).

Outflows in the forms of jets and winds originate from the disk. These outflows are confined and accelerated by the magnetic field (Feigelson & Montmerle 1999). However the detailed mechanism of acceleration is still subject of discussion and is beyond the purpose of this PhD project. Outflows play a crucial role in carrying away angular momentum from the system.

1.3.1 The Magnetospheric Accretion Scenario

The disk rotates with Keplerian velocity around the central star. According to the largely accepted magnetospheric accretion scenario (Koenigl 1991), the disks of CTTSs extend internally up to the so-called truncation radius. In this region, the magnetic field of the star is

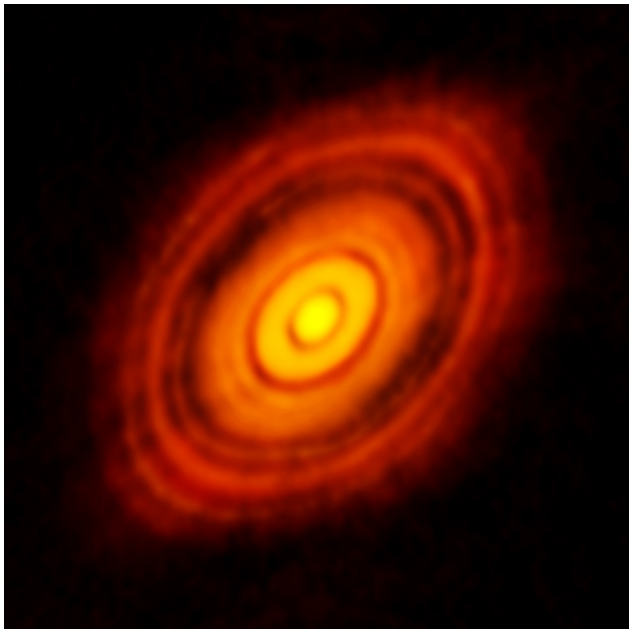

Figure 1.3 – Protoplanetary disk surrounding the young star HL Tauri. This submillimeter image shows the disk structure (red to yellow scale). The black orbits show the inhomogeneity of the disk density possibly due to planetary formation. Credit: ALMA (ESO/NAOJ/NRAO).

sufficiently strong to truncate the accretion disk. At this radius, the magnetic pressure and the ram pressure of the disk material balance. This leads to $B^2/8\pi \approx \rho \mathbf{u}^2$, where B represent the magnetic field strength, ρ the mass density, and $\mathbf{u}$ the Keplerian velocity of the plasma. The truncation radius can be estimated assuming a dipolar magnetic field

$$R_T \approx \xi \left(\frac{\mu_B^4}{4GM_\star \dot{M}^2} \right)^{1/7} \tag{1.6}$$

where μ_B is the dipole moment of the star, $\xi \lesssim 1$ is a correction factor dependent on the system (Hartmann et al. 2016), G is the gravitational constant, $M_\star$ the stellar mass, and $\dot{M}$ the mass accretion rate. Using fiducial numbers (i.e. $M_* \approx 0.8 M_\odot$, $R_* \approx 2 M_\odot$, $B \approx 1$kG at the stellar surface), one finds that the truncation radius is of the order of a few stellar radii (Hartmann et al. 2016). The material, funneled by the magnetic field, forms the so-called accretion columns: the material falls onto the star at free fall velocity and hits the stellar surface generating hot shocks.

Several observational lines of evidence support this scenario. For example, Bertout et al. (1988); Bouvier et al. (2007) observed a sample of CTTSs and found evidence of hot material ($T \approx 10^6$ K) moving with velocities of the order of a few hundreds km/s. Some T Tauri stars show optical and IR spectra with absorption lines that present Doppler shifts compatible with material moving at hundreds km/s (e.g. Ardila et al. 2013). Edwards et al. (1994) observed a

sample of 15 CTTSs and found that, in 13 cases, the lines were characterized by Doppler shifts compatible with material accreting onto the star. The fact that some CTTSs do not show these features does not go against the model. The redshift is visible only if the accretion column is aligned with the line of sight.

Accretion signatures are also visible in the soft X-ray bands [0.2 - 0.8]keV, and UV. In particular, these systems show lines produced by material with density $n \geqslant 10^{11}$ cm^{-3} and temperatures between a few 10^5 and a few 10^6K (e.g. Kastner et al. 2002; Argiroffi et al. 2007). According to the magnetospheric accretion model, this emission is produced by the conversion of kinetic energy to thermal energy in the accretion shock. The shock is generated by the impact onto the stellar surface of the accretion column that heats the plasma up to $T > 10^6$ K producing X-ray emission (Kastner et al. 2002; Argiroffi et al. 2007).

1.3.2 Coronal Activity

CTTSs are also strong X-ray emitters (Feigelson & Montmerle 1999; Favata & Micela 2003). This emission originates mainly from an intense coronal activity. In particular, observations show that CTTSs present an X-ray luminosity, in general, 3-4 orders of magnitude higher than in the solar case (Getman et al. 2005; Favata et al. 2005; Audard et al. 2007; Getman et al. 2008a,b). Part of this X-ray emission comes from the heated plasma in the outer part of the stellar corona with temperatures from 1 to 100 MK. The plasma heating is correlated with the presence of magnetic field and might be, in particular, due to strong magnetic activity (Feigelson & Montmerle 1999; Favata & Micela 2003) in the form of high energetic flares that are generated from a quick release of energy in proximity of the stellar surface. A flare is a sudden brightening of individual coronal structures followed by a decay (e.g. Reale 2003). The X-ray emission produced by the flares may dominate the emission from the rest of the corona. In the solar case, flares typically decay in minutes or hours (Reale 2003). In CTTSs the brightest flares decay in several days (Favata & Micela 2003).

During the *Chandra Orion Ultradeep Project* (COUP) observing campaign, the *Chandra* X-ray observatory revealed numerous flares in the Orion star-forming region (Favata et al. 2005; Getman et al. 2008a,b), some of which reached temperatures of $\approx$ 100 MK. The analysis of these flares revealed that they are long-lasting ($\approx$ 100 ks) and apparently confined to very long (several stellar radii) magnetic structures that may connect the disk surface to the stellar photosphere (e.g. Favata et al. 2005; López-Santiago et al. 2016).

From the theoretical point of view, bright flares might be generated by reconnection of magnetic field lines in proximity of the disk surface, as is often observed in local and global magnetorotational instabilities (MRI) simulations of accretion disks (e.g. Miller & Stone 2000; Romanova et al. 2011b), or by the inflation of the field lines that connect a star with the inner disk, as suggested by other authors (e.g. Goodson et al. 1997, 1999; Bessolaz et al. 2008). More recently, Reale et al. (2018) used accurate hydrodynamic simulations of flares confined to magnetic flux tubes to unambiguously prove that some of the flares observed during COUP campaign are confined to loops that extend over several stellar radii and possibly connect the

protostar to the disk. Fig. 1.4 shows the scenario proposed by Reale et al. (2018) of the flaring magnetic tube in the V772 Ori flare.

If flares originate in proximity of the disks, some effects on the dynamics of the disk are expected. For instance, they may influence the disk stability with possible consequences on the process of mass accretion onto the star.

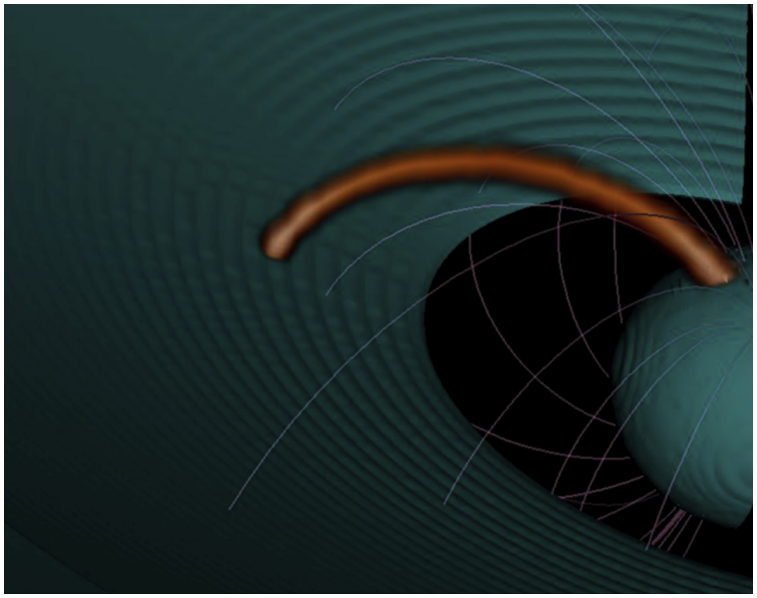

Figure 1.4 – Hot flare confined by magnetic field lines that connects the stellar surface to the disk. The temperature of the flare is showed in red to orange scale. The magnetic field is represented by white lines. The disk and the star are in dark green. Credit: Reale et al. (2018)

1.4 Modeling accretion phenomena in CTTSs

Numerical models are a widely used tool to investigate the accretion phenomenon in CTTSs. The advantage of using models is that they can isolate the effects on the system evolution of all the physical components. Moreover, from numerical models it is possible to synthesize physical quantities, such as spectra, that can be compared with actual observations..

Accurate simulations require to include many physical phenomena such as the viscosity of the disk that allows the material to fall down onto the star, the thermal conduction and effects of absorption and emission of radiation, in order to correctly evaluate the energy balance in the impact regions. Many studies focused on the mechanisms which trigger accretion events from the disk onto the star (e.g. Romanova et al. 2002; Koldoba et al. 2002; Kulkarni & Romanova 2005). Other studies focused on the description of the regions where accretion columns hit the stellar surface. The former studies make use of 2D and 3D magnetohydrodynamic models of star-disk systems, and are able to support with theoretical evidence the magnetospheric

accretion scenario. The others describe the dynamics of the material shock-heated by impacts of accretion columns onto the stellar surface and explain the origin of UV and X-ray emission arising from impact regions.

In this section we review some of the previous numerical models discussed in literature.

1.4.1 MHD modeling of the star-disk system

In the last 20 years, several progresses were made in modeling the star-disk system. The major problem was to find physically reasonable and stable initial conditions that do not affect the dynamics and the evolution of the system. Romanova et al. (2002) developed quasi-equilibrium initial conditions where the material from the disk accretes in a timescale of few hundreds stellar periods. In their axisymmetric 2D MHD simulations, the rate of accretion is regulated by viscosity in the accretion disk (Shakura & Sunyaev 1973).

The disk is truncated at R_T (see Eq. 1.6) by the stellar magnetosphere. The viscosity allows the material to lose angular momentum and to move inward until that region. There the magnetic field from the star is strong enough to prevent the material to move inward through the radial direction. At this point the plasma lifts up from the disk plane due to pressure force. Then it is caught by the gravity of the star and falls down onto the stellar surface, at supersonic velocity, funneled by the magnetic field. The R_T oscillates from the equilibrium position due to the accumulation and reconnection of magnetic field lines that prevent or not the plasma from falling down onto the star. The result of this dynamics is a non-steady accretion through accretion columns. The simulations also show that the funnel flows are quite stable and last up to 1000 stellar periods Long et al. (2005).

The first model able to reproduce the formation of accretion columns and the effects of an extended magnetosphere with production of stellar winds was developed by Zanni & Ferreira (2009). They developed a set of 2D axisymmetric simulations to study the evolution of the angular momentum of the star. In particular, their simulations have shown that the spin-down torques due to stellar winds and due to the interaction of the extended magnetosphere with the outer part of the disk are not sufficient to contrast the spin-up due to accretion. In a further work, Zanni & Ferreira (2013) investigated the role of the outflows in the evolution of angular momentum of the star. In particular, their simulations have shown that the torque due to mass ejection may be significant and, together with a light stellar wind, is able to compensate the acceleration due to accretion.

Several authors have moved further the limits of axisymmetric models by studying cases in which the dipole of the central star is not aligned with the rotational axis (Koldoba et al. 2002; Romanova et al. 2003, 2004b). In cases with a tilted dipole, the disk is still truncated at the truncation radius (as in the axisymmetric cases), but, in this case, the accretion column dynamic is more complex. As for the 2D case, matter flows along the magnetosphere and hits supersonically the stellar surface. However, for a tilted dipole case, 3D simulations of star-disk systems have shown that the dynamics and morphology of accretion structures strongly depend on θ, i.e., the angle between the star magnetic dipole and the rotational axis of the

star-disk system (Romanova et al. 2004b). Matter typically accretes in two main streams, but for cases with θ close to 90 deg, they can be more numerous (Koldoba et al. 2002; Romanova et al. 2003, 2004b). In the accretion columns, the density and the pressure vary towards the star due to the funneling of the material by the magnetic field and due to accretion column dynamics. In general, density and pressure are higher in the center of an accretion column than in its outer part. Fig. 1.5 shows the high and low density parts of the accretion columns for a case with $\theta = 30°$.

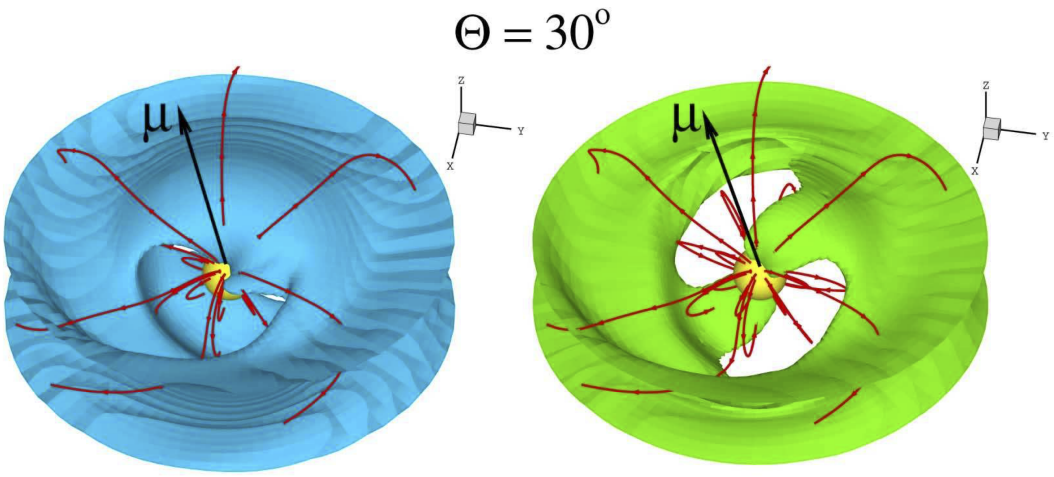

Figure 1.5 – 3D simulations of a star-disk system with tilted dipole. The figure shows the low density funnel flows (on the left) that surround the high density flows (on the right), in the case of $\theta = 30°$. (Credit: Bouvier et al. 2007)

Simulations focusing on the inner disk region have shown that the magnetosphere-disk interaction is non-stationary. The inner disk oscillates around R_T (or the truncation radius) and matter accretes and outflows quasi-periodically (Goodson et al. 1997, 1999; Hirose et al. 1997; Romanova et al. 2004a; von Rekowski & Brandenburg 2004; Romanova et al. 2005). It was suggested that this interaction may result in a production of X-ray flares (Hayashi et al. 1996; Feigelson & Montmerle 1999). The idea is that the motion of the disk may drag the magnetic field lines and generate magnetic reconnection close to the disk surface.

The idea of flares in proximity of a disk surface is not new, in fact this scenario is commonly accepted in the case of cataclysmic variables (CVs). Lightcurves of CVs exhibit burst and flares with no periodicity. Several studies have shown that this flickering originates in the inner region of the accretion disk (Hellier 2001; Horne & Stiening 1985; Bruch 2015). The turbulence of the disk is driven by the magneto-rotational instabilities (MRI), and this phenomenon may lead to magnetic reconnection. Some authors suggested that an extended corona can be built up and sustained on the disk through magnetic energy release due to magnetic reconnection (Beloborodov 1999; Malzac et al. 2001). Moreover, simulations of accretion onto magnetized

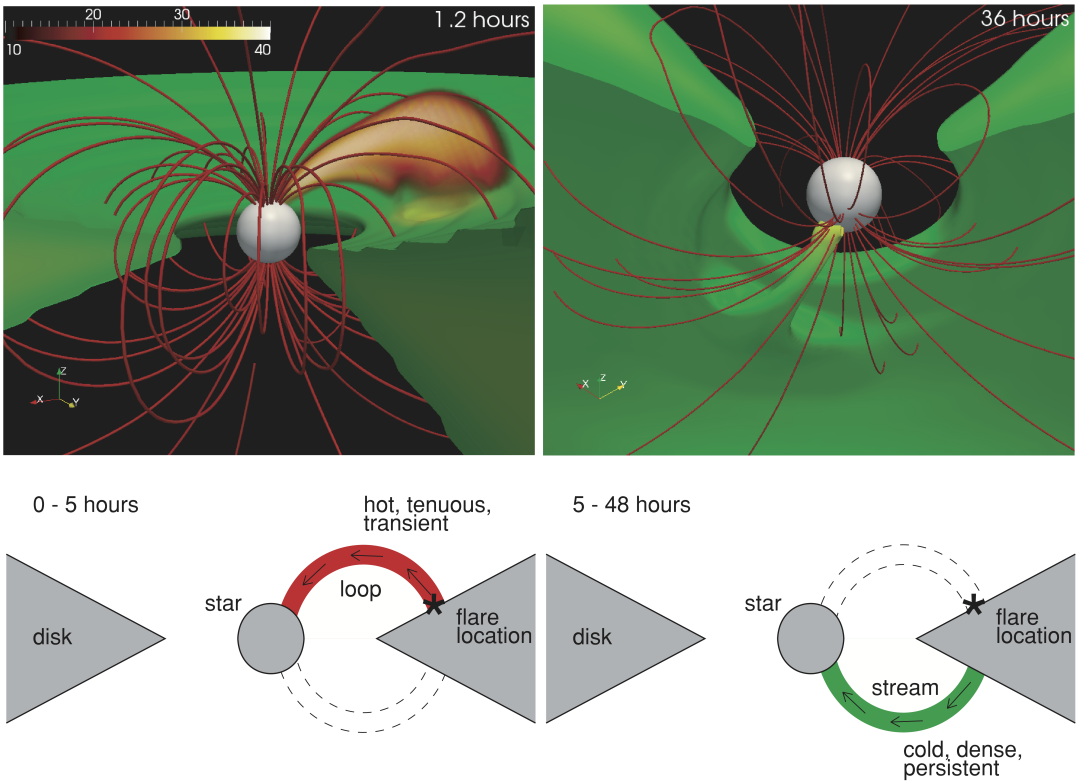

Figure 1.6 – Evolution of a flare and subsequent accretion column. On top left: cutaway view of the star-disk system after 1.2 hours of evolution. On top right: opposite view of the system after 36 hours of evolution. The mass density is represented in green. The bottom panels show a schematic view of the system during the evolution. On the left: the evolution of the hot loop. On the right: the accretion stream. Credit: Orlando et al. (2011)

stars from an MRI-driven disk show the formation of an extended corona (Romanova et al. 2011b).

Observations of flares in CTTSs during the Chandra Orion Ultradeep Project (COUP) were reported by Favata et al. (2005). In particular, the comparison of the brightest flares with the models suggests that these flares are likely hosted in very long loops that connect the star to the disk. In such scenario, the brightest flares observed during COUP may be similar to those observed in CVs, and may be responsible for the formation of a hot extended corona in CTTSs.

The effects of a flare, with intensity consistent with those of the brightest flares observed during COUP, on the stability of the disk have been investigated by Orlando et al. (2011). The dynamics is shown in Fig. 1.6. The sudden release of energy generates a flare hosted in a magnetic loop which links the star to the disk. Furthermore, the flare strongly perturbs the disk: part of the material evaporates in proximity of the flaring loop, and an overpressure wave,

generated by the flare, propagates through the disk. As soon as the overpressure wave reaches the opposite side of the disk, the disk material is pushed out from equilibrium position; then it is funneled by the magnetic field, and forms an accretion column that impacts onto the stellar surface.

1.4.2 HD/MHD MODELING OF IMPACT REGIONS

The structure and dynamics of the impact region have been the subject of several studies. The first theoretical model describing impact regions in CTTSs was developed by Calvet & Gullbring (1998). These authors have calculated, with a semi-analytical model, the structure and the spectral energy distribution of the emission arising from the impact region. Their model was able to reproduce the main features of CTTSs revealed in optical and infrared observations. However, this model does not describe the time evolution of the impact region, and misses the dynamics of the accreting plasma.

In the last 15 years, several hydrodynamic (HD) and magnetohydrodynamic (MHD) models were developed to describe in detail the dynamics and the structure of impact regions. The first type of models were used to describe cases where the plasma parameter β (i.e., the ratio between the thermal pressure of the plasma and the magnetic pressure) is $\beta << 1$, i.e. cases in which magnetic field is so intense (hundreds of Gauss) that it constrains the plasma to move and transport energy along the magnetic field lines. As a result, the structure of impact region is composed of elementary streams with similar physical characteristics which evolve independently one from each others. The whole system evolution can be described by following the temporal evolution of one of the streams, using simple 1D HD models. These models show that an accretion column hits the stellar surface and sinks down into the chromosphere to the position where the thermal pressure of the chromosphere equals the ram pressure of the accreting material. Then the accretion column stops and two shocks develop: a forward shock traveling through the chromosphere, and a reverse shock traveling through the accretion column. The latter propagates and heats the accreting material up to a few 10^6 K. During this phase, the material piles up at the base of the post-shock region, where the radiative losses (that depend on the density) increase. The hot slab of post-shock accreting material expands upward until the radiative losses are high enough to trigger thermal instability at the base of the slab. Thus the base rapidly cools down, and is not able to sustain the post-shock plasma above. As a result, the whole slab collapses. Then a new slab forms again and the process of expansion and collapse are repeated again. This succession of expansions and collapses of the slab generates quasi-periodic oscillations (QPOs) of the shock.

Despite the assumptions and simplifications on the geometry, structure and physical conditions of the system, 1D models were able to describe the dynamics of the impact region and to reproduce the X-ray spectra of the CTTS MP Mus (Sacco et al. 2008). Moreover, they identified the physical conditions required to produce detectable X-ray emission arising from the post-shock regions (Sacco et al. 2010): X-ray emission can be detected only if the accretion column has a density $n \leqslant 10^{11}\mathrm{cm}^{-3}$ and an impact speed $u \geqslant 300$km/s. A denser accre-

tion column sinks deeper into the chromosphere, and generates a thin post-shock region. As a result, a non-negligible part or even all the radiation is absorbed by the dense surrounding chromosphere of the star (Günther et al. 2007; Bonito et al. 2014; Revet et al. 2017) A slower stream generates a post-shock region too cold to emit in the X-ray band.

Although 1D models predict QPOs, they have never been observed in CTTSs. In fact, in a non-idelized case with $\beta << 1$, the single fibrils that compose the slab can be characterized by both a different mass densities and velocities. This would result in different periods and random phases of the oscillations. Orlando et al. (2010) proposed that an accretion stream composed of hundreds of independent fibrils would not produce any observable pulsed signal in the emission. Subsequent, further studies revealed that even small perturbations of the impact region, such as a clumpy density stream or a pressure fluctuation in the chromosphere, leads to strong consequences in the post-shock dynamics which determine the structure of the shock-heated plasma and heavily suppress QPOs (Matsakos et al. 2013).

To describe cases where the assumption $\beta << 1$ is no longer valid it is necessary to extend the model from 1 to 2 or 3 dimensions. In fact, in the case of $\beta \geqslant 1$, magnetic field lines can be dragged and distorted by the plasma motion, so that a multi-dimensional description is necessary.

Studies with 2D models were able to understand the role of magnetic field strength and topology in the dynamics of impact regions in CTTSs. Orlando et al. (2010) developed a 2D magnetohydrodynamic model describing an accretion column hitting the stellar chromosphere at different β parameters. Fig. 1.7 shows three different examples of impact regions that differ only in the magnetic field strength. For cases with $\beta >> 1$ the post-shock plasma is pushed laterally under the effects of the ram pressure of the downfalling plasma and generates hot outflows at the base of the slab. These outflows may perturb the surrounding stellar atmosphere in the form of MHD waves and plasma motion in the direction parallel to the stellar surface. The plasma ejected may also advect the magnetic field generating phenomena of magnetic reconnection that would result in a release of energy in the stellar atmosphere. This dynamic may link the stellar coronal activity to the accretion events.

Orlando et al. (2013) extended their previous study and focused their attention on the topology of the magnetic field and not only on the strength. In this case, they studied how different topologies of magnetic field can affect the dynamics of the post-shock region. They found that both intensity and configuration of magnetic field are extremely important to determine the geometry and structure of the post-shock plasma. In cases where $\beta \geqslant 1$, during the impact the hot plasma drags the magnetic field lines and generates a perpendicular component with respect to the accretion column downfalling direction. This component acts as a break, preventing the accretion column to sink deeply in chromosphere, and, also, affecting the dynamics of the post-shock plasma (see also Koldoba et al. 2008). Moreover, a dense and cold envelope is generated and surrounds the post-shock region. The topology of the magnetic field strongly perturbs the evolution of the impact regions, in fact different topologies generate post-shock regions with different shapes and locations.

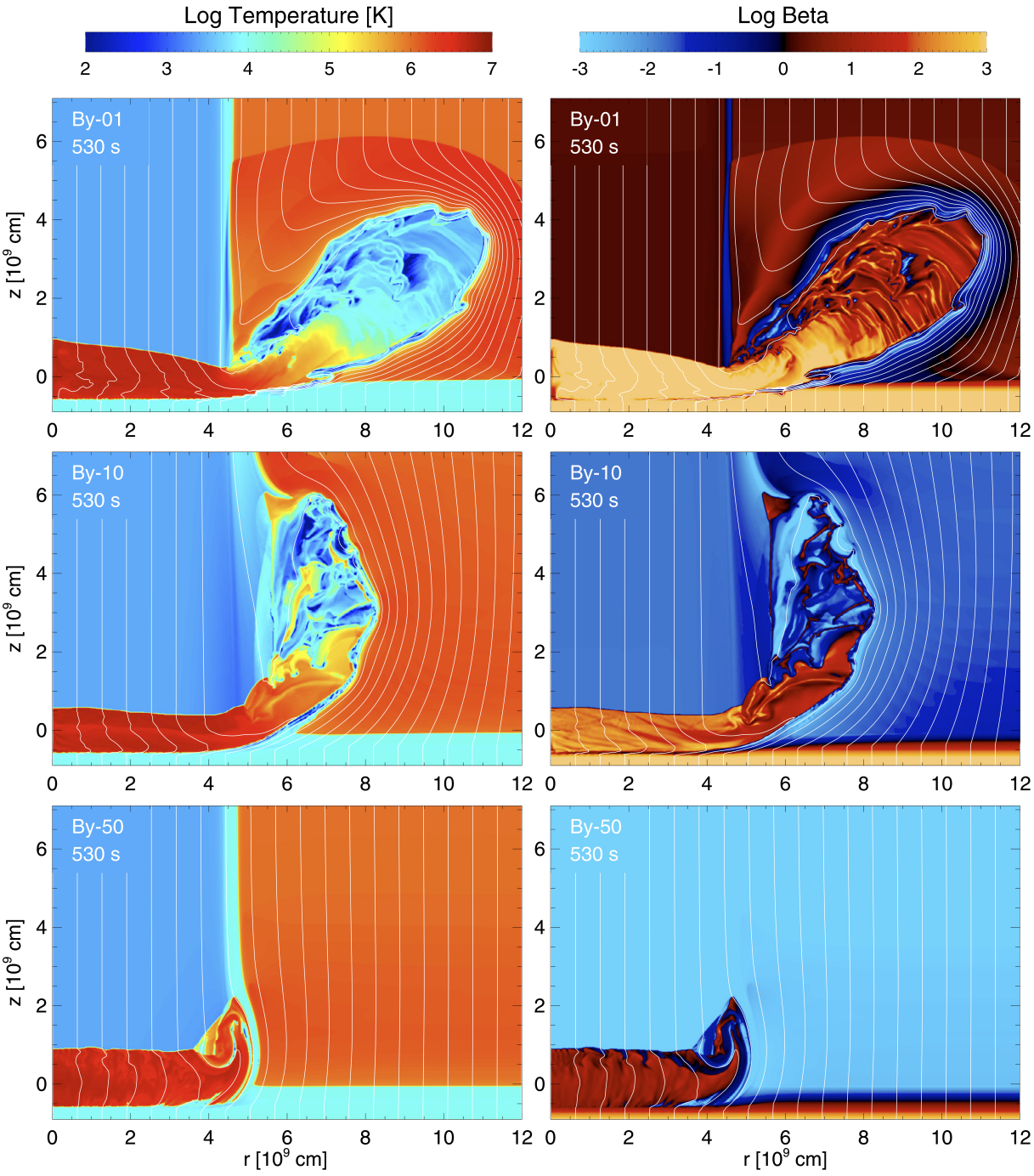

Figure 1.7 – Distribution of temperature (left panels) and plasma β (right panels) in the (r,z) plane in log scale. The magnetic field strength is 50 G (top panel), 10 G (mid panel) and 0.1 G (bottom panel). The white lines represent the magnetic field lines. Credit: Orlando et al. (2010)

Even though all these models provided a general view of the dynamics of impact regions, they have difficulties in explaining some features observed in different wavelength bands. For instance, UV observations of CTTSs show emission lines (e.g. C IV lines) characterized by complex and asymmetric profiles with the red wing much more extended than the blue one (Ardila et al. 2013). The line profiles can be described by two emission components: the first centered at velocities of the order of 100 km/s which is consistent with being emission arising from the post-shock plasma at the base of the accretion column; the second component centered at velocities of the order of 300 km/s and with the red wing extending up to velocities of the order of 500 km/s. The latter component cannot be explained as post-shock plasma at the base of the accretion column if the latter is uniform and continuous (as assumed, in general, by models of accretion impacts).

A possible hint to explain the profiles of UV lines observed in CTTSs came from the analysis of solar observations. On June 2011, a bright flare occurred on the Sun. The flare produced a large eruption of chromospheric material that, eventually, formed a coronal mass ejection. Part of the erupted material, however, felt back onto the Sun in the form of dense and cold blobs. Reale et al. (2013) studied the dynamics of the impact of the downfalling material by developing a 2D HD model describing the impacts of the downfalling blobs onto the solar surface and by comparing the model results with UV and X-ray observations. They found that the impacts produce UV lines with shifts comparable with those observed in some CTTSs. They suggested that a density structured accretion column may be the origin of the complex and asymmetric profiles of UV lines. Starting from this suggestion, Colombo et al. (2016) studied impacts of density structured accretion streams onto the surface of a CTTS. Using a 2D MHD model, they were able to explain the origin of strong Doppler shifts present in UV spectra observed in TW Hya.

Despite the numerous models developed in the last 20 years and the high level of physical insight of these models, none of them is able to synthesize UV and X-ray emission which are, at the same time, both consistent with observations (Curran et al. 2011; Costa et al. 2017). Several studies have shown that the X-ray emission arises from the shock-heated plasma (e.g. Argiroffi et al. 2007; Sacco et al. 2008, 2010). However, there is no certainty on where the UV emission comes from. The complexity of the impact regions requires a full physical description. In these regions, both optically thin and optically thick plasma components coexist, and the reprocessing of radiation is crucial. Models predict that the post-shock regions may be surrounded by cold material (Orlando et al. 2010, 2013; Bonito et al. 2014) that absorbs all, or part, of the radiation originating from the hot shocked plasma. This hypothesis was suggested by Reale et al. (2013) and then tested by Revet et al. (2017) that reproduced with a laboratory experiment impacts of accretion columns onto CTTSs. The conclusion was that significant absorption of X-ray emission is expected in impact regions.

Therefore, in order to have a better understanding of impact regions, it is necessary to include the effects of absorption of radiation by matter in the models. The first attempt was done by Costa et al. (2017). They developed a 1D model that includes the effects of absorption

of radiation by plasma. They used an iterative method: first, they solved the HD equations without including absorption effects; then, they derived the heating due to irradiation, and used it as an input for a new simulation of the accretion impact; finally they repeated the first two steps iteratively until the results converged. Their model suggests that part of the emission arising from the post-shock plasma is absorbed by the downfalling unshocked material. The irradiation heats the unshocked plasma up to temperatures of 10^6 K. Their work suggests the presence of a radiative precursor in the pre-shock accretion column, but underline the necessity of developing a self-consistent radiation hydrodynamic model of the impact region.

1.5 Open questions

Even though the accretion process is a very well studied phenomenon, both from an observational and a modeling point of view, there are still some issues not fully addressed.

As stated before (see Sect. 1.3.2), CTTSs are known to be strong X-ray emitters, characterized by a high level of coronal activity. One of the most debated issues in this field is the apparent correlation between coronal activity and accretion (Flaccomio et al. 2003; Preibisch et al. 2005). In fact, CTTSs which exhibit active accretion show an X-ray luminosity which is systematically lower than that observed in Weak line T Tauri stars (WTTSs), which do not exhibit accreting signatures (Neuhaeuser et al. 1995; Preibisch et al. 2005; Gregory et al. 2007; Drake et al. 2009). This evidence suggests that the coronal activity may be influenced by accretion or viceversa. Several scenarios were proposed in the last 15 years to explain if and how the coronal activity is linked to accretion. Some authors suggested that accretion modulates the X-ray emission through the suppression, disruption or absorption of the coronal magnetic activity (Flaccomio et al. 2003; Stassun et al. 2004; Preibisch et al. 2005; Jardine et al. 2006; Gregory et al. 2007). Other authors suggested that the coronal activity modulates the accretion flow driving the X-ray photoevaporation of the disk material (e.g. Drake et al. 2009).

Brickhouse et al. (2010) suggested that the accretion may even enhance the coronal activity around the region of impact of accretion streams. They proposed a scenario in which accretion produces hot plasma which populates the stellar corona, that, combined with different magnetic field configurations, can be constrained into loops or stellar winds. Orlando et al. (2011) proved that a high energetic flare occuring on the disk surface is able to perturb enough the disk stability and to trigger an accretion event. They explored the case of a very bight flare consistent with COUP observations and proved that an intense flare may perturb the disk stability and induce accretion of mass onto the star. Their work open a more general question: May a coronal activity, of the same type of those observed in CTTSs, perturb the disk stability and trigger accretion?

Once formed, the accretion columns impact onto the stellar surface at supersonic velocity. Models and analyses of observations at different wavelengths have proven that impact regions can present complex structures and dynamics. The accretion columns themselves can be structured in density (Orlando et al. 2011; Matsakos et al. 2013; Bonito et al. 2014; Colombo

et al. 2016, 2019c), so that post-shock regions may show a wide range of densities, temperatures, and velocities. As a result, different plasma components, both optically thin and optically thick, and emitting in different wavelength bands, co-exist. In this scenario, reprocessing of radiation, through absorption and re-emission, is expected (Calvet & Gullbring 1998; Lamzin 1998; Reale et al. 2013; Bonito et al. 2014; Revet et al. 2017) and may lead to complex profiles of emission lines. Even though it is probably an important ingredient, the role of absorption of radiation has been neglected in most models present in literature. The first work that includes such effects (done by Costa et al. 2017) suggests the presence of a radiative precursor. Since their approach is not fully self-consistent, these authors could not describe the structure of the precursor and derived a range of possible values of its temperature between $10^4 - 10^6$ K. More recently, de Sá et al. (2019) described accretion impacts in CTTSs with an "hybrid" model which makes a smooth transition between an LTE approach for the radiative transfer for the stellar chromosphere and a coronal model for the hot slab and found that non-LTE is required for a correct description of the phenomenon.

1.6 Purpose of this work

In this work, we investigate two aspects of the accretion process in CTTSs. We first explore the role of an intense flaring activity occurring in proximity of a disk surrounding a central protostar (Colombo et al. 2019c). The aim is to investigate if the common coronal activity of a young star made by several flares with small-to-medium intensity is able to perturb the disk and to trigger accretion as the single bright flare studied in Orlando et al. (2011). To this end, we adopt the 3D MHD model of the star-disk system presented in Orlando et al. (2011); the model includes the most important physical processes, namely the gravitational effects, the disk viscosity, the radiative losses from optically thin plasma, the magnetic field oriented thermal conduction, and the coronal heating (including heat pulses triggering the flares). We explore cases characterized by different densities of the disk or by different levels of coronal activity.

The second aspect of accretion that we investigate concerns the physical and radiative properties of impact regions. In particular, we investigate the effects of radiation on the structure of the accreting gas through a HD model of accretion impacts which includes self-consistently, for the first time, the effects of both radiative losses and absorption of radiation by matter in a non-LTE regime (Colombo et al. 2019b). In order to perform the calculation, we upgrade the LTE radiation-hydrodynamics module implemented in the PLUTO code, originally developed by Kolb et al. (2013), extending it to handle also a non-LTE regime (Colombo et al. 2019a). We validate our module through different test cases already discussed in literature. We, also, determine how shock structures and dynamics differ if they are described by performing the calculation in the LTE regime or, more in general, in the non-LTE regime. The new module allow us to investigate the role of absorption of radiation in the impact region of a CTTS. We describe the impact of an accretion column onto the stellar surface. We focus on a typi-

cal accretion column which produces detectable X-ray emission at its impact (Argiroffi et al. 2007; Sacco et al. 2010).

The manuscript is structured as follows: in Chapter 2 we present the results of the 3D MHD modeling of flaring activity in CTTSs; in Chapter 3 we present the radiative module implemented in PLUTO code; in Chapter 4 we show the results of the radiation HD simulations; finally in Chapter 5 we draw our conclusions.

CHAPTER 2

Effects of intense flaring activity in circumstellar disks

2.1 Introduction

In this chapter, we study if an intense flaring activity due to flares that occur close to the accretion disk may perturb the stability or even disrupt the inner part of the disk, and might, also, trigger accretion phenomena.

A first attempt to investigate the possible effects of a strong flare on the stability of a circumstellar disk around a CTTS was done by Orlando et al. (2011) (hereafter in the chapter Paper I). These authors developed a 3D magnetohydrodynamics (MHD) model describing the evolution of a flare occurring near the disk around a rotating magnetized star. They explored the case of a single bright flare with energy of the same order of magnitude (10^{36}erg) as those involved in the brightest X-ray flare observed in COUP (see Chapter 1 and Favata et al. 2005). They found that such energetic flare produces a hot magnetic loop which links the star to the disk. Moreover, the disk is strongly perturbed by the flare: a fraction of the disk material evaporates in proximity of the flaring loop and an overpressure wave, originating from the flare, propagates through the disk. When the overpressure wave reaches the opposite side of the disk, the material is pushed out and forms a dense ($n \geqslant 10^{10}\mathrm{cm}^{-3}$) funnel stream that is channeled by the magnetic field and accretes onto the central protostar.

Starting from the results of Paper I, here we study the effects of a storm of flares with small-to-medium intensity (compared to Paper I) occurring in proximity of a circumstellar disk. The aim is to investigate if the common coronal activity of a young star, made by several flares with small-to-medium intensity, is able to perturb the disk and to trigger accretion as the single bright flare studied in Paper I. To this end, we adopt the 3D MHD model of the star-disk system presented in Paper I. The model includes the gravitational effects, the disk viscosity, the radiative losses from optically thin plasma, the magnetic field oriented thermal conduction, and the coronal heating (including heat pulses triggering the flares). We explore cases characterized either by different densities of the disk or by different levels of coronal activity.

This chapter is structured as follow: in Sect. 2.2 we describe the physical model and the numerical setup; in Sect. 2.3 we present the results of modeling and the comparison with observations; in Sect. 2.4 we summarize the results and draw our conclusions.

This work has been published in Astronomy & Astrophysics (Colombo et al. 2019c).

2.2 MHD MODELING

We adopted the model presented in Paper I, which describes a rotating magnetized CTTS surrounded by a thick quasi-Keplerian disk (see Fig. 2.1), but modified to describe the effects of a storm of low to intermediate flares that occur close to the disk. The CTTS is assumed to have mass $M_\star = 0.8 M_\odot$ and radius $R_\star = 2 R_\odot$ (see Paper I)[1]. The flares occur in proximity of the inner portion of the disk. The magnetosphere is initially assumed to be force-free, with a topology given by a dipole and an octupole (Donati et al. 2007; Argiroffi et al. 2007), and both magnetic moments are aligned with the rotation axis of the star. In Paper I, we assumed the magnetic field to be aligned dipole-like. We assumed that the ratio of octupole-to-dipole strength is 4, as suggested for the CTTS TW Hya. This ratio can be different in different young accreting stars (e.g., Gregory & Donati 2011). The magnetic moments are chosen in order to have a magnetic field strength on the order of ≈ 3 kG at the surface of the star (Donati et al. 2007). The field ratio determines the topology of the magnetic field lines, and it is therefore expected to influence the dynamical evolution of the accretion streams. The dipole component has a magnetic field strength of about 700 G at the stellar surface and 27 G at the distance of 3 $R_\star$ (in proximity of the disk). At distances larger than $1.7 R_*$, the dipole component dominates and disrupts the inner portion of the disk at a distance of few stellar radii. Closer to the star (at distances smaller than $1.7 R_*$), the octupole component becomes dominant and the accreting plasma is expected to be guided by the magnetic field at higher latitudes than in the pure dipole case (e.g., Romanova et al. 2011a).

2.2.1 EQUATIONS

The system is described by solving the time dependent MHD equations in a 3D spherical coordinate system (R, θ, ϕ), including effects of gravitational force from the star, disk viscosity, thermal conduction that also includes the effects of heat flux saturation, coronal heating (using a phenomenological term composed of a steady-state component and a transient component; see Sect. 2.2.3), and the radiative losses from optically thin plasma. The time-dependent MHD equations are

[1] $M_\odot = 1.99 \times 10^{33}$ cm^{-3}; $R_\odot = 6.96 \times 10^{10}$cm

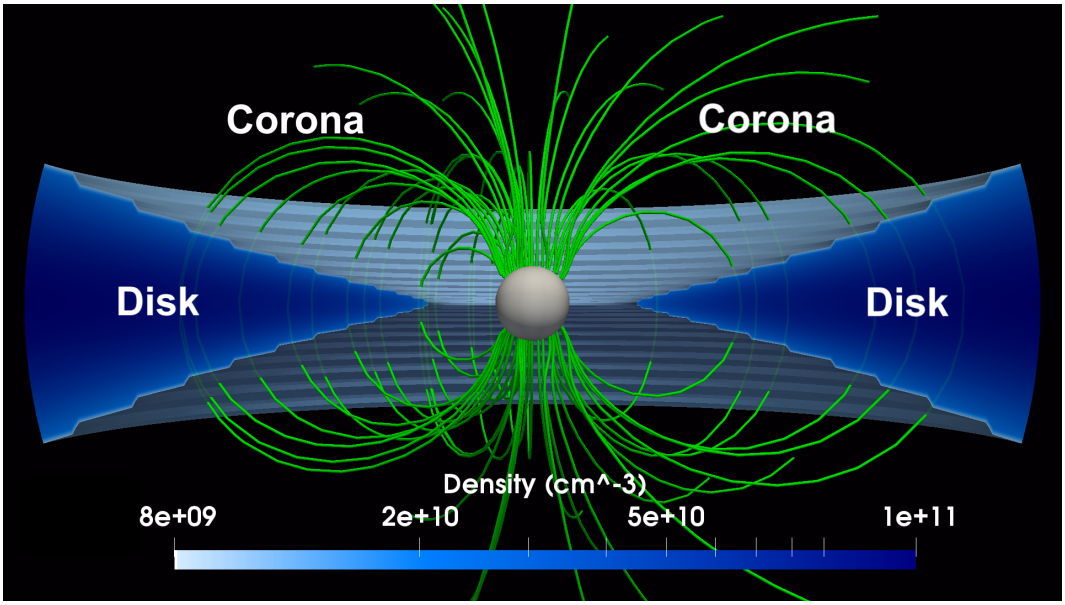

Figure 2.1 – Initial conditions for the reference case. In blue we present in logarithmic scale the density map of the disk, the green lines show the sampled magnetic field lines, and the white sphere represents the stellar surface that marks a boundary. (Colombo et al. 2019c).

$$\frac{\partial}{\partial t}\rho + \nabla \cdot \vec{m} = 0 \tag{2.1}$$

$$\frac{\partial}{\partial t}\vec{m} + \nabla \cdot (\vec{m}\vec{u} - \vec{B}\vec{B} + \vec{I}p_t - \vec{\tau}) = \rho\vec{g} \tag{2.2}$$

$$\frac{\partial}{\partial t}\rho E + \nabla \cdot [(\rho E + p_t)\vec{u} - \vec{B}(\vec{u}\cdot\vec{B}) - \vec{u}\cdot\vec{\tau}] = \vec{m}\cdot\vec{g} - \nabla\cdot F_c - n_e n_H \Lambda(T) + Q(R,\theta,\phi,t) \tag{2.3}$$

$$\frac{\partial}{\partial t}\vec{B} + \nabla \cdot (\vec{u}\vec{B} - \vec{B}\vec{u}) = 0, \tag{2.4}$$

where

$$p_t = P + \frac{\vec{B}\cdot\vec{B}}{2}, \qquad E = \epsilon + \frac{\vec{u}\cdot\vec{u}}{2} + \frac{\vec{B}\cdot\vec{B}}{2\rho} \tag{2.5}$$

are the total pressure (thermal and magnetic) and the total gas energy per unit mass (thermal, bulk kinetic, and magnetic), ρ is the density, $\vec{m} = \rho\vec{u}$ is the momentum density, $\vec{u}$ is the fluid bulk velocity, $\vec{B}$ is the magnetic field, $\vec{I}$ the identity matrix, $\vec{\tau}$ is the viscous stress tensor that we treat below in more detail, $\vec{g} = -\nabla\Phi_g$ is the gravity acceleration vector, $\Phi_g = -GM_\star/R$ is the gravitational potential of a central star of mass $M_\star$ at a distance R, G is the gravitational constant, F_c is the heat conductive flux, n_e and n_H are the electron and hydrogen number

density, $\Lambda(T)$ is the optically thin radiative losses per unit emission measure, T is the fluid temperature, and $Q(R, \theta, \phi, t)$ is a function of space and time describing the phenomenological heating rate (See Section 2.2.3). We used the ideal gas law $P = (\gamma - 1)\rho\epsilon$, where γ is the adiabatic index and ϵ is the thermal energy density. The radiative losses were defined for $T > 10^4$K and were derived with the PINTofALE (Kashyap & Drake 2000) spectral code and with the APED v1.3 atomic line database assuming metal abundances equal to 0.5 of the solar value (Anders & Grevesse 1989).

We assumed the viscosity to be effective only in the circumstellar disk and negligible in the extended stellar corona. The transition between corona and disk was outlined through a passive tracer ($C_{\mathtt{disk}}$) that is passively advected in the same manner as density (see Paper I for more details). The tracer was initialized with $C_{\mathtt{disk}} = 1$ in the disk region and $C_{\mathtt{disk}} = 0$ elsewhere. During the system evolution, the disk material and the corona mixed, leading to regions with $0 < C_{\mathtt{disk}} < 1$. The viscosity works only in regions with $C_{\mathtt{disk}} > 0.99$, that is, in zones consisting of more than 99% of disk material. The viscous tensor is defined as

$$\tau = \eta_\nu \left[(\nabla \vec{u}) + (\nabla \vec{u})^T - \frac{2}{3}(\nabla \cdot \vec{u})\vec{I} \right], \tag{2.6}$$

where $\eta_\nu = \nu_\nu \rho$ is the dynamic viscosity, and ν_ν is the kinematic viscosity. The accepted scenario considers the turbulence in the disk as the main responsible factor for the losses of angular momentum (Shakura & Sunyaev 1973), possibly triggered by MRI (Balbus & Hawley 1991, 1998). Because it is difficult to describe the phenomenon and we know little about its details, the efficiency of angular momentum transport within the disk is in general described through a phenomenological viscous term that is modulated through the Shakura–Sunyaev α-parameter (e.g., Romanova et al. 2002, Paper I). As in Paper I, the kinematic viscosity was expressed as $\nu_\nu = \alpha c_s^2/\Omega_K$, where c_s is the isothermal sound speed, Ω_K is the Keplerian angular velocity, and $\alpha < 1$ is a dimensionless parameter regulating the efficiency of angular momentum transport within the disk. Simulations of Keplerian disks indicate that the turbulence-enhanced stress tensor, which is responsible for the outward transport of energy and angular momentum, has a typical dimensionless value ranging between 10^{-3} and 0.6 (Balbus 2003). In our simulations, we assumed $\alpha = 0.02$ (according to Romanova et al. 2002).

The thermal conduction is anisotropic because of the stellar magnetic field, and it is highly reduced in the direction transverse to the magnetic field. We split the thermal conduction into two components, one along and the other across the magnetic field lines, $F_c = F_\parallel \mathbf{i} + F_\perp \mathbf{j}$. To allow for a smooth transition between the classical and saturated conduction regimes, we followed Dalton & Balbus (1993) and described the two components of thermal flux as (see also Orlando et al. 2008)

$$F_{\parallel} = \left(\frac{1}{[q_{spi}]_{\parallel}} + \frac{1}{[q_{sat}]_{\parallel}} \right)^{-1} \tag{2.7}$$

$$F_{\perp} = \left(\frac{1}{[q_{spi}]_{\perp}} + \frac{1}{[q_{sat}]_{\perp}} \right)^{-1,} \tag{2.8}$$

where $[q_{spi}]_{\parallel}$ and $[q_{spi}]_{\perp}$ are the classical conductive flux along and across the magnetic field lines, respectively, according to Spitzer (1962), that is,

$$[q_{spi}]_{\parallel} = -k_{\parallel} [\nabla T]_{\parallel} = -9.2 \cdot 10^{-7} T^{5/2} [\nabla T]_{\parallel} \tag{2.9}$$

$$[q_{spi}]_{\perp} = -k_{\perp} [\nabla T]_{\perp} = -3.3 \cdot 10^{-16} n_H^2 / (T^{1/2} B^2) [\nabla T]_{\perp,} \tag{2.10}$$

where $k_{\parallel}$ and $k_{\perp}$ are both in units of erg $K^{-1} s^{-1} cm^{-1}$ and $[\nabla T]_{\parallel}$ and $[\nabla T]_{\perp}$ are the thermal gradients along and across the magnetic field lines. If the spatial scale of the characteristic change in temperature becomes too short compared to the electron mean-free path, the heat flux saturates and the conductive flux along and across the magnetic field lines can be described as (Cowie & McKee 1977)

$$[q_{sat}]_{\parallel} = -\text{sign}([\nabla T]_{\parallel}) 5 \phi \rho c_s^3 \tag{2.11}$$

$$[q_{sat}]_{\perp} = -\text{sign}([\nabla T]_{\perp}) 5 \phi \rho c_s^3 \tag{2.12}$$

where c_s is the isothermal sound speed, and ϕ, called flux limit factor, is a free parameter between 0 and 1 (Giuliani 1984). For this work, $\phi = 1$ as suggested for stellar coronae (Borkowski et al. 1989; Fadeyev et al. 2002).

The calculations were performed using PLUTO, a modular Godunov-type code for astrophysical plasmas (Mignone et al. 2007). The code is designed to use parallel computers using Message Passage Interface (MPI) libraries. The MHD equations were solved using the MHD module available in PLUTO with the Harten-Lax-van Leer Riemann solver. We use a second order spatial reconstruction strategy. The time evolution was solved using a second-order Runge-Kutta method. The evolution of the magnetic field was calculated using the constrained transport method (Balsara & Spicer 1999), which maintains the solenoidal condition at machine accuracy. We adopted the "magnetic field-splitting" technique (Tanaka 1994; Powell et al. 1999; Zanni & Ferreira 2009) by splitting the total magnetic field into a contribution from the background stellar magnetic field and a deviation from this initial field; then, only the latter component was computed numerically. Radiative losses Λ were calculated at the temperature of interest using a lookup table and linear interpolation method. Thermal conduction was treated with a super-time-stepping technique, the superstep consists of a certain number of substeps that are properly chosen for optimization and stability, depending

on the diffusion coefficient, grid size, and free parameter $\nu < 1$ (Alexiades et al. 1996). The viscosity was solved with an explicit scheme, using a second-order finite difference approximation for the dissipative fluxes. We use the harmonic mean limiter of Van Leer.

2.2.2 Initial and boundary conditions

As in Paper I, we adopted the initial conditions introduced by Romanova et al. (2002), describing the star–disk system in quiescent configuration. In particular, the initial corona and disk were set in order to satisfy mechanical equilibrium among centrifugal, gravitational, and pressure gradient forces (see Paper I and Romanova et al. 2002 for more details); all the plasma is barotropic and the disk and the corona are both isothermal with temperatures T_d and T_c, respectively. The stellar rotation axis was set normal to the disk mid-plane, and the protostar was characterized by a rotational period of 9.2 d (see Paper I). The isothermal disk was at $T_d = 10^4$ K and dense (see Table 1); the disk rotated with Keplerian velocity about a rotational axis aligned with the magnetic dipole. In the initial condition the disk was truncated at the radius R_d, where the ram pressure of the disk plasma is equal to the magnetic pressure. In our setup the corotation radius (where the disk rotates with the same angular velocity of the protostar) was $R_{co} = 8.6R_\star$ (see Paper I). The corona was initially isothermal with temperature $T_c = 4$ MK (see Paper I).

We simulated one half of the whole spatial domain in spherical geometry. Thus, the computational domain extends between $R_{min} = R_\star$ and $R_{max} = 14R_\star$ in the radial coordinates, between $\theta_{min} = 5°$ and $\theta_{max} = 174°$ in the angular coordinate θ and between $\phi_{min} = 0$ and $\phi_{max} = 180°$ in the angular coordinate ϕ. The inner and outer θ boundaries do not correspond to the rotational axis to avoid very small $\delta\phi$ that increase the computational cost and add no significant insight (see Paper I for more details). The radial coordinate was discretized using a logarithmic grid with 128 points with the mesh size increasing with R, to achieve a high resolution close to the stellar surface $\Delta R_{min} \approx 3 \times 10^9$cm and a low resolution in the outer part $\Delta R_{max} \approx 4 \times 10^{10}$cm. The θ and ϕ coordinates grids were uniformly sampled and composed of 128 points each, corresponding to the resolution of $\Delta\theta \approx 1.3°$ and $\Delta\phi \approx 1.4°$, respectively

Our choice to consider only one half of the whole spatial domain was aimed at reducing the computational cost due to the complex dynamics of flares, which requires including radiative cooling and thermal conduction. The main consequence of this choice is that it introduces a long-wavelength cutoff on the perturbation spectrum of the disk. For instance, long-wavelength modes participating in the development of instability at the disk truncation radius are not represented in our model. Nevertheless, we expect that these particular perturbations are not likely to dominate the system evolution; morerover, the study of these perturbations is beyond the scope of this study.

The radial internal boundary condition was defined assuming that the infalling material passes through the surface of the star as in Romanova et al. (2002), thus ignoring the dynamic of the plasma after it impacts onto the stellar surface. A zero-gradient boundary condition was

set at R_{max} and at the boundaries of θ_{min} and θ_{max}. Periodic boundary conditions were set at ϕ_{min} and ϕ_{max}.

2.2.3 Coronal heating and flaring activity

The term $Q(R, \theta, \phi, t)$ in Eq. 3 is a phenomenological heating function. It is prescribed as a stationary component, plus a transient component in analogy with the function proposed by Barbera et al. (2017). The former was chosen to exactly balance the radiative losses below 1 MK in the corona,and maintained an initial quasi-stationary extended tenuous corona.

The transient component describes a storm of low to intermediate flares that occur in proximity of the disk. This component is expected to mimic the flaring activity that may be driven by a stressed field configuration resulting from the twisting of magnetic field lines induced by the differential rotation of the inner rim of the disk and the stellar photosphere (Shu et al. 1997).

Each flare was triggered by injecting a localized release of energy that produces a heat pulse. All the pulses had a 3D Gaussian spatial distribution with a width of $\sigma = 2 \times 10^{10}$cm. The pulses were randomly distributed in space close to the disk surface at radial distances between the truncation radius and the corotation radius. The flares had a randomly generated timing in order to achieve an average frequency of flare per hour of either one or four flares. The total energy released in a single pulse was also randomized, and it ranged in particular between 10^{32} and 10^{34} erg. The total time duration of each pulse was 300 s, then the pulse was switched off. The short duration of the pulses was chosen to describe an impulsive release of energy. Tests performed in Paper I proved that a duration of 300 s represents the minimum pulse duration that can be managed by the code. The time evolution of pulse intensity consists of three equally spaced phases of 100 s each: a linearly increasing ramp, a steady part, and a linearly decreasing ramp.

2.3 Results

Our model solutions depend on a number of physical parameters, among which the most notable are the density of the disk and the frequency of flares. In the light of this, we considered as a reference case (run FL-REF in Table 1) the disk configuration investigated in Paper I, which is characterized by a maximum density in the equatorial plane of 2.34×10^{10} cm^{-3} and a frequency of flares of four per hour. Then we explored the case of a disk that was five times denser than in the reference case (run FL-HD), and the case of a frequency of flares four times lower than in the reference case (run FL-LF). We also considered an additional simulation identical to the run FL-HD, but without flares (run NF), to highlight the role played by the flares in the formation of accretion columns in the timescales we covered. We considered the case with the densest disk because we expect a more efficient interaction between disk and stellar magnetosphere, which helps the formation of accretion columns. The simulation

Table 2.1 – Model parameters defining the initial conditions of the 3D simulations.

Run	ρ_d [cm^{-3}]	ρ_c [cm^{-3}]	F_{fl} [flares/hour]
FL-REF	2.34×10^{10}	9.37×10^{7}	4
FL-HD	9.37×10^{10}	9.37×10^{7}	4
FL-LF	2.34×10^{10}	9.37×10^{7}	1
NF	9.37×10^{10}	9.37×10^{7}	0

FL-HD generates the highest accretion rates ($\approx 10^{-9}\,M_\odot$ year^{-1}; see Fig. 8). Table 2.1 summarizes the various simulations and the main parameters that are characteristic of each run: ρ_d is the maximum density of the disk in the equatorial plane, ρ_c is the density of the corona close to the disk, and F_{fl} is the flare frequency.

Our main focus here is on exploring the role played by the flares in perturbing the accretion disk and possibly in triggering accretion on timescales shorter than those if flares were not present. For this reason, we stopped the simulations when the accretion rates reached a quasi-stationary regime after the initial sudden and steep rise (see Sect. 3.3); our simulations cover about three days of evolution ($\approx 1/3$ of the rotational period of the inner disk).

We followed the evolution of the system without flares (i.e., run NF) for about four days (i.e., on a timescale larger than that covered by the other simulations). We note that the initial conditions adopted provide quasi-equilibrium. The disk was initially truncated at $2.86R_\star$. When the simulation started, the magnetic field lines of the slowly rotating magnetosphere threading the disk exerted a torque on the faster-rotating disk. As a result, the inner part of the disk moved inward on a timescale that was shorter than the viscous timescale, and matter gradually accumulated in proximity of the truncation radius located at $R_d \approx 2.1R_\star$ at the end of the simulation. As shown by long-term 3D simulations (e.g., Romanova et al. 2002, 2011b; Kulkarni & Romanova 2008), this process of inward motion of matter at some point leads to accretion onto the star without any need of flares. However, run NF shows that this initial torque helps to bring matter toward the magnetosphere of the star, but no accretion stream develops in the timescale we considered. By the end of the simulation, there is a hint of mass accretion that leads to rates on the order of $10^{-10}\,M_\odot$ year^{-1} (about an order of magnitude lower than in the corresponding simulation with flares; see Fig. 8). We conclude that higher levels of accretion driven by the magnetic torque in our star-disk system start on timescales longer than about four days. In the following, we discuss in detail the simulations, including the effect of flares. In the light of the results of run NF, we are confident that disk perturbations and the accretion rates found in the timescale we considered are entirely due to the flaring activity.

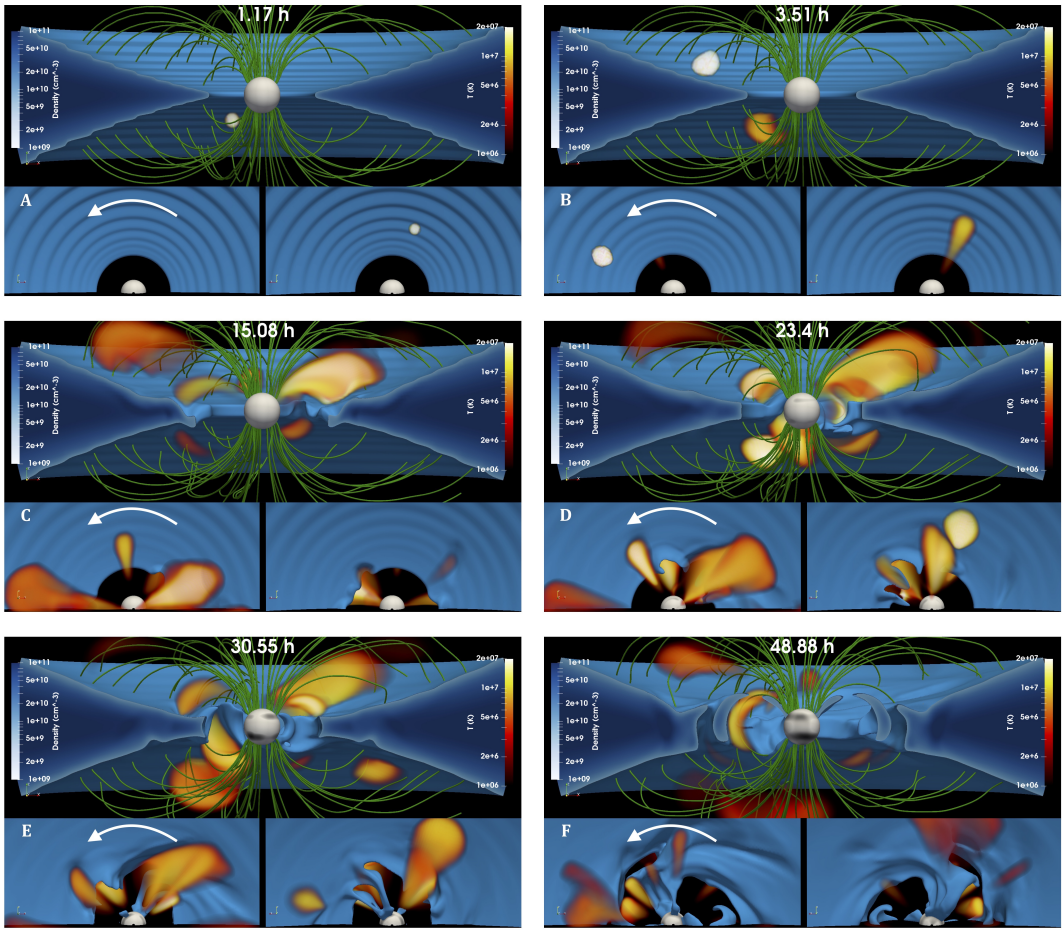

Figure 2.2 – Evolution of the reference case FL-REF. Each of the six panels shows a snapshot at a given time after the initial condition (defined in Sect. 2.2 in Fig. 2.1) at 1.17 h (A), 3.51 h (B), 15.08 h (C), 23.4 h (D), 30.55 h (E), and 48.88 h (F). Each panel is composed of three images: at the top, an edge-on view of the 3D system, at bottom left and right, the two pole on views. The cutaway views of the star-disk system show the mass density (blue) and sampled magnetic field lines (green) at different times. A 3D volume rendering of the plasma temperature is overplotted in log scale on each image and shows the flaring loops (red-yellow) that link the inner part of the disk with the central protostar. The color-coded density logarithmic scale is shown on the left of each panel, and the analogously coded temperature scale is on the right. The white arrows indicate the rotational direction of the system. The physical time since the start of the evolution is shown at the top center of each panel. (Colombo et al. 2019c).

2.3.1 REFERENCE CASE

For the reference case FL-REF, we followed the evolution of the flaring activity on the star-disk system for approximately three days (i.e., when a stationary regime was reached). Fig. 2.2 shows representative frames to describe this evolution. The figure shows the evolution of FL-REF. Each frame is composed of three panels: at the top, an edge-on view of the system, at the bottom left and right, the two pole-on views. The figure shows the mass density (blue) and sampled magnetic field lines (green). A 3D volume rendering of the plasma temperature is overplotted in log scale and shows the flaring loops (red-yellow).

As discussed in Sect. 2.2.3, the heat pulses triggering the flares are injected into the system at randomly chosen locations above and below the disk through the phenomenological term $Q(R, \theta, \phi, t)$ in Eq.(3). We found that the evolution of each flare is analogous to the evolution of the single bright flare analyzed in Paper I. For example, this is evident for the first flare in run FL-REF, which occurs after about one hour since the initial condition (see the lower right panel in Fig.2.2 A-B) and is not perturbed by other flares during its entire lifetime.

The initial heat pulse determines a local increase in plasma pressure and temperature close to the disk surface. As a result, the disk material is heated up and rapidly expands through the overlying hot and tenuous corona, resulting in a strong evaporation front. The disk evaporation is sustained by thermal conduction from the outer layers of hot plasma even after the heat pulse ends. The fraction of this hot expanding material closer to the protostar is confined by the magnetic field due to $\beta < 1$ and forms a hot (temperature of about $10^7 - 10^9$ K) magnetic loop with a length on the order of 10^{11} cm that links the disk to the stellar surface. The magnetic-field-oriented thermal conduction furthers the development of this hot loop through the formation of a fast thermal front propagating from the disk along the magnetic field lines toward the star. The remaining part of the evaporating plasma that is not channeled in the loop is poorly confined by the magnetic field (due to $\beta > 1$). Thus it moves away from the system toward regions with higher β, carrying away mass and angular momentum from the system (see below). In any case, the plasma (either magnetically confined or non-confined) starts to cool down as soon as the heat deposition ends because of the combined action of radiative losses, thermal conduction, and plasma expansion. After about 10 hours, the hot loop disappears.

Fig. 2.3 shows the evolution of the maximum temperature and emission measure (EM(T) = $\int_V n^2 dV$ it gives informations about the components of plasma emitting at a given temperature) of the second flaring loop (see Fig. 2.2 B). This evolution can be considered to be representative of all the flares simulated here and is analogous to that observed on Sun and stars. We distinguished two different phases in the evolution: a heating and a cooling phase. The first starts with the injection of the heat pulse and lasts for a few hundred seconds. During this phase the temperature increases very rapidly and reaches maximum at $\approx 10^9$K. The disk material evaporates under the effect of the thermal conduction and the heated plasma expands, filling a magnetic flux tube that links the disk with the star. As a result, the EM rapidly increases and peaks at later times, about 6 minutes after the maximum temperature.

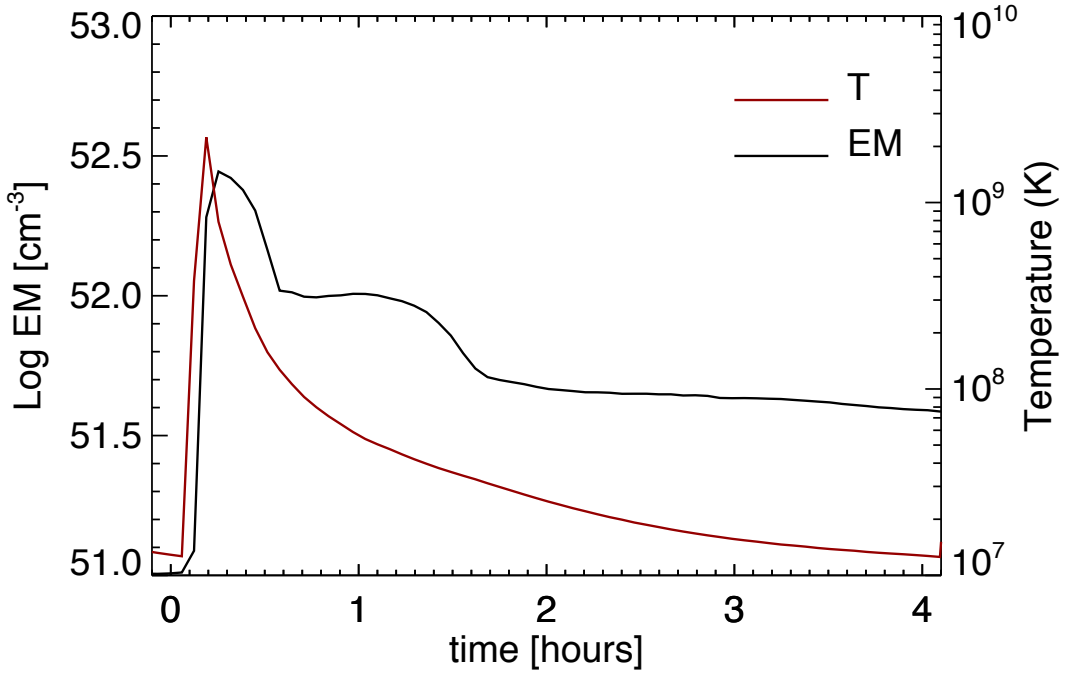

Figure 2.3 – Evolution of the maximum temperature (red line) and integrated EM (black line) of the plasma with $\log(T) > 6.3$ for the second flare in run FL-REF. The initial time is at the release of the corresponding heat pulse. (Colombo et al. 2019c).

At later times, the radiative losses and the thermal conduction very efficiently cool the plasma down and the cooling phase starts. Both the temperature and the EM decrease slowly. After about four hours since the heating, the temperature of the flaring plasma is still on the order of 10^7 K. The EM develops a plateau about one hour after the peak, which is at odds with the expected evolution on the base of 1D models of flares (e.g., Reale et al. 1988). As discussed in Paper I, each flare of our simulations is only partially confined by the magnetic field at the loop footpoint anchored at the disk surface, which is at variance with 1D models where the flares are assumed to be fully confined by the magnetic field. The plateau of EM in Fig. 2.3 originates from the fast expansion of the non-confined hot plasma in the surrounding environment. From this point of view, our simulated flares can be considered to be intermediate between those of models of fully confined flares (e.g., Reale et al. 1988) and those of models of non-confined flares (e.g., Reale et al. 2002). We also note that the magnetic field in the domain is idealized. In a more realistic case the evolved magnetic field may have a more complex configuration, and may be more intense than in the case studied because of magnetic field twisting. For this reason we expect to observe a greater confinement in a real case than in the simulations.

In addition to the formation of the hot loop, the initial heat pulse produces an overpressure wave at the loop footpoint that is anchored to the disk, which propagates through the

disk. In the case of the energetic flare investigated in Paper I, when the overpressure reaches the opposite side of the disk, it pushes the material out of the equilibrium position and drives it into a funnel flow (see Paper I for more details). Then the gravitational force accelerates the plasma toward the central star where the accretion stream impacts. In run FL-REF, however, the flares are less energetic than the flare in Paper I. The overpressure wave generated by the first flare is not strong enough to significantly perturb the disk and to eventually trigger an accretion event.

After the first flare, other flares occur close to the disk surface. Each of them produces a significant amount of hot plasma (with temperatures up to $\approx 10^9$ K) that is thrown out in the magnetosphere (Fig. 2.2 C-F). As for the first flare, part of this hot material is channeled by the magnetic field in flux tubes that form hot magnetic loops that link the disk to the central protostar. Nevertheless, most of the evaporated disk material is poorly confined by the magnetic field (especially in flares that occur at larger distances from the star) and it escapes from the system, contributing to the plasma outflow from the star with a mass loss rate $M_{loss} \approx 10^{-10}\, M_\odot\ yr^{-1}$ and angular momentum loss rate $L_{loss} \approx 10^6 - 10^7\ g\ cm^2\ yr^{-1}$. As a result, the magnetic field lines are gradually distorted by the escaping plasma. All this hot plasma, either confined to loops or escaping from the star, forms an extended hot corona that once formed, persists until the end of the simulation.

Fig. 2.4 shows the evolution of the integrated EM of the whole system. After the first heat pulse, the emission measure increases rapidly. In this transient phase, the extended corona is not developed yet and the effect of each heat pulse is clearly visible in the curve with the sudden increase and slower decay of EM. After the first flares, the amount of plasma at temperatures greater than 2 MK continues to increase, reaching a quasi-stationary regime after ≈ 10 hours. At this time the hot extended corona is well developed. The resulting values of EM for plasma above 2 MK indicate that the flaring activity is expected to produce a significant X-ray emission. During this phase, the pronounced peaks of EM are produced by the most energetic flares.

We synthesized the X-ray luminosity (L_X) in the band [1,10] keV from the reference case. We applied a procedure analogous to the one described in Paper I (see also Barbera et al. 2017). We found that during the stationary phase, $L_X \approx 10^{30}$erg/s. This value is in the range of luminosities typically inferred from observations (Preibisch et al. 2005). A detailed study of the evolution and origin of the X-ray emission will be the subject of a future work (see Sect. 5.2).

As for the first flare, each subsequent abrupt release of energy produced a local increase in plasma pressure in regions of the disk that correspond to the loop footpoints. These local increases in pressure produce overpressure waves that propagate through the disk. In general, given the low energy of most of the flares, the single overpressure wave is not sufficient to significantly perturb the disk and trigger an accretion column. However, the combination of a series of these overpressures can strongly perturb and distort the disk, especially in proximity of the truncation radius (see Fig. 2.2 F). Eventually, the overpressures can produce mass accre-

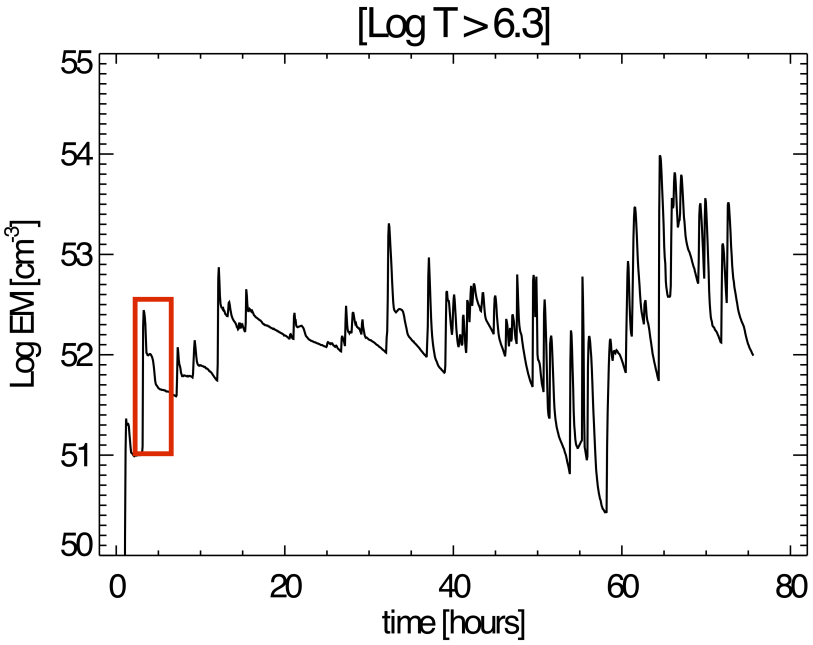

Figure 2.4 – Evolution of the integrated EM for plasma with $\log(T) > 6.3$ for the run FL-REF. The red square is zoomed-in in Fig.2.3. (Colombo et al. 2019c).

tion episodes. After $\approx$ 15 hours, several accretion columns start to develop (Fig. 2.2 C). The first column impacts onto the stellar surface after $\approx$ 23 hours (Fig. 2.2 D). Then, the accretion process continues until the end of the simulation.

The dynamics of the accretion columns is complex, as expected because the corotation radius of our system ($R_{co} = 8.6R_*$) is much larger than the magnetospheric radius ($\approx 2-3R_*$). In these conditions, the material accretes in a strongly unstable regime (Blinova et al. 2016), where one or two unstable filaments ("tongues") form and rotate approximately with the angular velocity of the inner disk. In our simulation, the system evolution is analogous and accretion columns develop from the disk surface in regions close to the truncation radius. There, the disk material is channelled by the magnetic field in accretion streams that accelerate toward the central star under the effect of gravity. Then the accretion streams impact onto the stellar surface at high latitudes ($> 40°$; see Sect. 2.3.4). The accretion pattern suggests accretion driven by Rayleigh-Taylor (RT) instability (e.g., Blinova et al. 2016). As expected for RT unstable accretion, the formation of small-scale filaments along the edge of the disk and the formation of several funnels is indeed visible. Their occurrence and shape are typical of unstable tongues: they form frequently and disappear rapidly, and they are initially tall and narrow (e.g., Kulkarni & Romanova 2008, 2009; Romanova et al. 2008; Blinova et al. 2016). In 3D simulations of accretion onto stars with a tilted dipole, the instability is triggered and supported by the non-axisymmetry introduced by the dipole and by the pressure gradient force that develops close to the truncation radius through accumulation of matter by

disk viscosity (Romanova et al. 2012). In our case of a non-tilted dipole-octupole simulated on short timescales, the X-ray flares provide the necessary amount of non-axisymmetry and determines the pressure gradient force to start and support accretion through instability. In the simulation without flares (run NF), no sign of instability is present in the timescale covered (about four days). Therefore, even if matter were to accrete onto the protostar through MHD processes of the disk-magnetosphere interaction, this phenomenon would occur on timescales longer than those covered here in our simulations. The flares therefore provide the conditions to speed up the process on timescales significantly shorter (only a few hours) than those present in the case without flares.

The streams can be heavily perturbed during their lifetime by the flaring activity and by other streams. For instance, a flare occurring on the opposite side of the disk may trigger an overpressure wave that may enhance the accretion rate of the stream. A flare occurring close to the accretion column may inject more mass into the stream increasing its lifetime (see Fig. 2.5) or it may produce a perturbation that is strong enough to disrupt the base of the stream and, as a consequence, the whole accretion column. The streams may interact with each other, merging into larger streams. As a result of this complex dynamic, the streams are highly unstable and time variable, and the accretion columns are highly inhomogeneous, structured in density, and clumped (e.g., Matsakos et al. 2013; Colombo et al. 2016). This may support the idea that the persistent low-level hour-timescale variability observed in CTTSs may reflect the internal clumpiness of the streams (Gullbring et al. 1996; Safier 1998; Bouvier et al. 2007; Giardino et al. 2007; Cranmer 2009).

2.3.2 Comparison with other models

We explored the effects of either the disk density or the flare frequency on the dynamics of the star-disk system. To this end, we considered the case of a disk that was five times denser than in the reference case (run FL-HD in Table 2.1) and had the same sequence of flares. We found that the evolution in run FL-HD is analogous to that of the reference case. In particular, the random heat pulses produce hot plasma in proximity of the disk surface; then part of this plasma is channeled in hot loops, and the other part escapes from the system. All this hot material forms an extended and structured hot corona. As for the reference case, the heat pulses also generate overpressure waves that propagate through the disk, eventually pushing the disk material out of equilibrium to form accretion columns. In the case of a denser disk, however, the effects of these waves moving through the disk are mild in comparison with run FL-REF. The perturbation of the disk is limited to the surface of the disk and the latter is less distorted than in FL-REF (see Figs. 2.6-2.7). Nevertheless, the disk material channeled in accretion streams is on average denser than in FL-REF so that the accretion columns are in general denser than in the reference case (see Fig. 2.6).

For the dependence of the system evolution on the flare frequency, we found that the dynamics can be significantly different if the flare frequency is four times lower than in FL-REF. In this case, the system needs more time for a significant perturbation of the disk that

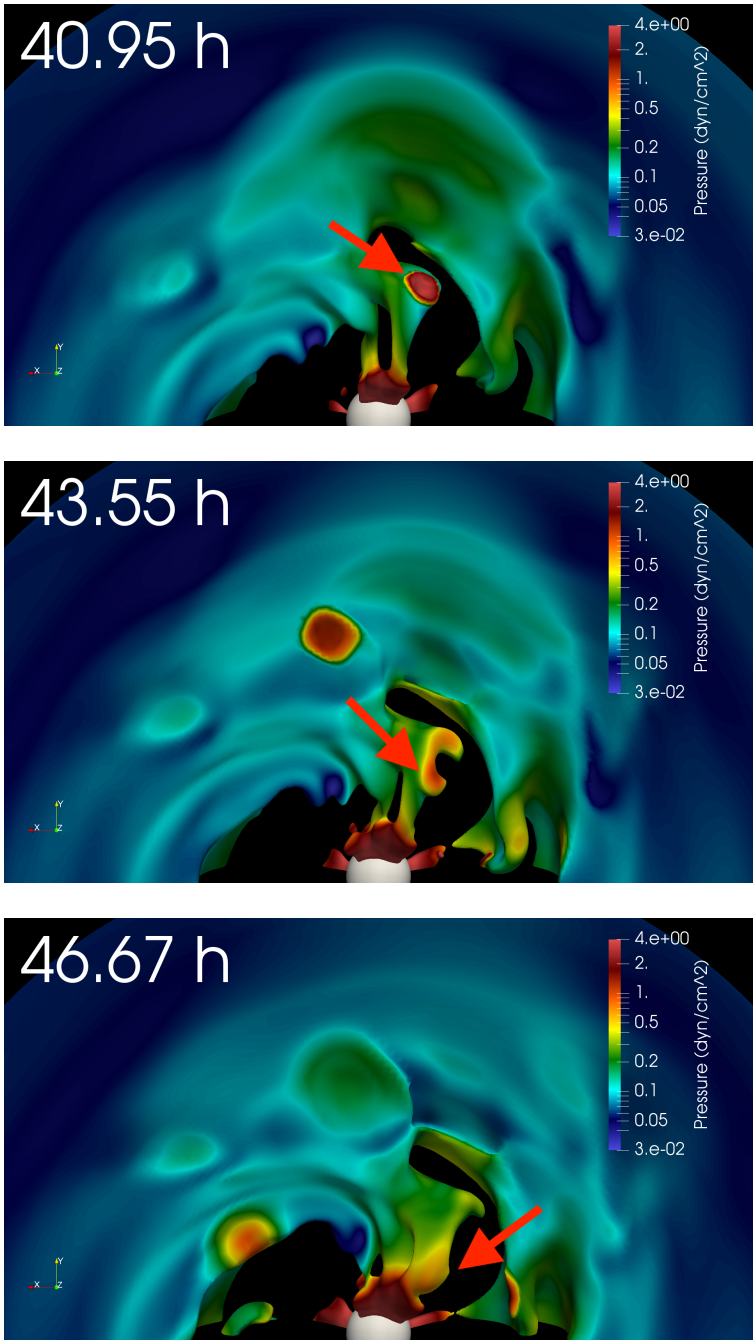

Figure 2.5 – Example of the perturbation of an accretion column by nearby flaring activity. The figure shows snapshots displaying isosurfaces where the particle number density equals 5×10^9 cm^{-3} in run FL-REF. We show the southern pole-on view of the star. The isosurfaces, which coincide with the cold and dense disk material, are shown at the labeled times (upper left corner of each panel). The colors give the pressure (in units of dyn cm^{-2}) on the isosurface, and the color-coding is defined on the right of each panel. Upper panel: Red arrow points at flare that perturbs the accretion column (see high-pressure region in the disk). Middle and lower panel: Red arrow points at the portion of the disk material that perturbs the accretion column. (Colombo et al. 2019c).

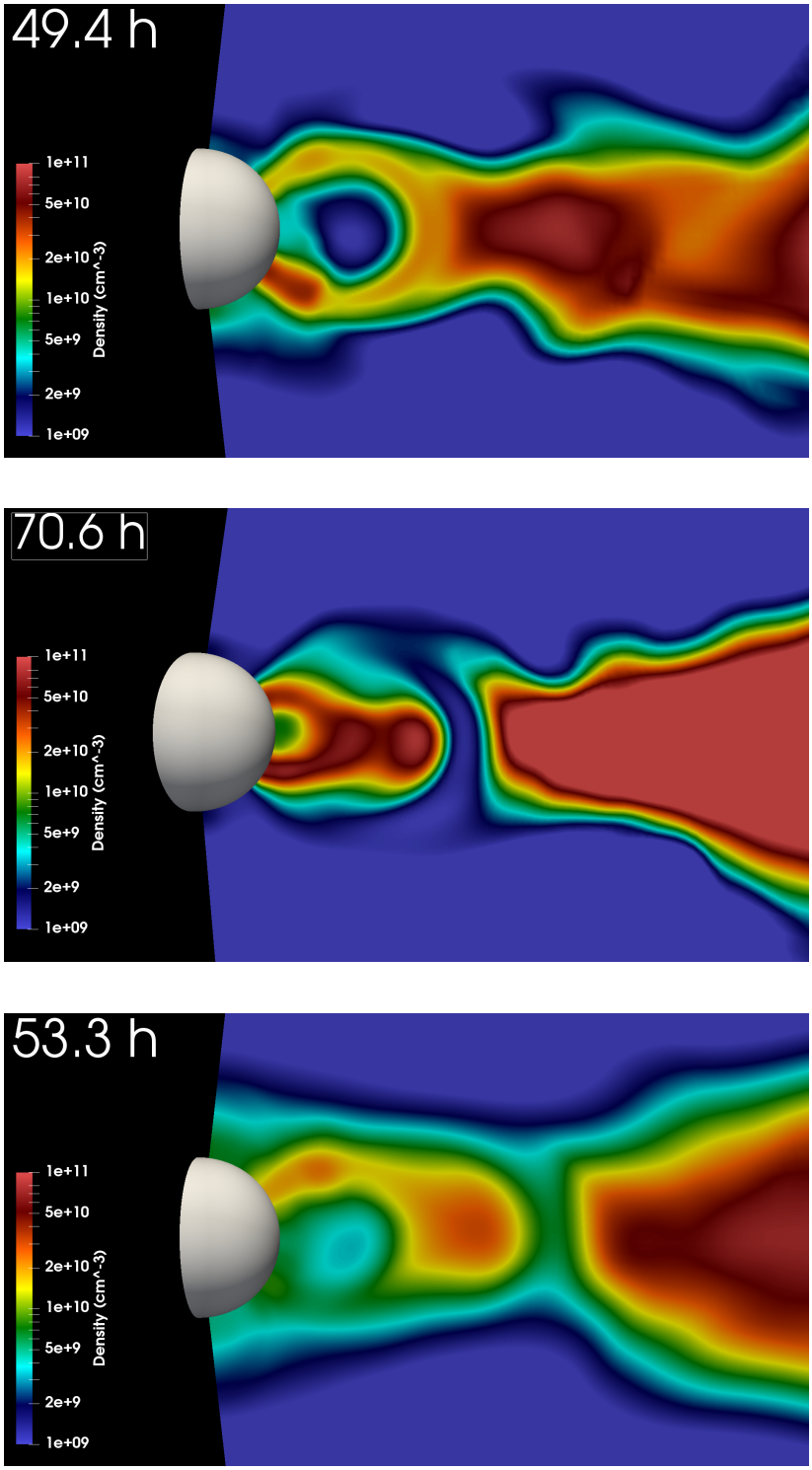

Figure 2.6 – Close-up view of the structure of the accretion columns for runs FL-REF (top panel), FL-HD (middle panel), and FL-LF (bottom panel). Each panel shows a slice in the (R, z) plane passing through the middle of one of the streams. The white hemisphere represents the stellar surface. (Colombo et al. 2019c).

is able to produce mass accretion onto the central protostar. The dynamics of the accretion columns, once formed, is similar to that in runs FL-REF and FL-HD. The main difference is the number of streams, which is lower in run FL-LF than in the other two cases. This is a direct consequence of the lower number of flares in run FL-LF, which can contribute to the disk perturbation with their overpressure waves. After about 60 hours, only one prominent accretion column is present, whereas in runs FL-REF and FL-HD, two or more accretion columns are clearly visible (see Fig. 2.7). Nevertheless, a significant mass accretion is present in the system at the end of the simulation, even though the flare frequency is lower than in FL-REF.

2.3.3 Accretion rates

From the modeling results, we derived the mass accretion rates due to the various streams triggered by the flares. We considered as accreting material the amount of mass that crosses the internal boundary representing the stellar surface, namely the material that falls onto the central star. Fig. 2.8 shows the evolution of the accretion rates for the four simulations in Table 2.1. The three cases with flares show qualitatively the same trend. After the first stream hits the stellar surface (during the first 20 hours of evolution; in run FL-LF this occurs after about 50 hours), the accretion rate rapidly increases due to the rapid development of new accretion columns. This phase is transient and lasts for about10 hours (see Fig. 2.2 D). After this, the accretion rate increases more slowly and enters a phase in which the number of active accretion columns is roughly constant.

After the transient phase, the three cases show accretion rates ranging between $\approx 10^{-10}$ $M_\odot$ yr^{-1} and $\approx 10^{-9}$ $M_\odot$ yr^{-1}, with the highest values shown by run FL-HD because the streams are denser than in the other two cases, and FL-LF and FL-REF show the lowest values because the disk is less dense (see Sect. 2.3.2). After about 70 hours of evolution, run FL-LF shows accretion rates that are comparable to those of run FL-REF. These two cases differ only for the frequency of flares, and they consider the same density structure of the disk; thus run FL-LF needs more time to reach the accretion rate values shown in run FL-REF. We conclude that the accretion rates depend more strongly on the disk density than on the flare frequency.

The simulation without flares (run NF) does not show accretion during the first approximately 65 hours of evolution. In this time the magnetic torque brings matter toward the magnetosphere of the star, and after about 65 hours leads to inflow of matter that generates a sudden increase in the accretion rate up to $\approx 10^{-10}$ $M_\odot$ yr^{-1}. The rate then slowly increases until the end of the simulation, when it reaches values that do not exceed $\approx 3 \times 10^{-10}$ $M_\odot$ yr^{-1}. In the corresponding simulation with flares (run FL-HD), the accretion starts much earlier, about 20 hours after the start of the simulation, with rates more than an order of magnitude higher than in run NF on the timescale we covered. The disk perturbation and the mass accretion we observed in simulations with flares are therefore due to the flaring activity in proximity of the disk.

We compared the accretion rates derived from our 3D simulations with those available in

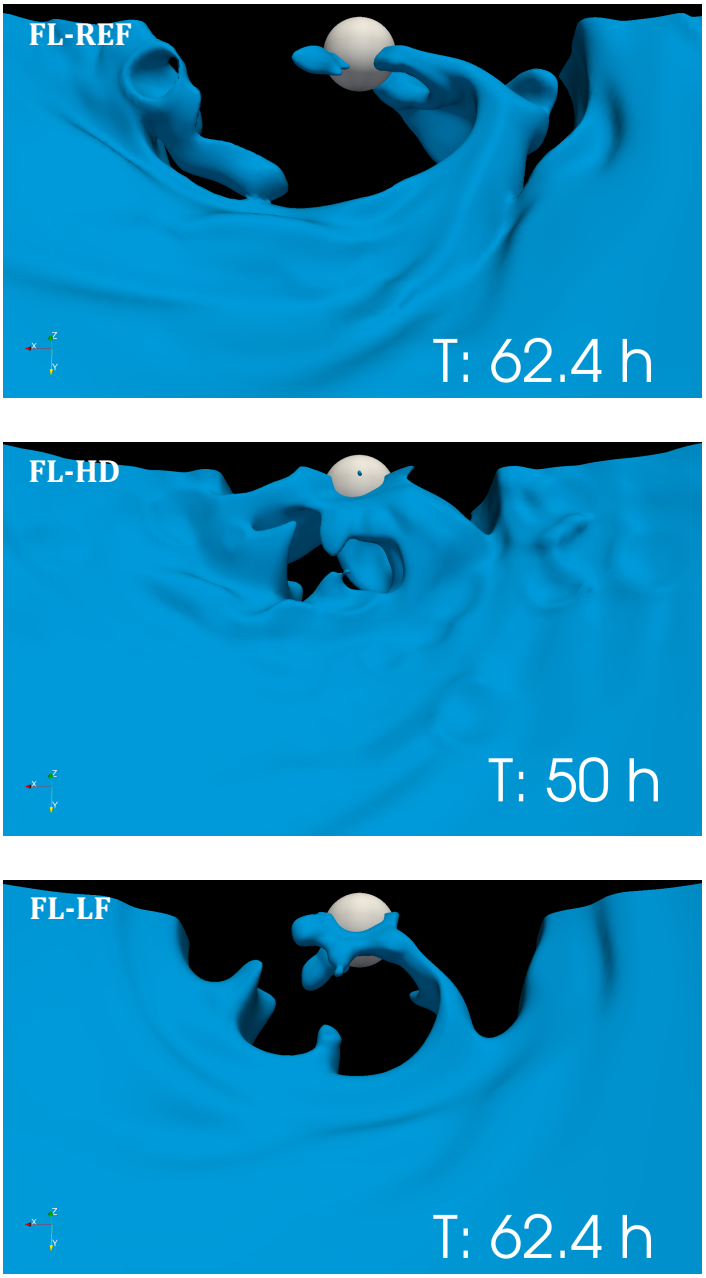

Figure 2.7 – Representative close up views of the inner region of the star-disk system for runs FL-REF (top panel), FL-HD (middle panel), and FL-LF (bottom panel). In blue we show the isosurfaces where the disk material has a particle number density $n = 10^{10}\mathrm{cm}^{-3}$. The white sphere in each panel represents the stellar surface. (Colombo et al. 2019c).

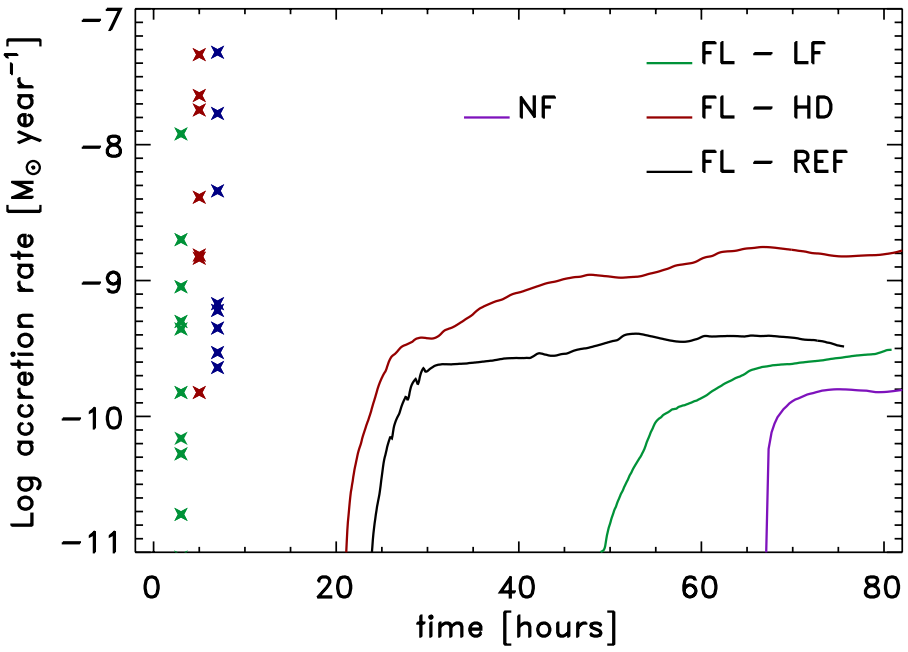

Figure 2.8 – Evolution of accretion rates synthesized from runs FL-RF (black line), FL-HD (red line), FL-LF (green line), and NF (purple line). The crosses represent the values of mass accretion rates inferred from optical-near UV observations for a sample of low-mass stars and brown dwarfs (green, Herczeg & Hillenbrand 2008), for a sample of solar-mass young accretors (red, Herczeg & Hillenbrand 2008), and for an X-ray-selected sample of CTTSs (blue, Curran et al. 2011); their position on the time axis is chosen to facilitate comparison with the model results. (Colombo et al. 2019c).

the literature derived from optical–UV observations. In particular, we considered two samples of low-mass young accreting stars analyzed by Herczeg & Hillenbrand (2008) that were observed with the Low Resolution Imaging Spectrometer (LRIS) on Keck I and with the Space Telescope Imaging Spectrograph (STIS) on board the Hubble Space Telescope, and an X-ray selected sample of CTTSs analyzed by Curran et al. (2011) that was observed with various optical telescopes. We found that the three simulations reproduce most of the accretion rates measured in low-mass stars quite well and are lower than those of fast-accreting objects such as BP Tau, RU Lup, or T Tau. On the other hand, it is worth noting that the timescale we explored here is rather short (about 80 hours) so that the disk viscosity, for instance, has a negligible effect on the dynamics.

2.3.4 Hotspots

The disk material flowing through the accretion columns is expected to impact onto the stellar surface and to produce shock-heated spots. We do not have enough spatial resolution in our simulations to model these impacts (see, e.g., Orlando et al. 2011, 2013). The model does not include a description of the chromosphere of the CTTS either, which would be necessary to produce shocks at the base of accretion columns after the impacts. Nevertheless, we can infer the expected size and evolution of the hotspots and the latitudes where the spots are located from the simulations.

Fig. 2.9 shows maps of particle number density close to the stellar surface after about 60 hours of evolution (when the accretion columns are well developed). During the initial transient phase, only a few (one or two) small and faint hotspots are present on the stellar surface, each corresponding to an accretion column (Fig. 2.2 D-E). At later times, the number of accretion columns in general increase following the disk perturbation that is due to the flares (Fig. 2.2 F). The number of hotspots, however, does not increase with the number of accretion columns, and no more than four spots are visible on the stellar surface during the whole evolution (see Fig. 2.9). The accretion streams interact with each other and often merge to form larger accretion columns before impact (Fig. 2.2 F). This complex dynamics is typical of accretion in the strongly unstable regime, where smaller tongues merge and form one or two larger tongues (e.g., Blinova et al. 2016). As a result, the spots are larger at later times.

In the reference case (FL-REF), two prominent hotspots are evident in the visible hemisphere of the star (top panel of Fig. 2.9) both with a density of around 3×10^{10} cm^{-3} (the shock-heated plasma after impact is expected to be four times denser in strong-shock conditions; e.g., Sacco et al. 2010). A slightly fainter (density of about 10^{10} cm^{-3}) spot is also present in the northern hemisphere. The spots cover a significant portion of the stellar surface ($\approx$ 20 %). Simulation FL-HD (middle panel of Fig. 2.9) shows a similar density structure on the stellar surface. In this case, three large hotspots with a density of between 10^{10} and 5×10^{10} cm^{-3} are present in the visible hemisphere of the star. In this case, the filling factor of the spots is $\approx$ 30 %. Run FL-LF presents a density structure on the stellar surface that is significantly different than in the other two cases. The density contrast of the spots is much

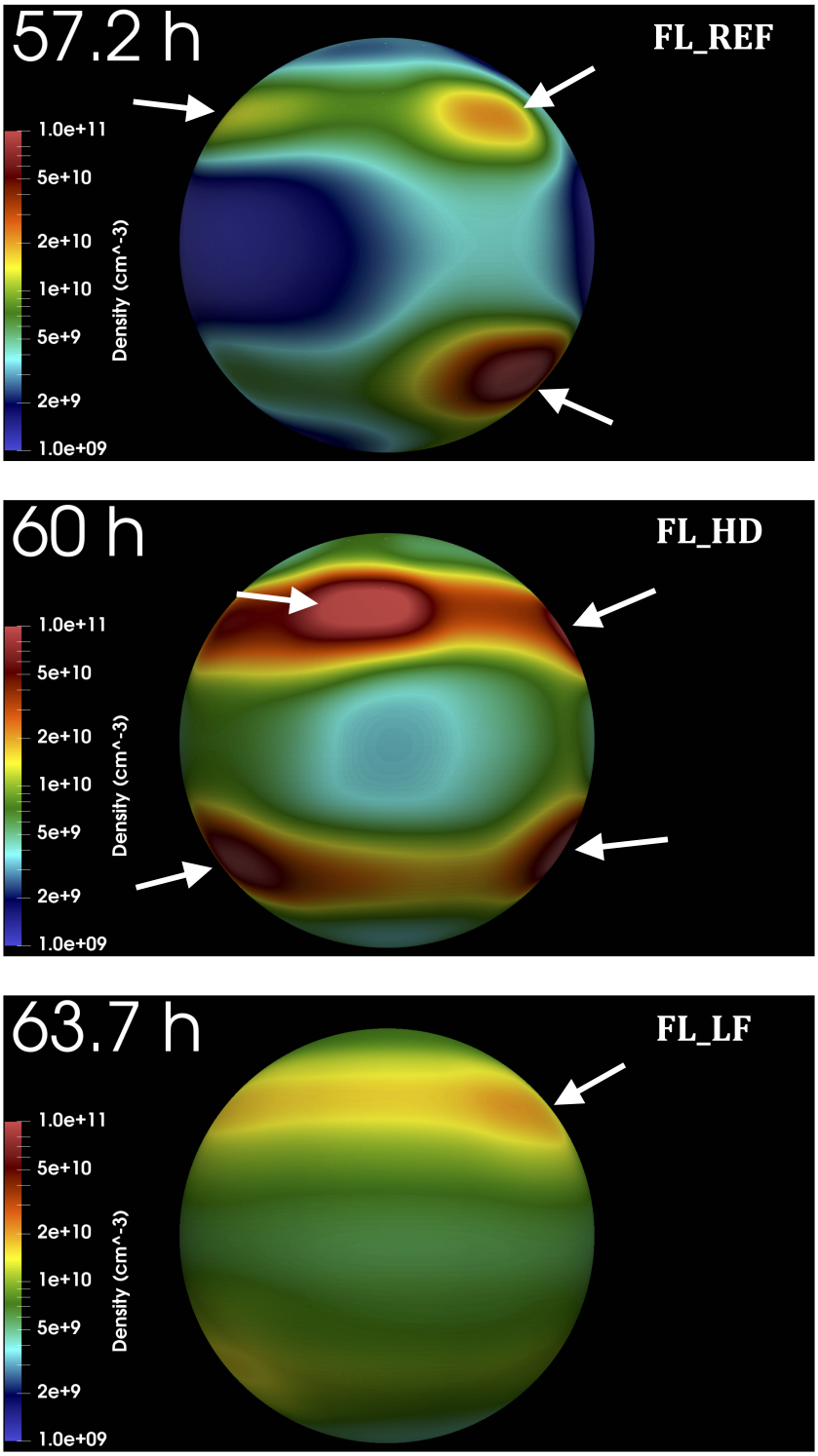

Figure 2.9 – Maps of particle number density in log scale close to the stellar surface after about 60 hours of evolution for runs FL-REF (upper panel), FL-HD (middle panel), and FL-LP (lower panel). The high-density regions (pointed at by white arrows) correspond to accretion columns impacting onto the stellar surface. Runs FL-REF and FL-HD exhibit clear hotspots, whereas in run FL-LF, the matter is more diffused and the contrast in density is weaker. (Colombo et al. 2019c).

weaker than in runs FL-REF and FL-HD. A main hotspot with density $\rho \approx 2 \times 10^{10}$ cm^{-3} and two less dense ($\rho \approx 10^{10}$ cm^{-3}) and smaller spots are present in the visible hemisphere. In this case, the filling factor of the spots is lower than 10 %.

Fig. 2.9 also shows that the hotspots are characterized by a dense inner core that is surrounded by lower density material as found by Romanova et al. (2004b) (see also Bonito et al. 2014). The spots are clearly visible in runs FL-REF and FL-HD (in general, yielding higher accretion rates); in run FL-LF, the accreted matter is more diffuse throughout the entire stellar surface and the spots have a lower contrast in density. In all the explored cases, the accretion occurs preferentially at high latitudes and the hotspots are located above (below) 40° (−40°); this is an effect of the magnetic field configuration chosen for the model (see Sect. 2.2 and, e.g., Romanova et al. 2011a). More specifically, high-latitude hotspots are favored when dipole and octupole components are parallel (e.g., Romanova et al. 2011a); conversely, if dipole and octupole components are antiparallel, low-latitude spots are favored (e.g., Donati et al. 2011). Earlier 3D simulations of accretion onto stars with dipole-plus-octupole aligned components (as in our case) have shown that the octupole component dominates in driving matter closer to the star, guiding the flows toward the high-latitude poles, and part of the matter into octupolar belts or rings (e.g., Long et al. 2008, 2011; Romanova et al. 2011a,b). As a result, the shape and position of the hotspots differ from those expected in a pure dipolar case, where the spots are typically observed at intermediate latitudes. In our simulations, we observe that initially, the matter flows into accretion streams guided by the dipole magnetic field. Then, the trajectory of the flows is sligthly redirected in proximity of the star, at distances below $\approx 1.7 R_\star$, by the dominant octupole component.

2.3.5 LIMITS OF THE MODEL

Our setup is analogous to others that have often been used in the literature (e.g., Romanova et al. 2002; Orlando et al. 2011) and is appropriate to describing the stellar-disk system in the context of young accreting stars. Nevertheless, a number of simplifications and assumptions have been made that we discuss in the following.

First, many works (e.g., Gregory et al. 2010; Gregory & Donati 2011) suggested that a stellar magnetic field can have a more complex configuration than we adopted here, namely an aligned octupole-dipole. In addition, in our setup, the initial magnetic field configuration does not account for the twisting and expansion of the field lines driven by the differential rotation of the disk and the different rotation period of the disk with respect to the star. A more complex magnetic field configuration is expected to change the dynamics of accretion streams described here, leading to a possibly more complex pattern of accretion. Moreover, we expect that the flares are generated by phenomena such as magnetic reconnection (see Sect. 1). For this reason, in the region where the magnetic field may generate a heat release, we expect an even more complex configuration than that assumed in our simulations. Then, the magnetic confinement of the hot plasma might be more efficient than in our simulations; this should enhance the effects of flare energy deposition in the system.

The description of the viscosity of the disk is simplified. Simulations of MRI suggests that the disk viscosity can be highly inhomogeneous and depending on time (Balbus 2003).

However, the timescale considered here (80 hours) is negligible compared to the viscosity timescale (several stellar periods, e.g., Romanova et al. 2002; Zanni & Ferreira 2009), we therefore do not expect to observe any effects considering a more realistic viscosity. Last, the description in terms of geometry and duration of the heat release that generates the single flare is idealized (see Sect. 2.2.3). We expect that the geometry of the heat release strongly depends on the specific magnetic field configuration at the site where the energy release occurs. Moreover, in realistic conditions we do not expect that each heat release would have the same duration as we have assumed. Nevertheless, we are not interested in a detailed study of the flare evolution here, but only in its consequences in terms of dynamical perturbation of the disk. From this point of view, the flares we simulated produce realistic perturbations.

2.4 Summary and conclusions

We investigated the effects of an intense flaring activity localized in proximity of the accretion disk of a CTTS. To this end, we adopted the 3D MHD model presented in Paper I, a magnetized protostar surrounded by a Keplerian accretion disk. The model has been adapted to include a storm of flares with low to intermediate intensity that occurs in proximity of the disk. The model takes into account all the relevant physical processes: stellar gravity, viscosity of the disk, thermal conduction, radiative losses from optically thin plasma, and a parametrized heating function to trigger the flares. We explored cases with different disk densities and different levels of flaring activity. Our results lead to the following conclusions.

- The coronal activity due to a series of low to intermediate flares that occur in proximity of the disk surface heats the disk material to temperatures of several million degrees. Part of this hot plasma is channeled and flows in magnetic loops that link the inner part of the disk to the central protostar; the remaining part of the heated plasma is poorly confined by the magnetic field (especially in flares that occur at larger distances from the star) and escapes from the system, carrying away mass and angular momentum. The coronal loops generated by the flares have typical lengths on the order of 10^{11} cm, maximum temperatures ranging between 10^8 K and 10^9 K, and a lifetime of about 10 hours. These characteristics are similar to those derived from the analysis of luminous X-ray flares observed in young low-mass stars (e.g., Favata et al. 2005). The escaping disk material contributes to increase the plasma outflow from the system with mass-loss rates $M_{loss} = 10^{-10} M_\odot$ yr^{-1} and angular momentum loss rate $L_{loss} = 10^6 - 10^7$g cm^{-2}yr^{-1}. The disk material, either confined in loops or escaping from the star, forms a tenuous hot corona extending from the central protostar to the inner portion of the disk.

- The circumstellar disk is heavily perturbed by the flaring activity. In the aftermath of

the flares, disk material evaporates in the outer stellar atmosphere under the effect of the thermal conduction. As previously stated in Paper I, overpressure waves are generated by the heat pulses in the disk at the footpoints of the hot loops that form the corona. The overpressure waves travel through the disk and distort its structure. Eventually, the overpressure waves can reach the side of the disk opposite to where heat pulses were injected. There, the overpressure waves can push the disk material out of equilibrium to form funnel flows that accrete disk material onto the protostar. We found that the effects of the overpressure waves are larger in disks that are less dense and for a higher frequency of flares. This type of accretion process starts about 20 hours after the first heat pulse, which is a timescale much shorter than that required by the disk viscosity to trigger the accretion. The accretion rates derived by the simulations range between 10^{-10} and $10^{-9}\,M_{\odot}\,yr^{-1}$. We found that the higher the disk density, the higher the accretion rate. The accretion rates are comparable with those inferred from observations of low-mass stars and brown dwarfs and in some solar mass accretors (Herczeg & Hillenbrand 2008; Curran et al. 2011).

- The accretion columns generated by the flaring activity on the disk have a complex dynamics and a lifetime ranging between a few hours and tens of hours. They can be perturbed by the flaring activity itself; for instance, a flare that occurs close to an accretion column can disrupt it or otherwise increase the amount of downfalling plasma. The streams can also interact with each other if they are sufficiently close, possibly merging into larger streams. As a result of this complex dynamics, the streams are highly inhomogeneous, with a complex density structure (see Fig. 2.6), and clumped, with clumps of typical size comparable to the section of the accretion column. In general, they have a dense inner core surrounded by lower density material, as has also been found by Romanova et al. (2004b). These findings support the idea that the persistent low-level hour-timescale variability observed in CTTSs reflects the internal clumpiness of the streams (Gullbring et al. 1996; Safier 1998; Bouvier et al. 2007; Giardino et al. 2007; Cranmer 2009).

Our simulations open a number of interesting questions. The hot plasma generated by the flares produces a hot extended corona that irradiates strong X-rays with a different spatial distribution than in the standard scenario of a corona confined to the stellar surface. A corona above the disk irradiates the disk from above with near normal incidence; the radiation reaches outer regions of the disk that may be shielded from the stellar-emitted X-rays. This may influence the chemical and physical evolution of the disk in a different way, with important consequences, for instance, on the formation of planets. This effect can be even more relevant than that due to X-ray emission from the base of protostellar jets located at larger distances from the disks (hundreds of astronomical units; Bonito et al. 2007). In addition, the irradiation produced by the flares can also increase the ionization level of the disk. As a result, a better coupling between magnetic field and plasma can be realized, which might increase the MRI efficiency.

CHAPTER 3

Radiation Hydrodynamics in PLUTO

Modeling the dynamics of most astrophysical structures requires an adequate description of the radiation-matter interaction. Since 1992 (Stone et al. 1992), several numerical (magneto)hydrodynamics codes were upgraded with a radiation module to fulfill this request. However, those among them that use either the flux-limited diffusion (FLD) or the M1 radiation moment approaches are today restricted to the local thermodynamic equilibrium (LTE). This assumption may not be valid in some astrophysical cases.

In this chapter, we present an upgraded version of the radiation module for PLUTO, originally developed by Kolb et al. (2013) in the LTE approximation, using the flux limited diffusion (FLD) method with the frequency-integrated comoving-frame radiation quantities. We expand the capabilities of this module, so that it can now allow for non-LTE regimes. Our implementation is validated through different tests. The agreement with the analytical solutions (when available) is good, with a maximum discrepancy of 7%. As a first application, we prove that the non-LTE approach is of paramount importance to properly model accretion shock structures.

3.1 Introduction

A direct coupling of the radiation effects to the hydrodynamic equations (RHD) or even the magnetohydrodynamic equations (RMHD) requires to solve the radiative transfer equation (RTE) and, in non-local thermodynamic equilibrium (non-LTE or NLTE) regimes, the kinetic equilibrium equations, at each time step, in order to infer the necessary radiative quantities that describe the momentum energy coupling between matter and radiation. However, this is a challenge that is, still to date, far beyond the current capabilities of computers. The main reason is that the RTE is an integro-differential equation, whose unknown, the specific intensity, depends on seven variables in a three-dimensional description (e.g., Pomraning 1973; Mihalas & Mihalas 1984; Castor 2004; Hubeny & Mihalas 2014). Fully solving the 3D radiative transfer equation itself requires a dedicated approach (e.g., Ibgui et al. 2013) that can be used for the generation of synthetic spectra, without coupling to hydrodynamic evolution.

A work around is to solve directly the equations that involve the radiation moments. These are obtained from angular moments of the RTE. Such an approach entails the creation of a hierarchy of moments, and necessitates the use of closure relations.

The most accurate of the radiation moment techniques is the variable Eddington tensor (VET) method (Stone et al. 1992; Gehmeyr & Mihalas 1994; Gnedin & Abel 2001; Hayes & Norman 2003; Hubeny & Burrows 2007; Jiang et al. 2012). The method has been applied to the total, or frequency-integrated, radiation moment equations. The Eddington tensor is defined as the ratio of the radiation pressure to the radiation energy. The method consists in solving the moment equations, while assuming that the Eddington tensor is known. Then,

once the structure of the medium is determined, the Eddington tensor is updated by solving the RTE with the short-characteristics method (Davis et al. 2012). Despite its good precision, this method is very costly from the computational point of view.

Another technique, less accurate than the VET method, but much cheaper from the computational point of view, is the so-called M1 approximation (Levermore 1984; Dubroca & Feugeas 1999). The difference with the VET method, for the total radiation moment equations, is that the Eddington tensor is provided by an analytical closure relation; the RTE is not solved. The M1 method has been implemented in several multidimensional RHD or RMHD codes, not only in the frequency-integrated approach (HERACLES: González et al. 2007, ATON: Aubert & Teyssier 2008, RAMSES: Rosdahl et al. 2013, ATHENA: Skinner & Ostriker 2013, PLUTO: Melon Fuksman & Mignone 2019), but also in the multigroup approach (HERACLES: Vaytet et al. 2013, FORNAX: Skinner et al. 2019).

Finally, we mention the third, radiation moment based, technique: the Flux-Limited Diffusion approximation (Alme & Wilson 1973; Levermore & Pomraning 1981). This method has been implemented in many multidimensional RHD or RMHD codes in astrophysical context, in the frequency-integrated approach (ZEUS: Turner & Stone 2001, ORION: Krumholz et al. 2007, V2D: Swesty & Myra 2009, NIRVANA: Kley et al. 2009, RAMSES: Commerçon et al. 2011b, CASTRO: Zhang et al. 2011, PLUTO: Kolb et al. 2013; Flock et al. 2013), and in the multigroup approach (CRASH: van der Holst et al. 2011, CASTRO: Zhang et al. 2013, FLASH: Klassen et al. 2014, RAMSES: González et al. 2015). Though FLD is less accurate than M1, especially in the optically thin regions, and it is not able to treat properly the shadows, it is the most widely used method in the R(M)HD codes, because it is the simplest one, the most robust, the most efficient in terms of computational cost, and provides very good results in flows where optically thick regions are of paramount importance. This method is discussed in detail in Sect. 3.6.4

The main focus of the first part of this chapter (Sects. 3.2-3.7) is to introduce the general equations of radiation hydrodynamic (RHD) and to guide, step by step, the reader through the assumptions and the approximations made until we obtain the RHD equations actually solved by our version of the module. In Sect. 3.8, we explain the theoretical model used to generate the opacity and the radiative power loss databases used by our module. In Sect. 3.9, we describe the numerical implementation used in the module. In Sect. 3.10, we validate the modifications made in the code. The new implementation of the code has been successfully tested, with the most common RHD tests, and in Sect. 3.11, we compare the two radiative shock structures obtained by letting evolve a given flow under, respectively, forced LTE regime, and non-LTE regime. Finally, in Sect. 3.12, we draw our conclusions.

This work is the subject of a paper accepted for publication in Astronomy & Astrophysics (Colombo et al. 2019a).

3.2 Definitions and basic concepts

Before going deeply in the discussion of the general equations of radiation hydrodynamics it is useful to introduce the reader some important terms that will be used further in the discussion.

The first quantity to define is the specific intensity I_ν. It is a function of three spatial (x,y,z) and two angle coordinates (θ,ϕ) , the frequency ν, and the time t; seven coordinates in all. To better understand the physical meaning of I_ν imagine an ideal experiment (this explanation follows from Castor 2004). The setup of the experiment is shown in Fig. 3.1.

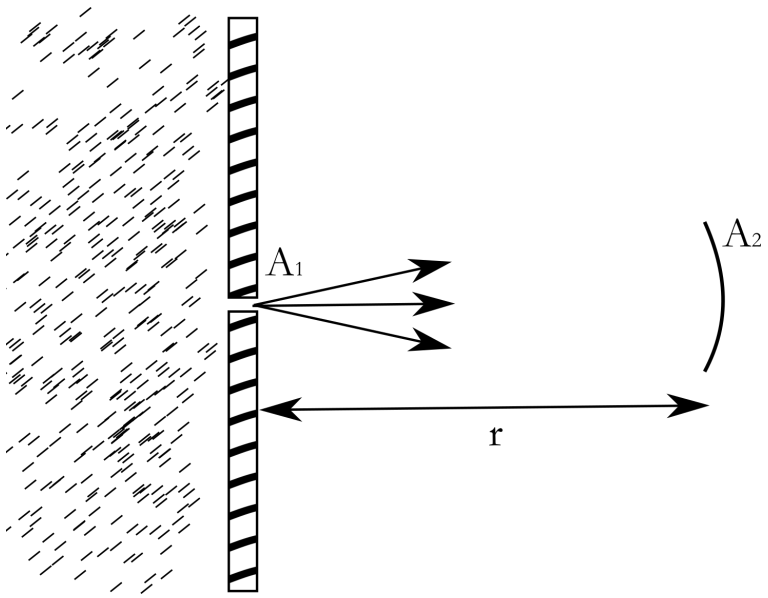

Figure 3.1 – Sketch (readapted from Castor 2004) of the ideal experiment useful to define the physical meaning of I. The setup is composed of a wall with a small hole A_1 compared to the aperture of the detector A_2.

The setup is composed of a wall with a small hole of surface A_1; the wall separates a region where a radiation is present from a completely empty region. In the empty region, a detector of radiation of size A_2, is located at distance r from the wall. The distance r is much larger than the size of the aperture. The wall is perpendicular to the direction we want to measure. The idea is twofold:

- We want to measure the energy coming from one direction;
- The single direction must be perpendicular to the emitting surface A_1.

The intensity I_ν is defined such that the energy collected by the detector, in a time Δt in

the range of frequency $\Delta\nu$, is:

$$\Delta E = I_\nu \frac{A_1 A_2}{r^2} \Delta t \Delta\nu \tag{3.1}$$

Noticing that A_2/r^2 is the solid angle $d\Omega$ subtended by A_2 at the aperture, we define the intensity I_ν as the energy crossing a unit area at a given point per unit time per unit frequency and per unit solid angle in the direction of interest.

Together with the intensity it is possible to define its angular moments, defined as:

$$E_\nu = \frac{1}{c}\int_{4\pi} I_\nu d\Omega \qquad \text{erg cm}^{-3}\text{Hz}^{-1} \tag{3.2}$$

$$\mathbf{F}_\nu = \int_{4\pi} \mathbf{n} I_\nu d\Omega \qquad \text{erg cm}^{-2}\text{s}^{-1}\text{Hz}^{-1} \tag{3.3}$$

$$\mathbb{P}_\nu = \frac{1}{c}\int_{4\pi} \mathbf{n}\mathbf{n} I_\nu d\Omega \qquad [\text{p}]\ \text{cm}^{-2}\text{s}^{-1}\text{Hz}^{-1} \tag{3.4}$$

The first (Eq. 3.2) represents the radiation energy density. The second (Eq. 3.3) is the vector flux, i.e. the energy flux for a radiation with frequency ν. The third (Eq. 3.4) is the radiation pressure, that is the pressure due to radiation at the frequency ν. For further calculations in this manuscript, the direction of propagation $\mathbf{n}$ in Eqs. 3.2-3.4, is defined as $\mathbf{n} = \sin\Theta\cos\Phi e_x + \sin\Theta\sin\Phi e_y + \cos\Theta e_z$, where Θ and Φ are the colatitude and the longitude, respectively.

3.3 THE TRANSPORT EQUATION

If we consider a bundle of radiation moving in an empty space, it is straightforward to understand that the intensity of the radiation will not change as the photons move. However, if the radiation moves in a not empty space it could be absorbed and/or emitted by the matter. This effects can be described by the transport equation.

Before introducing this equation it is better to chose a notation for the direction of propagation of radiation. Here, in analogy to (Castor 2004), we remind to the reader that we use $\mathbf{n}$ as direction of propagation, defined as $\mathbf{n} = \sin\Theta\cos\Phi e_x + \sin\Theta\sin\Phi e_y + \cos\Theta e_z$, where Θ and Φ are the colatitude and the longitude, respectively.

We can start assuming that there is no absorption or emission, in this case I_ν remains constant.

$$I_\nu(\mathbf{r} + \mathbf{n}c\tau, \mathbf{n}, t + \tau) = I_\nu(\mathbf{r}, \mathbf{n}, t) \tag{3.5}$$

where $\mathbf{r}(x, y, z)$ represent the position vector. We expand in Taylor series the left-hand side of Eq. 3.5, we neglect the term of order higher than τ^2. We subtract $I_\nu(\mathbf{r}, \mathbf{n}, t)$ and divide by $c\tau$, and we obtain

$$\frac{1}{c}\frac{\partial I_\nu}{\partial t} + \mathbf{n}\cdot\nabla I_\nu = 0 \tag{3.6}$$

Eq. 3.6 is the equation of transport without the terms of sink and source of radiation. If we define χ_ν (cm^{-1}) and η_ν ($erg\,cm^{-3}\,sr^{-1}\,s^{-1}\,Hz^{-1}$) as the extinction and emission coefficients (see later in the text), we obtain the most general transport equation

$$\frac{1}{c}\frac{\partial I_\nu}{\partial t} + \mathbf{n}\cdot\nabla I_\nu = \eta_\nu - \chi_\nu I_\nu \tag{3.7}$$

This is an equation of conservation for the radiation intensity in the laboratory frame. Choosing this frame has the advantage of simplicity in the partial derivative, but the disadvantage of the complexity in the absorption χ_ν and emission η_ν coefficients. Choosing the comoving frame, also known as the fluid frame, i.e., the frame moving with the macroscopic velocity of the fluid, has advantages and disadvantages exchanged.

Obtaining the equation of transport in the co-moving frame is needs some algebra and physical insight. The idea is to take into account the Doppler effect, the aberration effects and to rewrite I_ν, χ_ν and η_ν in the co-moving frame. This leads to (Mihalas & Mihalas 1984; Munier & Weaver 1986):

$$\begin{aligned}
&\frac{1}{c}\left(1+\mathbf{n}_0\cdot\frac{\mathbf{u}}{c}\right)\frac{\partial I_0}{\partial t} + \mathbf{n}_0\cdot\nabla I_0 + \frac{\mathbf{u}}{c}\cdot\nabla I_0 - \frac{1}{c}\left(\mathbf{n}_0\cdot\frac{\mathbf{a}}{c} + \mathbf{n}_0\cdot(\nabla\mathbf{u}\mathbf{n}_0)\right)\frac{\partial(\nu_0 I_0)}{\partial\nu_0}\\
&+\frac{1}{c}\nabla_{\mathbf{n}_0}\cdot\left\{\left[\frac{1}{c}\left((\mathbf{n}_0\cdot\mathbf{a})\,\mathbf{n}_0-\mathbf{a}\right)+(\mathbf{n}_0\cdot(\nabla\mathbf{u}\mathbf{n}_0))\,\mathbf{n}_0-(\mathbf{n}_0\cdot\nabla)\,\mathbf{u}\right] I_0\right\}\\
&+\frac{1}{c}\left(2\mathbf{n}_0\cdot\frac{\mathbf{a}}{c}+\nabla\cdot\mathbf{u}+\mathbf{n}_0\cdot(\nabla\mathbf{u}\mathbf{n}_0)\right) I_0 = \eta_0(\mathbf{r},t;\mathbf{n}_0,\nu_0) - \chi_0 I_0
\end{aligned} \tag{3.8}$$

Where, $\mathbf{a} = \partial\mathbf{u}/\partial t$ is the local acceleration of the fluid, and for simplicity the comoving frame frequency ν_0 subscript, indicating that all the radiative quantities are frequency-dependent, is omitted.

3.4 The general radiation hydrodynamic equations

The full monochromatic equations of radiation hydrodynamic (RHD) in the non-relativistic approximation describes the conservation of mass, matter momentum and total matter en-

ergy:

$$\frac{\partial \rho}{\partial t} + \nabla \cdot (\rho\, \mathbf{u}) = 0\,, \tag{3.9a}$$

$$\frac{\partial}{\partial t}(\rho\, \mathbf{u}) + \nabla \cdot (\rho\, \mathbf{u}\mathbf{u} + p\, \mathbb{I}) = \rho\, \mathbf{g} + \mathbf{G}_0\,, \tag{3.9b}$$

$$\frac{\partial}{\partial t}\left(\mathbb{E} + \tfrac{1}{2}\rho\, u^2\right) + \nabla \cdot \left[\left(\mathbb{E} + \tfrac{1}{2}\rho\, u^2 + p\right)\, \mathbf{u}\right] = \rho\, \mathbf{g}\cdot\mathbf{u} + \mathbf{G}_0 \cdot \mathbf{u} + c\, G_0^0. \tag{3.9c}$$

where ρ represents the mass density of the fluid, $\mathbf{u}$ the velocity, p the pressure, $\mathbb{I}$ the identity matrix, $\mathbf{g}$ the gravity acceleration, $\mathbb{E}$ the matter internal energy density, c the speed of light and G_0^0 and $\mathbf{G}_0$, respectively, the time component and the space components of the radiation four-force density vector, i.e., G_0^0 represents the net rate of radiation energy input into the matter per unit volume, while each component of $\mathbf{G}_0$ represents the net rate of momentum input into the matter per unit volume in a specific direction $\mathbf{i}$. G_0^0 and $\mathbf{G}_0$ are defined as (note that in this manuscript the notation adopted by Mihalas & Mihalas (1984) is used, where the subscript "0" refers to comoving frame radiation quantities):

$$G_0^0(\mathbf{r}, t) \equiv \frac{1}{c}\int_0^\infty d\nu_0 \oint_{4\pi} (\chi_0 I_0 - \eta_0)\, d\Omega_0, \tag{3.10a}$$

$$\mathbf{G}_0(\mathbf{r}, t) \equiv \frac{1}{c}\int_0^\infty d\nu_0 \oint_{4\pi} (\chi_0 I_0 - \eta_0)\, \mathbf{n}_0 d\Omega_0, \tag{3.10b}$$

where, $I_0(\mathbf{r}, t; \mathbf{n}_0, \nu_0)$ is the comoving-frame specific intensity defined at position $\mathbf{r}$, time t, for the comoving-frame direction unit vector $\mathbf{n}_0$, and at the comoving-frame frequency ν_0, and where $\chi_0(\mathbf{r}, t; \mathbf{n}_0, \nu_0)$ and $\eta_0(\mathbf{r}, t; \mathbf{n}_0, \nu_0)$ are, respectively, the comoving-frame extinction coefficient (cm^{-1}) and emission coefficient or emissivity ($\mathrm{erg\ cm^{-3}\ s^{-1}\ sr^{-1}\ Hz^{-1}}$):

$$\chi_0(\mathbf{r}, t; \mathbf{n}_0, \nu_0) = \kappa_0^{\mathrm{th}}(\mathbf{r}, t; \mathbf{n}_0, \nu_0) + \kappa_0^{\mathrm{sca}}(\mathbf{r}, t; \mathbf{n}_0, \nu_0)\ , \tag{3.11a}$$

$$\eta_0(\mathbf{r}, t; \mathbf{n}_0, \nu_0) = \eta_0^{\mathrm{th}}(\mathbf{r}, t; \mathbf{n}_0, \nu_0) + \eta_0^{\mathrm{sca}}(\mathbf{r}, t; \mathbf{n}_0, \nu_0)\ , \tag{3.11b}$$

where $\kappa_0^{\mathrm{th}}(\mathbf{r}, t; \mathbf{n}_0, \nu_0)$ is the comoving-frame thermal absorption coefficient, $\kappa_0^{\mathrm{sca}}(\mathbf{r}, t; \mathbf{n}_0, \nu_0)$ the scattering coefficient, $\eta_0^{\mathrm{th}}(\mathbf{r}, t; \mathbf{n}_0, \nu_0)$ the thermal emission coefficient, and $\eta_0^{\mathrm{sca}}(\mathbf{r}, t; \mathbf{n}_0, \nu_0)$ the scattering emission coefficient.

The basic idea is to solve Eq. (3.9a), (3.9b), (3.9c), using an equation of state (EOS) and an equation for matter internal energy (or caloric equation of state) as closure relations for the system. The whole system of equations has to be coupled with the full radiative transfer equations (RTE), that is used to determine the specific intensity I_0 and then G_0^0 and $\mathbf{G}_0$.

Even if this approach is correct, unfortunately it is not feasible with the current computer capabilities. In fact, solving only the radiative transfer equations itself is a challenging task, that requires a dedicated approach (e.g. Ibgui et al. 2013). So, in order to solve the RHD system we

have to reduce the calculation burden. One possibility is to work with angularly integrated radiation quantities, in this way we can reduce the number of dimensions in the problem. This leads to the so-called radiation moment equation approach that will be discussed in the next session.

3.5 The moment approach

3.5.1 The monochromatic moment equations

The results of the angular integration of Eq. 3.8 provide two monochromatic comoving-frame radiation moment equations. These equations are valid to $O(u/c)$ and describe the radiation energy and radiation momentum conservation (Mihalas & Mihalas 1984). For the radiation energy conservation we have

$$\frac{\partial E_{\nu_0}}{\partial t} + \nabla\cdot\mathbf{F}_{\nu_0} + \mathbf{u}\cdot\frac{\partial}{\partial t}\left(\frac{\mathbf{F}_{\nu_0}}{c^2}\right) + \nabla\cdot\left(E_{\nu_0}\,\mathbf{u}\right) - \frac{\partial}{\partial\nu_0}\left[\nu_0\left(\mathbb{P}_{\nu_0}:\nabla\mathbf{u} + \left(\frac{\mathbf{F}_{\nu_0}}{c^2}\right)\cdot\mathbf{a}\right)\right] + \mathbb{P}_{\nu_0}:\nabla\mathbf{u} + 2\left(\frac{\mathbf{F}_{\nu_0}}{c^2}\right)\cdot\mathbf{a} = -c\,G^0_{\nu_0} \tag{3.12}$$

and for the radiation momentum conservation

$$\frac{\partial}{\partial t}\left(\frac{\mathbf{F}_{\nu_0}}{c^2}\right) + \nabla\cdot\mathbb{P}_{\nu_0} + (\mathbf{u}\cdot\nabla)\left(\frac{\mathbf{F}_{\nu_0}}{c^2}\right) + \left(\frac{\mathbf{F}_{\nu_0}}{c^2}\cdot\nabla\right)\mathbf{u} + (\nabla\cdot\mathbf{u})\left(\frac{\mathbf{F}_{\nu_0}}{c^2}\right) + \frac{\partial\mathbb{P}_{\nu_0}}{\partial t}\frac{\mathbf{u}}{c^2} - \frac{1}{c^2}\frac{\partial}{\partial\nu_0}\left[\nu_0\left(\mathbb{P}_{\nu_0}\,\mathbf{a} + \mathbb{Q}_{\nu_0}:\nabla\mathbf{u}\right)\right] + \frac{1}{c^2}\left(\mathbb{P}_{\nu_0}\,\mathbf{a} + E_{\nu_0}\,\mathbf{a}\right) = -\mathbf{G}_{\nu_0}\,, \tag{3.13}$$

where $G^0_{\nu_0}$ and $\mathbf{G}_{\nu_0}$ are the monochromatic versions of the radiation four-force density vector $G^\alpha_0 \equiv (G^0_0, \mathbf{G}_0)$:

$$G^0_{\nu_0} \equiv \frac{1}{c}\oint_{4\pi} d\Omega_0\ (\chi_0 I_0 - \eta_0) \quad ; \quad G^0_0 = \int_0^\infty G^0_{\nu_0}\, d\nu_0 \tag{3.14a}$$

$$\mathbf{G}_{\nu_0} \equiv \frac{1}{c}\oint_{4\pi} d\Omega_0\ (\chi_0 I_0 - \eta_0)\ \mathbf{n}_0\,; \quad \mathbf{G}_0 = \int_0^\infty \mathbf{G}_{\nu_0}\, d\nu_0\,, \tag{3.14b}$$

and where the first three moments E_{ν_0}, $\mathbf{F}_{\nu_0}$ and $\mathbb{P}_{\nu_0}$, are defined in Eq. 3.2, 3.3 and 3.4 respectively. $\mathbb{Q}_{\nu_0}$ is the third order momentum, defined as:

$$\mathbb{Q}_{\nu_0} = \int_{4\pi} \mathbf{nnn} I_{\nu_0} d\Omega\,. \tag{3.15}$$

The radiation moment approach consists of solving the equations of conservation of mass, momentum and plasma energy (Eqs. 3.9a,3.9b,3.9c), with an equation of state (EOS), a caloric equation of state and the two radiation moment equations (Eqs. 3.12, 3.13). The tricky part

of this approach is that it requires a closure relation that links the four radiation moments. Another problem related to this approach is that in principle one should solve the radiation equations for each frequency. Unfortunately, this task is still prohibitive with the current computers' capabilities. To overcome this issue one consider in general the total, or frequency-integrated, version of the two radiation moment equations. A more detailed approach could be the multigroup approach (Vaytet et al. 2013; Skinner et al. 2019).

3.5.2 The total moment equations

Under the total approach (i.e. integrating all the terms depending on frequency) the radiation moment equations become

$$\frac{\partial E_0}{\partial t} + \nabla \cdot \mathbf{F}_0 + \mathbf{u} \cdot \frac{\partial}{\partial t}\left(\frac{\mathbf{F}_0}{c^2}\right) + \nabla \cdot (E_0\,\mathbf{u}) + \mathbb{P}_0 : \nabla \mathbf{u} + 2\left(\frac{\mathbf{F}_0}{c^2}\right) \cdot \mathbf{a} = -c\, G_0^0 \tag{3.16a}$$

$$\frac{\partial}{\partial t}\left(\frac{\mathbf{F}_0}{c^2}\right) + \nabla \cdot \mathbb{P}_0 + (\mathbf{u} \cdot \nabla)\left(\frac{\mathbf{F}_0}{c^2}\right) + \left(\frac{\mathbf{F}_0}{c^2} \cdot \nabla\right)\mathbf{u} + (\nabla \cdot \mathbf{u})\left(\frac{\mathbf{F}_0}{c^2}\right) + \frac{\partial \mathbb{P}_0}{\partial t}\frac{\mathbf{u}}{c^2} + \frac{1}{c^2}\left(\mathbb{P}_0\,\mathbf{a} + E_0\,\mathbf{a}\right) = -\mathbf{G}_0 \tag{3.16b}$$

This approach is the first to be adopted in HD and MHD multi-dimension codes, for example: ZEUS (Stone et al. 1992; Turner & Stone 2001; Hayes & Norman 2003), ORION (Krumholz et al. 2007), HERACLES (González et al. 2007), RAMSES (Commerçon et al. 2011a), CASTRO (Zhang et al. 2011) and ATHENA (Skinner & Ostriker 2013). However, all these codes assume the local thermodynamic equilibrium (LTE) regime.

3.6 Approximations

3.6.1 The approximate radiation four-four density

Here, we focus on the assumptions that we can adopt to simplify the determination of the terms G_0^0 and $\mathbf{G}_0$ in the full energy and momentum radiation conservation equations 3.16a and 3.16b. We use the fact that we evaluate the absorption and emission coefficients in the comoving-frame.

Let us start with the energy term $cG^0_{\nu_0}$ in Eq. 3.9c. Using Eqs. 3.14, 3.11a and 3.11b, it can be written as:

$$\begin{aligned} c\, G^0_{\nu_0} = &\left(\oint_{4\pi} \kappa_0^{\rm th}(\mathbf{n}_0, \nu_0)\, I_0\, d\Omega_0 + \oint_{4\pi} \kappa_0^{\rm sca}(\mathbf{n}_0, \nu_0)\, I_0\, d\Omega_0\right) \\ &- \left(\oint_{4\pi} \eta_0^{\rm th}(\mathbf{n}_0, \nu_0)\, d\Omega_0 \quad + \oint_{4\pi} \eta_0^{\rm sca}(\mathbf{n}_0, \nu_0)\, d\Omega_0\right) \end{aligned} \tag{3.17}$$

where for the sake of simplicity we have omitted the full dependence of $(\mathbf{r}, t; \mathbf{n}_0, \nu_0)$ for the coefficients $\kappa_0^{\rm th}$, $\kappa_0^{\rm sca}$, $\eta_0^{\rm th}$, $\eta_0^{\rm sca}$ and I_0.

As a first step, it is possible to assume coherent and isotropic scattering. Mihalas & Auer (2001) have shown that

$$\eta_0^{\rm sca}(\nu_0) \;=\; \kappa_0^{\rm sca}(\nu_0) \oint_{4\pi} I_0(\mathbf{n}_0', \nu_0)\, \frac{d\Omega_0'}{4\pi} \tag{3.18}$$

As a consequence, both scattering terms are canceled out, and the term $cG_{\nu_0}^0$ become:

$$c\, G_{\nu_0}^0 \;=\; \oint_{4\pi} \kappa_0^{\rm th}(\mathbf{n}_0, \nu_0)\, I_0\, d\Omega_0 - \oint_{4\pi} \eta_0^{\rm th}(\mathbf{n}_0, \nu_0)\, d\Omega_0 \tag{3.19}$$

As a second step, it is possible to assume also that the thermal absorption is isotropic. In this way:

$$c\, G_{\nu_0}^0 \;=\; \kappa_0^{\rm th}(\nu_0) \oint_{4\pi} I_0\, d\Omega_0 - \oint_{4\pi} \eta_0^{\rm th}(\mathbf{n}_0, \nu_0)\, d\Omega_0 \tag{3.20}$$

Using these two assumptions, it is possible to write in the total approach:

$$c\, G_0^0 \;=\; c\, \kappa_{0E}\, E_0 - L_0 \tag{3.21}$$

where κ_{0E} is the energy-weighted mean opacity defined as:

$$\kappa_{0E} \;\equiv\; \frac{\int_0^\infty \kappa_{\nu_0}^{\rm th}\, E_{\nu_0}\, d\nu_0}{\int_0^\infty E_{\nu_0}\, d\nu_0} \tag{3.22}$$

and L_0 (erg cm^{-3} s^{-1}) is the radiation emission per unit volume and time (or radiative power loss):

$$L_0 \;\equiv\; \int_0^\infty \oint_{4\pi} \eta_0^{\rm th}(\mathbf{n}_0, \nu_0)\, d\Omega_0\, d\nu_0 \tag{3.23}$$

Now, we can focus on the comoving-frame space components $\mathbf{G}_0$ of the radiation four-force density vector. Analogously to G_0^0, using Eqs. 3.14, 3.11a and 3.11b, it can be written as:

$$\begin{aligned} c\, \mathbf{G}_{\nu_0} \;=\; & \left(\oint_{4\pi} \kappa_0^{\rm th}(\mathbf{n}_0, \nu_0)\, I_0\, \mathbf{n}_0\, d\Omega_0 + \oint_{4\pi} \kappa_0^{\rm sca}(\mathbf{n}_0, \nu_0)\, I_0\, \mathbf{n}_0\, d\Omega_0 \right) \\ & - \left(\oint_{4\pi} \eta_0^{\rm th}(\mathbf{n}_0, \nu_0)\, \mathbf{n}_0\, d\Omega_0 \quad + \oint_{4\pi} \eta_0^{\rm sca}(\mathbf{n}_0, \nu_0)\, \mathbf{n}_0\, d\Omega_0 \right) \end{aligned} \tag{3.24}$$

Also in this case we can use the same assumptions used for G_0^0 (i.e. coherent and isotropic scattering, isotropic thermal absorption) plus the assumption of isotropic thermal emission. Then, the emission terms vanish, so

$$c\, \mathbf{G}_{\nu_0} \;=\; \kappa_0^{\rm th}(\nu_0) \oint_{4\pi} I_0\, \mathbf{n}_0\, d\Omega_0 + \kappa_0^{\rm sca}(\nu_0) \oint_{4\pi} I_0\, \mathbf{n}_0\, d\Omega_0 \tag{3.25}$$

and we can write the following total relation:

$$\mathbf{G}_0 = \frac{1}{c}\,\mathbb{\chi}_{0F}\,\mathbf{F}_0 \tag{3.26}$$

where $\mathbb{\chi}_{0F}$ represents the flux-weighted mean opacity, which is defined as:

$$\mathbb{\chi}_{0F} = \begin{pmatrix} \chi_{0F}^{(1)} & 0 & 0 \\ 0 & \chi_{0F}^{(2)} & 0 \\ 0 & 0 & \chi_{0F}^{(3)} \end{pmatrix} \tag{3.27}$$

where (Mihalas & Auer 2001),

$$\chi_{0F}^{(i)} \equiv \frac{\int_0^\infty \chi_{\nu_0}\, F_{\nu_0}^{(i)}\, d\nu_0}{\int_0^\infty F_{\nu_0}^{(i)}\, d\nu_0} \tag{3.28}$$

with $\chi_{0F}^{(i)} \equiv 0$ if $\int_0^\infty F_{\nu_0}^{(i)}\, d\nu_0 = 0$.

3.6.2 The approximate mean opacities

From Eqs. 3.21 and 3.26 it follows that to calculate G_0^0 and $\mathbf{G}_0$ we need to know the mean opacities κ_{0E} and $\mathbb{\chi}_{0F}$. Unfortunately, these quantities are not known in advance, since they depend on the unknowns radiation energy E_{ν_0} and flux $\mathbf{F}_{\nu_0}$. To overcome this difficulty it is possible to work with mean values, which are functions of only the density ρ and the temperature T of the plasma.

We can start the discussion assuming to be in an optically thick medium, and in the equilibrium diffusion regime. This approximation is accurate as far as the free paths are small compared with other length scales (Castor 2004). Under this assumption, we know that (Mihalas & Mihalas 1984):

$$E_{\nu_0} = \frac{4\pi}{c}\, B_{\nu_0} \tag{3.29a}$$

$$\mathbf{F}_{\nu_0} = -\frac{4\pi}{3\chi_{\nu_0}}\, \nabla B_{\nu_0} \tag{3.29b}$$

where $B_{\nu_0} = B(\nu_0, T_0)$ is the Planck function at material temperature T_0. It follows from Eq. 3.29a that

$$\kappa_{0E} = \kappa_{0P} \tag{3.30}$$

where κ_{0P} is the *Planck mean opacity*, defined as:

$$\kappa_{0P} \equiv \frac{\int_0^\infty \kappa_{\nu_0}^{th}\, B_{\nu_0}\, d\nu_0}{\int_0^\infty B_{\nu_0}\, d\nu_0} \tag{3.31}$$

Integrating along frequency Eq. 3.29b, we find that:

$$\mathbf{F}_0 = -\frac{4\pi}{3\chi_{0R}}\nabla B_0 \tag{3.32}$$

where $B_0 = c a_R T_0^4/4\pi$ is the frequency-integrated Planck function, in which a_R is the radiation constant (or radiation density constant), and χ_{0R} is the *Rosseland mean opacity*, defined as:

$$\frac{1}{\chi_{0R}} \equiv \frac{\int_0^\infty \frac{1}{\chi_{\nu_0}}\frac{\partial B_{\nu_0}}{\partial T}\,d\nu_0}{\int_0^\infty \frac{\partial B_{\nu_0}}{\partial T}\,d\nu_0} \tag{3.33}$$

We can conclude that in the equilibrium diffusion regime, we can replace κ_{0E} in Eq. 3.21 with κ_{0P} and $\not{\chi}_{0F}$ with χ_{0R}. There is no such approximate functions for mean opacities in the optically thin regime. Then, we use this approximation from the optically thick to the optically thin regimes, giving thereby priority to optically thick parts of flows, as suggested by Krumholz et al. (2007), obtaining:

$$c\,G_0^0 = c\,\kappa_{0P}\,E_0 - L_0 \tag{3.34a}$$

$$\mathbf{G}_0 = \frac{1}{c}\,\chi_{0R}\,\mathbf{F}_0 \tag{3.34b}$$

Note that the Planck and Rosseland mean opacities can be calculated in advance, as functions only of density and temperature.

Finally, we are now able to write the full set of radiation hydrodynamic equations:

$$\frac{\partial \rho}{\partial t} + \nabla\cdot(\rho\,\mathbf{u}) = 0 \tag{3.35}$$

$$\frac{\partial}{\partial t}(\rho\,\mathbf{u}) + \nabla\cdot(\rho\,\mathbf{u}\mathbf{u} + p\,\mathbb{I}) = \rho\,\mathbf{g} + \frac{1}{c}\,\chi_{0R}\,\mathbf{F}_0\,, \tag{3.36}$$

$$\frac{\partial}{\partial t}\left(\mathbb{E} + \tfrac{1}{2}\rho u^2\right) + \nabla\cdot\left[\left(\mathbb{E} + \tfrac{1}{2}\rho u^2 + p\right)\mathbf{u}\right] = \rho\mathbf{g}\cdot\mathbf{u} + \frac{1}{c}\chi_{0R}\mathbf{F}_0\cdot\mathbf{u} + c\kappa_{0P}E_0 - L_0 \tag{3.37}$$

$$\frac{\partial E_0}{\partial t} + \nabla\cdot\mathbf{F}_0 + \mathbf{u}\cdot\frac{\partial}{\partial t}\left(\frac{\mathbf{F}_0}{c^2}\right) + \nabla\cdot(E_0\mathbf{u}) + \mathbb{P}_0 : \nabla\mathbf{u} + 2\frac{\mathbf{F}_0}{c^2}\cdot\mathbf{a} = L_0 - c\kappa_{0P}E_0 \tag{3.38}$$

$$\frac{\partial}{\partial t}\left(\frac{\mathbf{F}_0}{c^2}\right) + \nabla\cdot\mathbb{P}_0 + (\mathbf{u}\cdot\nabla)\left(\frac{\mathbf{F}_0}{c^2}\right) + \left(\frac{\mathbf{F}_0}{c^2}\cdot\nabla\right)\mathbf{u} + (\nabla\cdot\mathbf{u})\left(\frac{\mathbf{F}_0}{c^2}\right) + \frac{\partial\mathbb{P}_0}{\partial t}\frac{\mathbf{u}}{c^2} + \frac{1}{c^2}(\mathbb{P}_0\,\mathbf{a} + E_0\,\mathbf{a}) = -\frac{1}{c}\,\chi_{0R}\,\mathbf{F}_0 \tag{3.39}$$

3.6.3 SCALING OF TERMS IN THE RADIATION MOMENT EQUATIONS

The orders of magnitude of the terms involved in the LTE total radiation moment equations have been already evaluated in the comoving-frame equations by Mihalas & Mihalas (1984); Stone et al. (1992), and in the mixed-frame equations by Mihalas & Mihalas (1984); Krumholz et al. (2007); Skinner & Ostriker (2013). We apply here the same approach to the non-LTE radiation equations.

The three asymptotic physical regimes

We summarize the characteristics of the three asymptotic physical regimes, as classified by Mihalas & Mihalas (1984) and used by Krumholz et al. (2007) and Skinner & Ostriker (2013). We denote by ℓ the characteristic structural length at a given position and along a given direction in the flow, and $\lambda_p(\nu_0) \equiv 1/\chi_0(\nu_0)$ the photon mean free path (distance traveled by a photon before being thermally absorbed or scattered). The optical depth along the distance ℓ in the flow, at frequency ν_0, is $\tau(\nu_0) \equiv \chi_0(\nu_0)\,\ell = \ell/\lambda_p(\nu_0)$. We distinguish the free-streaming regime in an optically thin medium ($\tau(\nu_0) \ll 1$), where a photon can move freely in the medium at the speed of light, and the diffusion regime in an optically thick medium ($\tau(\nu_0) \gg 1$), where a photon travels one free path between interactions (thermal absorption or scattering) with matter. In the diffusion case, we differentiate two subcases. The first one is the static diffusion regime for media with negligible velocity. Photons, which are trapped in the material, diffuse in it through a random walk process. The second one is the dynamic diffusion regime for media with large enough velocity. Photons, which are also trapped in the material, can be advected by the material motion faster than they can diffuse. The distinction between these two subcases in an optically thick medium can be quantified by appropriate parameters (Mihalas & Klein 1982; Mihalas & Mihalas 1984; Krumholz et al. 2007; Skinner & Ostriker 2013). We introduce the fluid-flow timescale $t_f \equiv \ell/u_f$, the typical time for a fluid particle to cross distance ℓ at characteristic velocity u_f, the diffusion timescale $t_d \equiv \ell^2/(c\lambda_p)$, the typical time for a photon to cross distance ℓ through a random walk composed of steps of length λ_p (mean free path) covered at the speed of light (Mihalas & Mihalas 1984). The corresponding characteristic photon diffusion velocity is $u_d \equiv \ell/t_d$. We can then express quantitatively the physical distinction, discussed above, between the static diffusion regime, $u_d \gg u_f$ (equivalent to $t_d \ll t_f$), and the dynamic diffusion regime, $u_f \gg u_d$ (equivalent to $t_f \ll t_d$). We introduce a characteristic parameter, $\beta \equiv u_f/c \ll 1$ (nonrelativistic flow). This way, we can synthesize the quantitative classification of the three asymptotic regimes as follows (Krumholz et al. 2007):

$$\text{free streaming:} \quad \tau \ll 1 \tag{3.40a}$$

$$\text{diffusion:} \quad \tau \gg 1 \qquad \text{static:} \quad \beta \ll \frac{1}{\tau} \tag{3.40b}$$

$$\text{dynamic:} \quad \beta \gg \frac{1}{\tau} \tag{3.40c}$$

where $\tau(\nu_0)$ is the monochromatic optical depth as defined above. We extend this classification to the frequency-integrated optical depth.

Relative sizes of the terms

We analyse the relative sizes of the terms of the comoving-frame radiation moment equations (3.38) and (3.39), by evaluating the order of magnitude of the evolution of each term on the characteristic structural length ℓ. We have already introduced, above, the characteristic times for a photon to cross ℓ: the diffusion timescale t_d in a static diffusion regime, and the fluid-flow timescale t_f in a dynamic diffusion regime. In a free-streaming regime, the characteristic time for a photon to cross ℓ is the radiation-flow timescale $t_r \equiv \ell/c$.
One can link the three total radiation moments, E_0, $\mathbf{F}_0$, $\mathbb{P}_0$ in the three asymptotic regimes described above. One can show that (Mihalas & Mihalas 1984) in the free streaming regime:

$$\text{free streaming} \quad \begin{cases} \mathbf{F}_0 \xrightarrow[\tau \ll 1]{\beta \ll 1} c\, E_0\, \mathbf{n}_0 + \mathbf{O}(\beta) & (3.41a) \\ \mathbb{P}_0 \xrightarrow[\tau \ll 1]{\beta \ll 1} E_0\, \mathbf{n}_0 \otimes \mathbf{n}_0 + \mathbb{O}(\beta) & (3.41b) \end{cases}$$

One can also show that (Mihalas & Mihalas 1984) in the, either static of dynamic, first order equilibrium diffusion regime:

$$\text{diffusion (static or dynamic)} \quad \begin{cases} \mathbf{F}_0 = -\dfrac{c}{\chi_{0R}} \nabla \cdot \mathbb{P}_0 & (3.42a) \\ \mathbb{P}_0 = \dfrac{1}{3} E_0\, \mathbb{I} & (3.42b) \end{cases}$$

In addition, within the second-order equilibrium diffusion approximation (Mihalas & Mihalas 1984; Castor 2004), the comoving-frame radiation energy E_0 has the following orders of magnitude, in, respectively, the static diffusion regime, and the dynamic diffusion regime:

$$\text{diffusion} \quad \begin{cases} E_0 \underset{\text{diffusion}}{\overset{\text{static}}{\sim}} \dfrac{4\pi B_0}{c} \left[1 \pm \left(\dfrac{1}{\tau} \right)^2 \right] & (3.43a) \\ E_0 \underset{\text{diffusion}}{\overset{\text{dynamic}}{\sim}} \dfrac{4\pi B_0}{c} \left[1 \pm \left(\dfrac{\beta}{\tau} \right) \right] & (3.43b) \end{cases}$$

Using the results above, we can now estimate the orders of magnitude of each term of Eq. (3.38) and (3.39). We globally follow the usual approaches described in Mihalas & Klein (1982); Mihalas & Mihalas (1984); Stone et al. (1992); Krumholz et al. (2007); Skinner & Ostriker (2013). Following Krumholz et al. (2007) and Skinner & Ostriker (2013), we adopt the characteristic length ℓ in the three asymptotic regimes, for the fluid and radiation quantities. We adopt the characteristic timescale t_f for the fluid quantities. We adopt the following characteristic

timescales for the radiation quantities: t_r in the free-streaming regime, t_d in the static diffusion regime, and t_f in the dynamic diffusion regime. The spatial derivatives are characterized by $1/\ell$. The time derivatives are characterized by $1/(\text{characteristic timescale})$.

Table 3.1 and Table 3.2 display the relative scaling of each term in, respectively, Eq. (3.38) and Eq. (3.39). In each asymptotic regime, the normalization parameter is indicated in the last column. We also have sorted, in each regime, the terms according to their relative orders of magnitude, from the largest ones (rank 1), to the smallest ones (rank 3 or rank 4). The tables show that the terms with acceleration ((f) in Table 3.1, (g) and (h) in Table 3.2) are from one to three orders of magnitude smaller than the leading terms. Then, one can safely always neglect them, as already stated by Mihalas & Mihalas (1984). Moreover, the terms that account for the time derivative of the radiation momentum ((c) in Table 3.1), and of the radiation pressure ((f) in Table 3.2), are from one to two orders of magnitude smaller than the leading terms. Then, one can also safely always neglect them. In Table 3.1, the relative order of magnitude of the radiation energy source - sink term, $-\,c\,G_0^0$, cannot be estimated a priori in non-LTE (it is τ in LTE). That is why, its rank is considered to be one by default. Finally, in Table 3.2, the terms (c), (d), and (e) are from one to two orders of magnitude smaller than the leading terms. So, we can neglect them, to get a solution valid to $O(1)$.

The radiation moment equations to $O(1)$

The discussion above on the orders of magnitude suggests that, if we keep only the terms that are leading in at least one of the three asymptotic regimes, then the total non-LTE radiation moment equations are:

$$\frac{\partial E_0}{\partial t} + \nabla\cdot\mathbf{F}_0 + \nabla\cdot(E_0\,\mathbf{u}) + \mathbb{P}_0 : \nabla\,\mathbf{u} = L_0 - c\,\kappa_{0P}\,E_0\,, \tag{3.44a}$$

$$\frac{\partial}{\partial t}\left(\frac{\mathbf{F}_0}{c^2}\right) + \nabla\cdot\mathbb{P}_0 = -\frac{1}{c}\,\chi_{0R}\,\mathbf{F}_0. \tag{3.44b}$$

Note that, if we want to solve the radiation moment equations to the next order, i.e., by keeping the terms that are $O(\beta)$ relative to the leading terms, then, we should add term (c) from Table 3.1 in the radiation energy equation, and terms (c), (d), (e), and (f) from Table 3.2 in the radiation momentum equation.

Table 3.1 – Relative sizes of terms in the comoving-frame radiation energy equation (3.38) $\left(\mathrm{erg\ cm^{-3}\ s^{-1}}\right)$

Radiation energy (tag)		$\frac{\partial E_0}{\partial t}$ (a)	$\nabla \cdot \mathbf{F}_0$ (b)	$\mathbf{u} \cdot \frac{\partial}{\partial t}\left(\frac{\mathbf{F}_0}{c^2}\right)$ (c)	$\nabla \cdot (E_0\,\mathbf{u})$ (d)	$\mathbb{P}_0 : \nabla \mathbf{u}$ (e)	$2\,\mathbf{F}_0 \cdot \frac{\mathbf{a}}{c^2}$ (f)	$-c\,G_0^0$ (g)	Normalization
free streaming	$t_r \sim \frac{\ell}{c}$	1	1	β	β	β	β^2	$L_0 \frac{t_r}{E_0}(\underset{\mathrm{LTE}}{\rightarrow} \tau)$	$\times \left(\frac{E_0}{t_r}\right)$
	rank	1	1	2	2	2	3	1	
static diffusion	$t_d \sim \frac{\ell^2}{c\,\lambda_p}$	1	1	$\frac{\beta}{\tau}$	$\beta\tau$	$\beta\tau$	β^2	1	$\times \left(\frac{E_0}{t_d}\right)$
$t_d \ll t_f$	rank	1	1	3	2	2	4	1	
dynamic diffusion	$t_f \sim \frac{\ell}{u}$	1	$\frac{1}{\beta\tau}$	$\frac{\beta}{\tau}$	1	1	$\frac{\beta}{\tau}$	1	$\times \left(\frac{E_0}{t_f}\right)$
$t_f \ll t_d$	rank	1	2	3	1	1	3	1	

Table 3.2 – Relative sizes of terms in the comoving-frame radiation momentum equation (3.39) $\left(\mathrm{dyn\ cm^{-3}}\right)$

Radiation momentum		$\frac{\partial}{\partial t}\left(\frac{\mathbf{F}_0}{c^2}\right)$	$\nabla\cdot\mathbb{P}_0$	$(\mathbf{u}\cdot\nabla)\left(\frac{\mathbf{F}_0}{c^2}\right)$	$\left(\frac{\mathbf{F}_0}{c^2}\cdot\nabla\right)\mathbf{u}$	$(\nabla\cdot\mathbf{u})\left(\frac{\mathbf{F}_0}{c^2}\right)$	$\frac{\partial\mathbb{P}_0}{\partial t}\frac{\mathbf{u}}{c^2}$	$\frac{1}{c^2}\left(\mathbb{P}_0\,\mathbf{a}\right)$	$\frac{1}{c^2}\left(E_0\,\mathbf{a}\right)$	$-\mathbf{G}_0$	Normalization
(tag)		(a)	(b)	(c)	(d)	(e)	(f)	(g)	(h)	(i)	
free streaming	$t_r\sim\frac{\ell}{c}$	1	1	β	β	β	β	β^2	β^2	τ	$\times\left(\frac{F_0}{c\,\ell}\right)$
	rank	1	1	2	2	2	2	3	3	¿ 1	
static diffusion	$t_d\sim\frac{\ell^2}{c\,\lambda_p}$	$\frac{1}{\tau^2}$	1	$\frac{\beta}{\tau}$	$\frac{\beta}{\tau}$	$\frac{\beta}{\tau}$	$\frac{\beta}{\tau}$	β^2	β^2	1	$\times\left(\frac{F_0}{c\,\lambda_p}\right)$
$t_d\ll t_f$	rank	2	1	3	3	3	3	4	4	1	
dynamic diffusion	$t_f\sim\frac{\ell}{u}$	$\frac{\beta}{\tau}$	1	$\frac{\beta}{\tau}$	$\frac{\beta}{\tau}$	$\frac{\beta}{\tau}$	β^2	β^2	β^2	1	$\times\left(\frac{F_0}{c\,\lambda_p}\right)$
$t_f\ll t_d$	rank	3	1	3	3	3	2	2	2	1	

3.6.4 The flux-limited diffusion approximation

To close the system, we apply the flux-limited (FLD) approximation (Alme & Wilson 1973). The FLD approach, which has been widely used in many RHD and RMHD codes (ZEUS: Turner & Stone 2001, ORION: Krumholz et al. 2007, V2D: Swesty & Myra 2009, NIRVANA: Kley et al. 2009, RAMSES: Commerçon et al. 2011b; González et al. 2015, CASTRO: Zhang et al. 2011, 2013, PLUTO: Kolb et al. 2013; Flock et al. 2013, CRASH: van der Holst et al. 2011, FLASH: Klassen et al. 2014) consists in replacing the radiation momentum equation with a Fick's law of diffusion that links the comoving total radiation flux to the comoving total radiation energy through a radiation diffusion coefficient K, as written below:

$$\mathbf{F}_0 = -K\,\nabla E_0 \qquad \text{with} \quad K \equiv \frac{c\,\lambda}{\chi_{0R}} \tag{3.45}$$

where λ (not to be confused with the photon mean free path $\lambda_p(\nu_0)$ defined in Sect. 3.6.3) is the so-called flux-limiter, a dimensionless quantity that should be defined so that the relation between the radiation flux and the radiation energy is correct in the optically thin and optically thick asymptotic regimes. In other words, we must choose λ so that:

$$\begin{cases} \lambda \to 1/R & \text{in an optically thin medium} \\ \lambda \to 1/3 & \text{in an optically thick medium} \end{cases} \tag{3.46}$$

where the dimensionless quantity R is defined as follows:

$$R \equiv \frac{|\nabla E_0|}{\chi_{0R}\,E_0} \sim \frac{1}{\tau} \begin{cases} \xrightarrow[\text{optically thin}]{} \infty \\ \xrightarrow[\text{optically thick}]{} 0 \end{cases} \tag{3.47}$$

This way, we recover the asymptotic relations between E_0 and $\mathbf{F}_0$, in an optically thin medium, Eq. (3.41a), and in an optically thick medium, Eq. (3.42a). The flux-limiter is then defined as a function of R. Different functions are proposed in the literature. The following three ones, respectively suggested by Levermore & Pomraning (1981) (Eq. 3.48a), Minerbo (1978) (Eq. 3.48b), and Kley (1989) (Eq. 3.48c), were already implemented in PLUTO by Kolb et al. (2013):

$$\lambda(R) = \frac{1}{R}\left(\coth R - \frac{1}{R}\right) \tag{3.48a}$$

$$\lambda(R) = \begin{cases} \dfrac{2}{3+\sqrt{9+12R^2}} & 0 \leqslant R \leqslant \dfrac{3}{2} \\ \dfrac{1}{1+R+\sqrt{1+2R}} & \dfrac{3}{2} < R < \infty \end{cases} \tag{3.48b}$$

$$\lambda(R) = \begin{cases} \dfrac{2}{3+\sqrt{9+10R^2}} & 0 \leqslant R \leqslant 2 \\ \dfrac{10}{10R+9+\sqrt{180R+81}} & 2 < R < \infty \end{cases} \tag{3.48c}$$

Finally, one needs a closure relation to relate the radiation pressure to the radiation energy. The most commonly used one (e.g., by Turner & Stone 2001, Krumholz et al. 2007, Zhang et al. 2011, Zhang et al. 2013) is that provided by Levermore (1984):

$$\mathbb{P}_0 = \frac{E_0}{2}\left[(1-f)\,\mathbb{I} + (3f-1)\,\mathbf{n}_0 \otimes \mathbf{n}_0\right] \tag{3.49}$$

where f is the Eddington factor, a dimensionless quantity, related to λ and R as follows:

$$f = \lambda + \lambda^2 R^2 \quad \begin{cases} \xrightarrow[\text{optically thin}] \; 1 \\ \xrightarrow[\text{optically thick}] \; \dfrac{1}{3} \end{cases} \tag{3.50}$$

where the limits are inferred from (3.46) and (3.47). Then, we verify that (3.49) recovers the following asymptotic relations: (3.41b) in an optically thin medium, and (3.42b) in an optically thick medium.

3.7 THE NON-LTE RMHD EQUATIONS SOLVED BY PLUTO

We have implemented in a module, which is coupled to PLUTO, the radiation terms that account for a non-LTE radiation hydrodynamics (RHD) description of a flow, by expanding the LTE RHD equations (Kolb et al. 2013) to the more general non-LTE regime. Since PLUTO is a MHD code, we have actually enhanced its capabilities, so that it is now a 3D non-LTE radiation magnetohydrodynamics (RMHD) code.

We use the RHD equations within the approximations detailed previously in the text.

The full set of 3D nonrelativistic RMHD equations solved by PLUTO is based on the full MHD equations (Mignone et al. 2007, 2012), and on Equations (3.35), (3.36), (3.37), (3.44a),

and (3.45). The system is written as:

$$\frac{\partial \rho}{\partial t} + \nabla \cdot (\rho\, \mathbf{u}) = 0 \tag{3.51}$$

$$\frac{\partial}{\partial t}(\rho \mathbf{u}) + \nabla \cdot \left[\rho \mathbf{u}\mathbf{u} - \mathbf{B}\mathbf{B} + \left(p + \tfrac{1}{2} B^2\right) \mathbb{I}\right] = \rho \mathbf{g} + \nabla \cdot \mathrm{T}_{\mathrm{visc}} + \frac{1}{c}\chi_{0R}\mathbf{F}_0 \tag{3.52}$$

$$\begin{aligned}\frac{\partial}{\partial t}\left(\mathbb{E} + \tfrac{1}{2}\rho u^2 + \tfrac{1}{2}B^2\right) + \nabla \cdot \left[\left(\mathbb{E} + \tfrac{1}{2}\rho u^2 + \tfrac{1}{2}B^2 + p + \tfrac{1}{2}B^2\right)\mathbf{u} - (\mathbf{u}\cdot\mathbf{B})\,\mathbf{B}\right] = \rho \mathbf{g}\cdot\mathbf{u} \\ + \nabla \cdot [-\mathbf{F}_c + \mathrm{T}_{\mathrm{visc}}\mathbf{u} - (\eta \mathbf{J}) \times \mathbf{B}] + \frac{1}{c}\chi_{0R}\mathbf{F}_0 \cdot \mathbf{u} + c\kappa_{0P}E_0 - L_0\end{aligned} \tag{3.53}$$

$$\frac{\partial E_0}{\partial t} + \nabla \cdot \mathbf{F}_0 = L_0 - c\kappa_{0P}E_0 \tag{3.54}$$

$$\mathbf{F}_0 = -\left(\frac{c\lambda}{\chi_{0R}}\right)\nabla E_0 \tag{3.55}$$

$$\frac{\partial \mathbf{B}}{\partial t} + \nabla \cdot (\mathbf{u}\mathbf{B} - \mathbf{B}\mathbf{u}) = -\nabla \times (\eta \mathbf{J}) \tag{3.56}$$

$$p = \rho \frac{k_B T}{\mu m_H} \quad \text{(EOS)} \tag{3.57}$$

$$\mathbb{E} = \frac{p}{\gamma - 1} = \rho \frac{k_B}{(\gamma - 1)\,\mu m_H} T \quad \text{(caloric EOS)} \tag{3.58}$$

where B is the magnetic field, λ is the flux-limiter (defined in Sect. 3.6.4), k_B is the Boltzmann constant, γ is the ratio of specific heats, μ is the mean molecular weight, m_H is the standard mass of one atom of hydrogen, $\mathbf{F}_c$ is the conductive flux, $\mathrm{T}_{\mathrm{visc}}$ is the viscous tensor, η is the magnetic resistivity tensor, and $\mathbf{J} \equiv \nabla \times \mathbf{B}$ is the current density (for more information on these quantities, see Mignone et al. 2007, 2012; Orlando et al. 2008).

The opacities κ_{0P}, χ_{0R}, and the radiative losses L_0 can be provided separately. In our case, we use databases pre-calculated as functions of density and temperature in a non-LTE regime (see Sect. 3.8).

Note that an additional approximation is made in the radiation energy equation (3.54) solved by PLUTO. The terms $\nabla \cdot (E_0\, \mathbf{u})$ and $\mathbb{P}_0 : \nabla$ are missing, compared to (3.44a). They were already missing in the LTE RHD version by Kolb et al. (2013) (cf. their equation 4). Table 3.1 reveals that these two terms are leading terms only in the dynamic diffusion regime, but are of second order in the static diffusion regime and in the free streaming regime. So, at this stage, our module cannot be used in the dynamic diffusion regime. We plan to implement these two terms in a future upgraded version of our RHD module.

3.8 NON-LTE OPACITIES AND RADIATIVE POWER LOSS: THEORETICAL MODEL

Our module needs, at a given set of density and temperature (ρ, T), and for a given composition of the plasma, the following input data: the radiation emission L_0, the Planck mean opacity κ_{0P}, and the Rosseland mean opacity χ_{0R}.

The corresponding databases have been generated by Rodríguez et al. (2018) in a non-LTE regime, but also in LTE regime. Our module uses three tables, (L_0, k_{0P}, k_{0R}) as functions of (ρ, T), for a plasma with solar-like abundances, where k_{0P} and k_{0R} are $(\mathrm{cm}^2\ \mathrm{g}^{-1})$:

$$k_{0P} \equiv \frac{\kappa_{0P}}{\rho} \tag{3.59}$$

$$k_{0R} \equiv \frac{\chi_{0R}}{\rho} \tag{3.60}$$

In this section we briefly summarize the features of the theoretical model, whose details are explained in Rodríguez et al. (2018). Note that our module can read any other set of data (L_0, k_{0P}, k_{0R}) that would be provided by the user.

Plasma radiative properties depend on the plasma level populations and atomic properties. In the present work, the atomic quantities of the different chemical elements of the multicomponent plasma, such as the relativistic energy levels, wave functions, oscillator strengths and photoionization cross sections, were calculated using the FAC code (Gu 2008), in which a fully relativistic approach based on the Dirac equation is solved. The atomic calculations were carried out in the relativistic detailed configuration account (Bauche et al. 1987). The atomic configurations selected for each ion in the plasma mixture were those with energies within two times the ionization energy of the ground configuration of the ion.

The atomic level populations were obtained assuming the plasma in steady-state. This approach is valid when the characteristic time of the most relevant atomic process in the plasma is considerably shorter than the time associated to changes in the plasma density and temperature, i.e., the characteristic time of the plasma evolution. When this criterion is fulfilled, the atomic processes are fast enough to distribute the atomic level populations in the plasma before the density and temperature of the plasma change. This approach is commonly used to obtain the atomic level populations in the plasma needed in the calculation of radiative properties databases for radiation-hydrodynamics simulations. In the steady-state approximation, the population density of the atomic level i of the ion with charge state ζ, denoted as $N_{\zeta i}$ is obtained by solving the set of rate equations implemented in a collisional-radiative steady-state (CRSS) model, given by

$$\sum_{\zeta' j} N_{\zeta' j}(\mathbf{r}, t) R^{+}_{\zeta' j \to \zeta i} - \sum_{\zeta' j} N_{\zeta i}(\mathbf{r}, t) R^{-}_{\zeta i \to \zeta' j} = 0 \tag{3.61}$$

Two complementary equations have to be satisfied together with Eq. (3.61). First, the requirement that the sum of all the partial densities equals the total ion density and, second, the charge neutrality condition in the plasma. In Eq. (3.61), $R^{+}_{\zeta' j \to \zeta i}$ and $R^{-}_{\zeta' j \to \zeta i}$ take into account all the atomic processes which contribute to populate and depopulate the atomic configuration ζ_i, respectively. The atomic processes included in the CRSS model were collisional ionization (Lotz 1968) and three-body recombination, spontaneous decay (Gu 2008), collisional excitation (van Regemorter 1962) and deexcitation, radiative recombination (Kramers 1923), autoionization and electron capture (Griem 1997). The rates of the inverse processes were obtained through the detailed balance principle. It is important to precise that in the computation of the atomic level populations used for the present work, the plasma was assumed as optically thin: the contribution of the radiative absorption processes like for instance photoionization and bound-bound transitions, are neglected in the calculation. The effect of the plasma environment on the population of the atomic levels was modeled through the depression of the ionization potential or continuum lowering, which can reduce the number of bound states available. The formulation developed by Stewart & Pyatt (1966) was applied. In the present CRSS model, the ions were considered to be at rest. On the other hand, in the calculation of the rates of the atomic processes, a Maxwell-Boltzmann distribution for the free electrons was assumed. For electron densities between 10^{11} and 10^{14} cm^{-3} and electron temperatures lower than 200 eV, the electron mean free paths range between 3.33×10^{5} and 25.8 cm (Rodríguez et al. 2018). This property provides an estimation of the average volume needed for the free electrons to thermalize. For the range of plasma conditions analyzed in this work, the Fermi-Dirac distribution is not necessary. The CRSS model described is implemented in MIXKIP code (Espinosa et al. 2017).

As said before, in this work a multi-component plasma was simulated. The chemical elements considered in the mixture were H, He, C, N, O, Ne, Na, Mg, Al, Si, S, Ar, Ca and Fe, and the solar-like abundances provided by Asplund et al. (2009) were used. For a given electron density and temperature, the CRSS model is solved for each element without considering any atomic processes that connect different chemical elements. However, they were coupled through the common pool of free electrons since the plasma level populations of each chemical element have to be consistent with the common electron density. This fact ensures the plasma neutrality (Klapisch & Busquet 2013).

Once the atomic data and level populations were obtained, the monochromatic absorption coefficient and emissivity of each chemical element m, $\kappa_m(\nu)$ and $j_m(\nu)$, respectively, with ν the photon frequency, were calculated using the RAPCAL code (Rodríguez et al. 2008, 2010). Both coefficients include the bound-bound, bound-free and free-free contributions. The radiative transition rates were calculated in the electric dipole approximation using the FAC code. The oscillator strengths included a correction to take into account configuration interaction effects due to the mix between relativistic configurations that belong to the same non-relativistic one. The photoionization cross sections were calculated in the distorted wave approach. Complete redistribution hypothesis was assumed for the line profile which

included natural, Doppler, electron-impact (Dimitrijevic & Konjevic 1987) and UTA broadenings (Bauche et al. 1987). The line-shape function was applied with the Voigt profile that incorporated all these broadenings. For the free-free contributions, the Kramers semi-classical expression for the inverse bremsstrahlung cross section was used (Rose 1992). In order to determine the opacity, $k(\nu)$, from the absorption coefficient, the scattering of photons was also taken into account, and, in RAPCAL, this was approximated using the Thomson scattering cross section (Rutten 1995). The monochromatic opacities and emissivities of the mixture were obtained from the weighted contributions of the different chemical elements

$$k(\nu) = \frac{1}{\rho}\sum_m X_m\,\kappa_m(\nu) \tag{3.62a}$$

$$j(\nu) = \sum_m X_m\,j_m(\nu) \tag{3.62b}$$

where ρ is the mass density of the mixture. From the monochromatic opacities of the mixture, the Planck k_{0P} and Rosseland k_{0R} mean opacities were calculated, as well as the radiative power loss, or radiation emission, L_0, from the monochromatic emissivity. Figure 3.2 portrays maps of L_0, k_{0P}, and k_{0R}, vs. free electron density (cm^{-3}) and temperature (K) in logarithmic scale, in a non-LTE regime, and in LTE regime. Both MIXKIP and RAPCAL codes have been successfully tested with experimental results and numerical simulations for plasmas of single elements included in the mixture analyzed in this work (Espinosa et al. 2017; Rodríguez et al. 2008, 2010), both in LTE and non-LTE, and for the plasma mixture in LTE simulations (Rodríguez et al. 2018). A more detailed explanation of both codes can be found in Rodríguez et al. (2018).

3.9 IMPLEMENTATION OF THE RADIATION TERMS

We explain, here, how the radiative terms of the physical equations are implemented in the code. We have followed and upgraded to the non-LTE case the techniques described for the LTE regime in Kolb et al. (2013) (see also Commerçon et al. 2011b, van der Holst et al. 2011, Zhang et al. 2011, and Zhang et al. 2013). We use an operator-split method. As detailed in this section, advancing the variables during a time step is made in two substeps, an explicit one (Sect. 3.9.2), and an implicit one (Sect. 3.9.3). The latter involves the radiation emission L_0, which is an analytical function of temperature in LTE ($L_0 = k_{0P}\,\rho\,c\,a_R\,T^4$), but has no analytical expression in non-LTE, and is stored in databases (see Sect. 3.8). Our original contribution, with respect to the usual LTE implementations, consists in handling this non-analytical radiation emission term in the treatment of the implicit scheme, as explained below in Sect. 3.9.3.

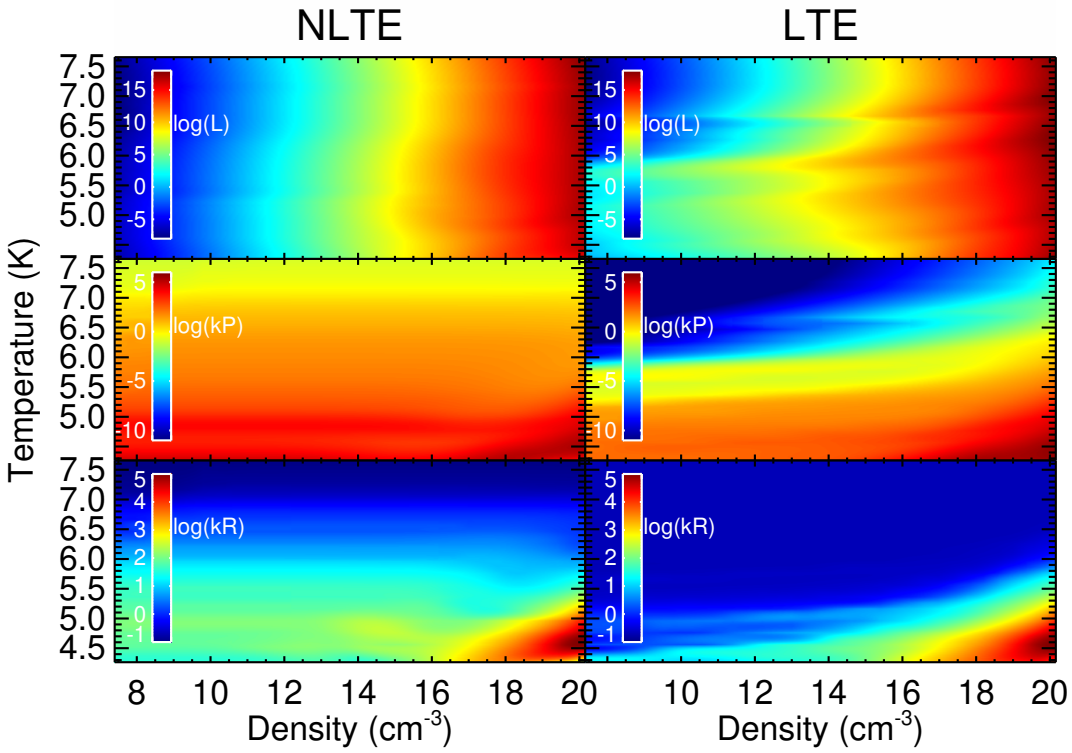

Figure 3.2 – Total radiation emission (erg cm^{-3} s^{-1}) (top panels), Planck opacities (cm^2 g^{-1}) (mid panels), and Rosseland opacities (cm^2 g^{-1}) (bottom panels), in a non-LTE regime (left), and in LTE regime (right).

3.9.1 REFORMULATION OF THE EQUATIONS

For the sake of simplicity, we remove from the full system solved by PLUTO, (3.51) - (3.58), the terms depending on the magnetic field, and rewrite it in a simplified version, for an inviscid fluid without heat-conduction, but subject to external gravity (even though the following discussion can be applied to the full RMHD system):

$$\frac{\partial \rho}{\partial t} + \nabla \cdot (\rho \mathbf{u}) = 0 \tag{3.63}$$

$$\frac{\partial}{\partial t}(\rho \mathbf{u}) + \nabla \cdot (\rho \mathbf{u}\mathbf{u} + p\,\mathbb{I}) = \rho \mathbf{g} + \frac{\rho k_R}{c}\mathbf{F} \tag{3.64}$$

$$\frac{\partial}{\partial t}\left(\mathbb{E} + \tfrac{1}{2}\rho u^2\right) + \nabla \cdot \left[\left(\mathbb{E} + \tfrac{1}{2}\rho u^2 + p\right)\mathbf{u}\right] = \rho \mathbf{g}\cdot\mathbf{u} + \frac{\rho k_R}{c}\mathbf{F}\cdot\mathbf{u} + k_P\,\rho\, c\, E - L \tag{3.65}$$

$$\frac{\partial E}{\partial t} + \nabla \cdot \mathbf{F} = L - k_P\,\rho\, c\, E \tag{3.66}$$

$$\mathbf{F} = -\frac{c\,\lambda}{k_R\,\rho}\nabla E \tag{3.67}$$

$$p = \rho\,\frac{k_B\,T}{\mu\, m_H} \tag{3.68}$$

$$\mathbb{E} = \frac{p}{\gamma - 1} = \rho\,\frac{k_B}{(\gamma-1)\,\mu\, m_H}\,T \tag{3.69}$$

where we have omitted, for economy of notation, the subscript 0 in the radiation quantities. The above system contains 11 unknowns: six principal variables $(\rho, \mathbf{u}, p, E)$ that are determined by solving the six equations (3.63), (3.64), (3.65), and (3.66), and five variables $(T, \mathbb{E}, \mathbf{F})$ that can be inferred from the six principal ones from the FLD relation (3.67), the EOS (3.68), and the caloric EOS (3.69).

At each time step $\Delta t^n = t^{n+1} - t^n$, determined by the CFL condition (Mignone et al. 2007), we advance the gas and radiation variables from t^n to t^{n+1}, by solving the above system in two consecutive substeps, as described below. We denote as $(\rho^n, \mathbf{u}^n, p^n, E^n)$ and $(T^n, \mathbb{E}^n, \mathbf{F}^n)$ the values of the variables at time t^n, and $(\rho^{n+1}, \mathbf{u}^{n+1}, p^{n+1}, E^{n+1})$ and $\left(T^{n+1}, \mathbb{E}^{n+1}, \mathbf{F}^{n+1}\right)$ their values at time t^{n+1}, *after* the *two* substeps are completed.

3.9.2 SUBSTEP 1: EXPLICIT HYDRODYNAMICS

In this first substep, PLUTO solves the hyperbolic subsystem made of Equations (3.63), (3.64), (3.65), but without the radiation source (also known as source-sink) terms $k_P\,\rho\, c\, E - L$ in the gas energy equation (3.65). The system to be solved is:

$$\frac{\partial \rho}{\partial t} + \nabla \cdot (\rho \mathbf{u}) = 0 \tag{3.70}$$

$$\frac{\partial}{\partial t}(\rho \mathbf{u}) + \nabla \cdot (\rho \mathbf{u}\mathbf{u} + p\mathbb{I}) = \rho \mathbf{g} - \lambda \nabla E \tag{3.71}$$

$$\frac{\partial}{\partial t}\left(\frac{p}{\gamma - 1} + \frac{1}{2}\rho u^2\right) + \nabla \cdot \left[\left(\frac{p}{\gamma - 1} + \frac{1}{2}\rho u^2 + p\right)\mathbf{u}\right] = \rho \mathbf{g} \cdot \mathbf{u} - \lambda \mathbf{u} \cdot \nabla E \tag{3.72}$$

where we have introduced (3.67), (3.69) in (3.64), (3.65). A Godunov type algorithm is applied, with several possibilities of Riemann solvers (see Mignone et al. 2007 for details).

We use a $*$ superscript to denote the quantities obtained at the completion of this substep. Some of these quantities have intermediate results that will be updated in the next substep (Sect. 3.9.3). Starting from $(\rho^n, \mathbf{u}^n, p^n)$, PLUTO determines $(\rho^*, \mathbf{u}^*, p^*)$, the terms involving the radiation energy density E^n being in the source part of the solved system, and, therefore, not updated. The corresponding intermediate temperature is obtained from the EOS (3.68):

$$T^* = \frac{p^*}{\rho^* \frac{k_B}{\mu\, m_H}} \tag{3.73}$$

3.9.3 Substep 2: implicit radiation diffusion and source terms

In this second substep, we determine, at time t^{n+1}, the radiation energy density E^{n+1}, and the gas temperature T^{n+1}, by solving the radiation energy equation (3.66), and the gas energy equation (3.65) without any velocity term (we couple the gas internal energy density evolution rate with the radiation source terms). The system to be solved in non-LTE is:

$$\frac{\partial E}{\partial t} - \nabla \cdot \left(\frac{c\lambda}{\rho k_R} \nabla E\right) = L - k_P \rho c E \tag{3.74}$$

$$\frac{\partial \mathbb{E}}{\partial t} = k_P \rho c E - L \tag{3.75}$$

where the gas energy density $\mathbb{E}$ is directly related to the gas temperature through the caloric equation of state (3.69).

Since timescales for radiation are much smaller than timescales for hydrodynamics, time steps that would be inferred from the CFL condition would lead, if applied to radiation, to impracticable computations. Consequently, we use an implicit scheme for solving the system (3.74) - (3.75), with the time step Δt^n provided by the explicit hydrodynamics substep 1.

Starting from (E^n, ρ^*, T^*), we obtain, at the completion of this substep, (E^{n+1}, T^{n+1}).

The time discretization of (3.74) and (3.75) is made according to the following implicit scheme:

$$\frac{E^{n+1}-E^{n}}{\Delta t^{n}} - \nabla\cdot\left(K^{*}\nabla E^{n+1}\right) = L^{n+1} - k_{P}^{*}\,\rho^{*}cE^{n+1} \tag{3.76}$$

$$\rho^{*}c_{V}\frac{T^{n+1}-T^{*}}{\Delta t^{n}} = k_{P}^{*}\rho^{*}cE^{n+1} - L^{n+1} \tag{3.77}$$

where, while relating $\mathbb{E}$ to ρ and T with (3.69), we assume that the mass density ρ is not modified by this implicit substep (following Commerçon et al. 2011b, Zhang et al. 2011, Zhang et al. 2013, and Kolb et al. 2013), and where

$$c_{V} = \frac{k_{B}}{(\gamma-1)\,\mu m_{H}} \tag{3.78}$$

$$L^{n+1} = L\left(\rho^{n+1}, T^{n+1}\right) \tag{3.79}$$

$$k_{P}^{*} = k_{P}\left(\rho^{*}, T^{*}\right) \tag{3.80}$$

$$k_{R}^{*} = k_{R}\left(\rho^{*}, T^{*}\right) \tag{3.81}$$

$$K^{*} = \frac{c\lambda(R^{*})}{k_{R}^{*}\rho^{*}} \quad \text{with} \quad R^{*} = \frac{|\nabla E^{n}|}{\rho^{*}k_{R}^{*}E^{n}} \tag{3.82}$$

The radiation diffusion coefficient K, the flux-limiter λ, and the dimensionless quantity R have been defined in Sect. 3.6.4. The space discretization of (3.76) is obtained from a finite volume method (now adapted to non-LTE regimes):

$$\frac{E_{ijk}^{n+1}-E_{ijk}^{n}}{\Delta t^{n}} - h_{ijk}(E^{n+1}, K^{*}) = L_{ijk}^{n+1} - k_{P\,ijk}^{*}\rho^{*}cE_{ijk}^{n+1} \tag{3.83}$$

where

$$h_{ijk}(E^{n+1}, K^{*}) \equiv \nabla\cdot\left(K^{*}\nabla E^{n+1}\right) \tag{3.84}$$

represents the discretized radiation diffusion term, a linear function of E^{n+1} given by Equation (14) of Kolb et al. (2013), and where the indices i, j, k identify the positions of the cell centers in the 3D computational grid.

The radiation emission at time t^{n+1}, L^{n+1} (Eq. 3.79), is determined from a 1st order Taylor expansion, starting from the state (ρ^{*}, T^{*}) obtained from substep 1:

$$L^{n+1} = L^{*} + \left(\frac{\partial L}{\partial T}\right)^{*}\left(T^{n+1}-T^{*}\right) + \cancel{\left(\frac{\partial L}{\partial \rho}\right)^{*}\left(\rho^{n+1}-\rho^{*}\right)} \tag{3.85}$$

with

$$L^{*} = L\left(\rho^{*}, T^{*}\right) \tag{3.86}$$

$$\left(\frac{\partial L}{\partial T}\right)^{*} = \left(\frac{\partial L}{\partial T}\right)\left(\rho^{*}, T^{*}\right); \quad \left(\frac{\partial L}{\partial \rho}\right)^{*} = \left(\frac{\partial L}{\partial \rho}\right)\left(\rho^{*}, T^{*}\right) \tag{3.87}$$

where we have struck out the term in mass density. This is because we have assumed that the mass density ρ is not modified by this substep 2. Moreover, the dependence of the radiation emission L on T is much higher than that on ρ (see Rodríguez et al. 2018, and references therein for more details).

Using (3.85) inside (3.77) and (3.83), we obtain, after some algebra (we removed the subscript i, j, k from each term for simplicity):

$$\frac{E^{n+1} - E^n}{\Delta t^n} = h(E^{n+1}, K^*) + \frac{L^* - k_P^* \, \rho^* c \, E^{n+1}}{1 + \left(\frac{\Delta t^n}{\rho^* \, c_v}\right) \left(\frac{\partial L}{\partial T}\right)^*} \tag{3.88}$$

$$T^{n+1} = T^n + \frac{\left(\frac{\Delta t^n}{\rho^* \, c_v}\right)}{1 + \left(\frac{\Delta t^n}{\rho^* \, c_v}\right) \left(\frac{\partial L}{\partial T}\right)^*} \left(k_P^* \, \rho^* \, c \, E^{n+1} - L^*\right) \tag{3.89}$$

Eq. (3.88) represents a linear system whose unknown is the radiation energy density E_{ijk}^{n+1}, at time t^{n+1}, and at all positions (i, j, k) in the computational domain. The system is solved using the PETSc solver, which is already implemented in the original version of the module; also, the boundary conditions for the radiation energy density can be periodic, symmetric, reflective, or with fixed values.

Once E^{n+1} is determined, the calculation of the temperature T^{n+1} is straightforward by simply applying formula (3.89). Then, using the approximation $\rho^{n+1} = \rho^*$, we update the Rosseland opacity k_R^{n+1}, and then the flux-limiter $\lambda(R^{n+1})$, therefore the radiation contribution to the right-hand side of Eq. (3.71) and (3.72). We also immediately obtain the pressure p^{n+1} from the EOS (3.68):

$$p^{n+1} = \rho^{n+1} \frac{k_B}{\mu \, m_H} T^{n+1} \tag{3.90}$$

The velocity $\mathbf{u}$ is not involved in the equations solved by this substep 2. Then, $\mathbf{u}^{n+1} = \mathbf{u}^*$. Finally, from the above quantities, we can infer the gas energy $\mathbb{E}^{n+1}$ by applying (3.69), and the radiation flux $\mathbf{F}^{n+1}$ by applying (3.67).

3.10 Tests

To validate our implementation of the non LTE equations in the radiation module in PLUTO, we simulated some test cases, and compared our solutions either to analytical, or semi-analytical results, when they exist, or, when appropriate, to the LTE version of the code. To our knowledge, all the test cases present in the literature assume the LTE regime. To have a direct comparison with those tests, we always used our non-LTE discretization scheme (cf. Sect. 3.9.3), but imposed a radiation emission (or radiative losses) L to be equal to the LTE emission ($L = k_P \, \rho \, c \, a_R \, T^4$). Such tests are described below in Sect. 3.10.1 and Sect. 3.10.2.

The tests are one-dimensional problems. Even though PLUTO works in one, two or three dimensions, the radiation module was developed only in 3D. For this reason, to model the test cases we used quasi-one-dimensional domains, which are cuboids with a length much longer than the width or the height. The tests were made only in Cartesian grid. Since, we did not change the geometrical terms in Eq. (3.88), we did not need to check the results using different grids.

To compare the results with Kolb et al. (2013), we used the solver based on the PETSc library for all test cases, with the GMRES iteration scheme and a block-Jacobi (bjacobi) preconditioner.

3.10.1 RADIATION MATTER COUPLING

Our objective is to test the correctness of the implementation of Equation (3.75), which couples the evolution of the matter (or gas) internal energy $\mathbb{E}$ with the radiation source terms $k_P\,\rho\,c\,E - L$. This equation is solved with an implicit method, in substep 2 of the operator-split scheme (see Sect. 3.9.3). In particular, this test will enable us to check our linearization procedure of the radiation emission L (Eq. 3.85), wich results in the expression of the temperature T^{n+1} versus T^n (Eq. 3.89). Such a test was first proposed by Turner & Stone (2001).

We want to freeze the evolution of any other quantity but the temperature (and, therefore, the gas internal energy). To do so, first, we build our test model as a static and uniform fluid that is initially out of radiative equilibrium, and we suppress external gravity. Second, we assume the radiation energy E to be large enough compared to the gas internal energy, so that, during the energy exchange between matter and radiation throughout the evolution process, E can be considered as a constant quantity. In this respect, the radiation flux, which is related to the gradient of radiation energy through the FLD relation (3.45), is negligible, and the continuity, matter momentum, and radiation energy equations (3.63, 3.64, 3.66) become irrelevant. The only remaining relevant equation to be solved is the matter energy equation (3.65), but in the form (3.75).

Even though we use our non-LTE discretization scheme with the radiation emission (or radiative losses) quantity L in the equations (Sect. 3.9.3), we set L to be equal to the LTE emission ($L = k_P\,\rho\,c\,a_R\,T^4$). This way, Eq. (3.75) can be recast as the following ordinary differential equation:

$$\frac{d\mathbb{E}}{dt} = A\left[1 - \left(\frac{\mathbb{E}}{\mathbb{E}_f}\right)^4\right] \tag{3.91}$$

with the two following constants:

$$A = k_P\,\rho\,c\,E \tag{3.92}$$

$$\mathbb{E}_f = \frac{\rho\,k_B}{(\gamma-1)\,\mu\,m_H\,a_R^{1/4}}\,E^{1/4} \tag{3.93}$$

where $\mathbb{E}_f$ is the gas internal energy in the final radiative equilibrium state.

Setup

For this test, we set the density $\rho = 10^{-7}$ g cm^{-3}, the radiation energy density $E = 10^{10}$ erg cm^{-3}, the Planck[1] mean opacity $\rho\, k_P = 4 \times 10^{-8}$ cm^{-1}, the mean molecular weight $\mu = 0.6$, and the ratio of specific heats $\gamma = 5/3$. The domain consists of a cuboid that has a length much larger than the other two dimensions. In particular, the cuboid has a width and a height of 3 cm, and a length of 100 cm. The grid consists of $3 \times 3 \times 100$ points. All the boundaries are periodic. For this test the hydrodynamic solver is turned off.

The simulation starts at $t = 0$ s with an initial time step of $\delta t = 10^{-20}$ s. After each step, the time step increases by 0.1%. The test is performed using 3 different initial gas internal energy densities $\mathbb{E}_0 = (6.4 \times 10^3;\ 6.4 \times 10^7;\ 6.4 \times 10^8)$ erg cm^{-3}.

Results

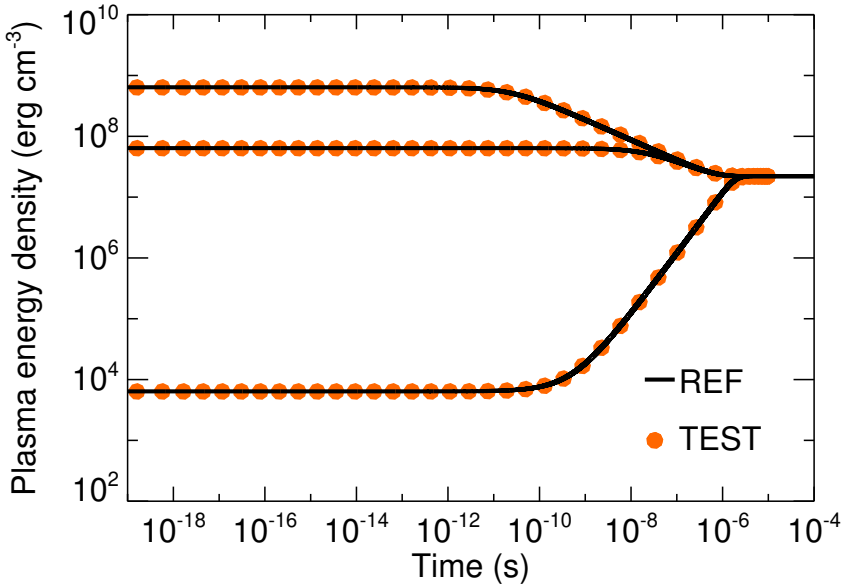

Figure 3.3 – Coupling test with three different initial gas internal energy densities. The black line represents the reference solution, the orange dots are the results obtained with the radiation module.

Fig. 3.3 shows the comparison between the solution found with our model (red dots) and the semi-analytical reference one (black line) obtained by solving (3.91) with a fourth order Runge-Kutta scheme (alternatively, a full analytical solution is provided by Swesty & Myra

[1]The choice of the Rosseland mean opacity is irrelevant since it is associated to the radiation flux that is negligible in our test; however, for computational convenience, we also adopted $\rho\, k_R = 4 \times 10^{-8}$ cm^{-1}.

2009), for the three different initial energy radiation densities $\mathbb{E}_0$. The agreement between the two solutions is excellent for all the three cases.

3.10.2 RADIATIVE SHOCKS

We test our implementation of the full set of non-LTE radiation hydrodynamics equations in PLUTO (3.63-3.69) (without external gravity), by assessing the ability of the code to reproduce the structure of radiative shock. We simulate a simple shock case in a quasi-one-dimensional domain; this test follows from Ensman (1994). It is possible to compare some characteristic quantities derived from the test, with analytical estimates (Mihalas & Mihalas 1984). We compare our results with the original version of the code (Kolb et al. 2013) and with analytical or semi-analytical solutions when available.

Setup

For this test, we simulate an initially uniform fluid with density $\rho = 7.78 \times 10^{-10}$ g cm^{-3}, and temperature $T = 10$ K, moving with velocity u along z-axis. We set the ratio of specific heats $\gamma = 7/5$, and the mean molecular weight $\mu = 1$, in analogy to Ensman (1994). We impose a constant opacity $k_R \times \rho = k_P \times \rho = 3.1 \times 10^{-10}$ cm^{-1}, and the initial radiation energy density is set by the equation $E = a_R T^4$. As in the previous test case (Sect. 3.10.1), we impose the radiative losses $L = k_P \rho c a_R T^4$ (LTE radiation emission), while using our non-LTE discretization scheme with L in the equations.

The computational domain has a width and a height of 3.418×10^7 cm, and a length (z-axis) of 7×10^{10} cm. Along with Kolb et al. (2013), we have chosen a grid composed of $4 \times 4 \times 2048$ cells, the Minerbo flux-limiter (Eq. 3.48b in Sect. 3.6.4), a Lax-Friedrichs scheme, 0.4 as CFL (Courant-Friedrichs-Lewy) value, and a relative tolerance $\epsilon = 10^{-5}$ for the matrix solver. The lateral boundaries are periodic for both hydrodynamic and radiation quantities. In the direction of the fluid flow (z-axis), we use a reflective boundary at the bottom of the domain ($z = 0$), to generate the shock, and a zero-gradient condition at the top ($z = z_{max} = 7 \times 10^{10}$ cm).

Moving from z_{max} to $z = 0$, the fluid impacts onto the reflective boundary, which generates a shock that propagates back into the fluid. The fluid velocity is calculated with respect to the computational domain, which is the physical frame of reference. The shock can be subcritical (low velocity) or supercritical (large velocity) (Mihalas & Mihalas 1984). We simulate both cases: we set $u = 6 \times 10^5$ cm s^{-1} to obtain a subcritical shock, and a higher velocity $u = 20 \times 10^5$ cm s^{-1} to obtain a supercritical shock.

Results

In order to compare our results with those obtained by Ensman (1994) or Kolb et al. (2013), we introduce the quantity $s = z - u\,t$. Fig. 3.4 shows the gas temperature (red) and the radiation temperature (blue), $T_{rad} = (E/a_R)^{1/4}$, versus s for the subcritical shock (top panel) and the

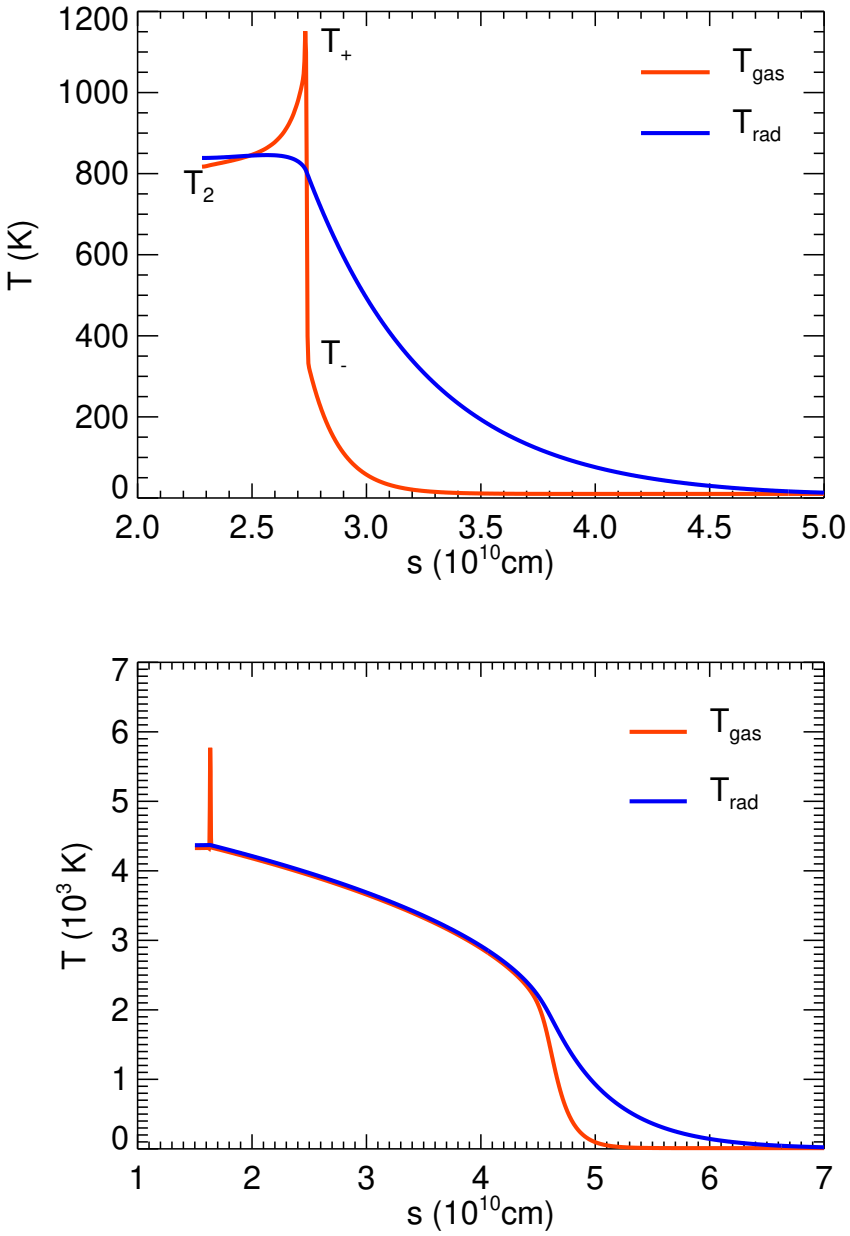

Figure 3.4 – Gas temperature (red) and radiation temperature (blue) versus $s = z - u\,t$ for the sub (top panel) and supercritical (bottom panel) shocks. The subcritical shock is shown at time $t = 3.8 \times 10^4$ s and the supercritical shock at $t = 7.5 \times 10^3$ s.

supercritical shock (bottom panel). In the supercritical shock the temperature after and before the shock are equal, as expected.

In the case of a subcritical shock, some characteristic gas temperatures can be estimated analytically (Mihalas & Mihalas 1984): T_-, the temperature immediately ahead of the shock front; T_+, the temperature immediately behind the shock front (Zel'dovich spike: Zel'dovich & Raizer 1967); T_2, the final equilibrium post-shock temperature, reached after radiative cooling. We have:

$$T_2 \approx \frac{2(\gamma-1)\,u^2}{R_G\,(\gamma+1)^2} \tag{3.94a}$$

$$T_- \approx \frac{\gamma-1}{\rho\,u\,R_G}\frac{2\,\sigma_{SB}\,T_2^4}{\sqrt{3}} \tag{3.94b}$$

$$T_+ \approx T_2 + \frac{3-\gamma}{\gamma+1}\,T_- \tag{3.94c}$$

where $R_G = k_B/\mu m_H$ is the perfect gas constant, σ_{SB} is the Stefan-Boltzmann constant, and u is the velocity of the shock relative to the upstream fluid.

Table 3.3 shows the comparison between our numerical solution, the analytical estimate, and the solution reported by Kolb et al. (2013). Our numerical solution agrees very well with the original version of the code. The relative deviation with respect to the analytical estimate is no larger than 7%. Moreover, the position and the shape of the shocks are very well reproduced. We can conclude that our modifications in the radiation module have maintained the accuracy of the code.

Table 3.3 – Comparisons of the characteristic temperatures of a subcritical shock, T_2, T_-, T_+ (Eq. 3.94a, b, c), obtained from analytical estimates, from our non-LTE code, and from the LTE initial code by Kolb et al. (2013). The last column shows the relative deviation between our numerical solution and the analytical estimate.

	Analytical estimate	Our numerical solution	Kolb et al. (2013)	Deviation
T_2	$\approx$ 865 K	817 K	816.6 K	$\approx$ 5%
T_-	$\approx$ 315 K	332 K	331.9 K	$\approx$ 5%
T_+	$\approx$ 1075 K	1151 K	1147.1 K	$\approx$ 7%

3.11 LTE vs non-LTE radiative shocks

The purpose of this section is to show the crucial importance of considering the appropriate regime (LTE vs non-LTE) for given physical conditions, in order to correctly model the structure and dynamics of a radiating fluid. This is because opacities and radiation emissions can

differ by several orders of magnitudes between both regimes, as exemplified by Fig. 3.2. Such deviations can have a major impact on the momentum and energy exchanges between matter and radiation, and, therefore, on the structure of the flow.

We modify the shock test from Ensman (1994), described in Sect. 3.10.2, to have physical conditions quite similar to those in accretion shocks in young stars (Sacco et al. 2008; Colombo et al. 2019b). As in the two test cases, we use the non-LTE discretization scheme with the radiation emission (or radiative losses) quantity L in the equations (Sect. 3.9.3). In one case, referred to as the "non-LTE case", we use the non-LTE radiative database (calculated by Rodríguez et al. 2018, see also Sect. 3.8), and let the system evolve following the flow conditions, for which, at a given time and position, either non-LTE or LTE regime prevails and is self-consistently taken into account by the database. In the other case, referred to as the "LTE case", we use the LTE database (still calculated by Rodríguez et al. 2018), and, therefore, force the LTE regime, no matter the physical conditions.

3.11.1 Setup

We simulate a uniform fluid with initial density $n = 10^{12}$ cm^{-3}, and temperature $T = 2 \times 10^4$ K, moving with velocity $u = 5 \times 10^7$ cm^{-1} along z-axis. We set $\gamma = 7/5$ and $\mu \approx 1.29$, i.e., assume solar abundances. Note that here, unlike the preceding test cases, we do not impose a constant value for k_P, k_R and L, but we use our radiative databases. The initial radiation energy E is chosen in order to start with a fluid in radiative equilibrium.

The computational domain describes a box of length 10^8 cm in the non-LTE case, and 10^7 cm in the LTE case, and of equal width and height, 3.418×10^7 cm in both cases. The grid is composed of $3 \times 3 \times 1024$ cells.

We adopt the Minerbo flux-limiter, and boundary conditions identical to those in the shock tests (Sect. 3.10.2). For the CFL condition, we use 0.01. For the matrix solver we set a relative tolerance $\epsilon = 10^{-4}$.

3.11.2 Results

The fluid impacts onto the reflective boundary, which generates a shock that propagates back into the fluid. The shock heats up the material forming a post-shock region. Fig. 3.5 shows the profiles of temperature, radiative gains ($G = k_P \rho c E$), which represent the energy gained by the fluid after absorbing radiation, and radiative losses (L) after 6 s of evolution.

The two cases present several differences while we follow their evolutions. This is related to the different regimes taken into account. In the LTE case (Fig.3.5, top panel), the shock reaches a maximum temperature of $\sim 5 \times 10^4$ K (dashed line curve). At this peak, the radiative losses (blue curve: $L \sim 5 \times 10^6$ erg cm^{-3} s^{-1}) are higher than the radiative gains (red curve: $G \sim 5 \times 10^5$ erg cm^{-3} s^{-1}). As a consequence, the material rapidly cools down until radiative equilibrium ($G = L$), and the post-shock region remains relatively cold at $\sim 2 \times 10^4$ K, close to the initial temperature.

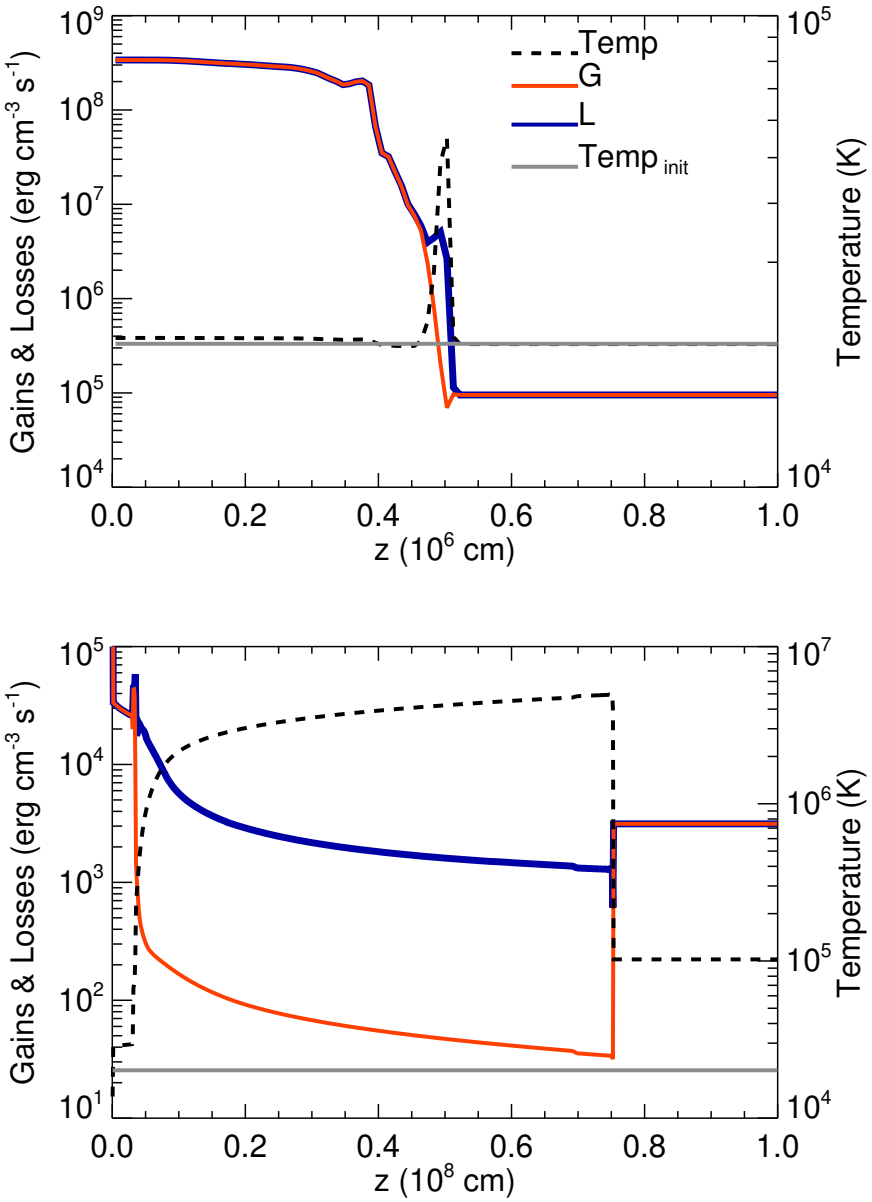

Figure 3.5 – Gas temperature (black dashed line), radiative gains G (red line) and radiative losses L (blue line) versus z for the LTE (top panel) and non-LTE (bottom panel) shock cases. Both cases are shown after 6 s of evolution. In each plot the grey solid line represents the initial temperature in the domain.

Even though the radiative losses are extremely high compared to the non-LTE case (see below, the last paragraph of this section), there is no precursor region. We can invoke two reasons for this: first, the region that emits is quite small, so the radiation energy emitted per unit time is not enough to heat up the unshocked plasma; second, according to Fig.3.2 (mid-right panel), the Planck opacity, k_P, in LTE regime is smaller by several order of magnitudes compared to that in the non-LTE case. Therefore, matter absorbs far less radiation in LTE than in non-LTE (a reminder: the gain of radiation energy by matter is $G = k_P \rho c E$).

In the non-LTE regime (Fig.3.5, bottom panel), the radiative losses are, in the shocked region, smaller by around three orders of magnitude compared to those in the LTE regime: $L_{LTE} \sim 5 \times 10^6$ erg cm^{-3} s^{-1} (see above), $L_{NLTE} \sim 10^3 - 10^4$ erg cm^{-3} s^{-1}. In this case, the shock heats the material up $T \sim 5 \times 10^6$ K, and generates a hot post-shock region. Since the radiative losses are smaller than in the LTE case, the shock-heated material needs more time to cool down, and forms a hot slab. After 6 s, the radiative losses trigger the thermal instabilities at the base of the post-shock: the material rapidly loses thermal energy through radiation emission. This drop in temperature produces enough radiation energy to heat up the unshocked plasma, thereby generating a precursor region with a temperature of $T \sim 10^5$ K (dashed line curve on the right in Fig.3.5).

3.12 Conclusions

Including the effects of radiation in HD and MHD models is a mandatory task to fully describe many astrophysical systems. Several codes fulfill this request, but none of them consider the more general non-LTE regime.

Here, we have presented our extended version of the LTE radiation module developed by Kolb et al. (2013) and implemented in the PLUTO code. The upgraded module is now able to handle non-LTE regimes (including, self-consistently, the particular case of LTE regime, depending on the physical plasma conditions). We use an operator-split method. The system is solved in two substeps, an explicit one for the hyperbolic subsystem, and an implicit one for the subsystem that involves radiation diffusion and radiation source terms. It is this second subsystem that we have upgraded so that it can now handle non-LTE conditions.

Starting from the general frequency-integrated comoving-frame radiation hydrodynamics equations, we have reviewed all the assumptions and approximations that have led to the equations that are actually coded in PLUTO. In particular, we use the flux-limited diffusion approximation. Also, our implementation is valid for plasma in conditions ranging from free streaming regime to static diffusion regime. It cannot describe the dynamic diffusion regime: to do so, we have to include the two advection terms in the radiation energy equation. Moreover, the multigroup implementation in non-LTE can be a further improvement of our module. These possible developments will be the subject of future works.

The module needs, as input data versus density and temperature, the following radiative quantities: the radiation emission, the Planck mean opacity, and the Rosseland mean opacity.

Our module currently uses non-LTE databases generated for a plasma with solar-like abundances. But the user may provide any other set of databases that would be more appropriate to the problem to be investigated.

We have tested the new implementation of the non-LTE equations, but in LTE conditions, and have compared our results with semi-analytical solutions, and with the results given by the previous version of the code. These tests have established the validity of our implementation.

We also have demonstrated, through the comparison of the structure of a radiative shock, in LTE and in non-LTE regimes, the importance of considering the appropriate regime in order to correctly describe the dynamics of a radiating fluid.

We have already successfully applied this new upgraded version of PLUTO to demonstrate the existence of a radiative precursor in the accreting stream onto the surface of a classical T Tauri Star (Colombo et al. 2019b).

The radiation module has been implemented in version 4.0 of PLUTO. The code is available, under request, to the scientific community.

CHAPTER 4

Effects of radiation on the impact region of an accretion stream onto a classical T Tauri star

4.1 Introduction

This chapter describes the first application of the radiation module that we have developed, and which is discussed in Chapter 3 of this manuscript and in Colombo et al. (2019a).

In this chapter, we study the accretion onto CTTSs, and specifically the region where the accretion column hits the stellar surface. In particular, we study the effects of radiation, that emerges from shock-heated plasma in impact regions of CTTSs, on the structure of the pre-shock downfalling material. We investigate if a significant absorption of radiation occurs and if it leads to a pre-shock heating of the accreting gas.

Several HD and MHD models have been developed in order to study such impacts of accretion streams onto the surface of CTTSs. These models and the analysis of observations at different wavelengths show that impact regions can present complex structures and dynamics. The accretion columns themselves can be structured in density (Orlando et al. 2011; Matsakos et al. 2013; Bonito et al. 2014; Colombo et al. 2016, 2019c), so that post-shock regions may show a wide range of densities, temperatures, and velocities. As a result, different plasma components, both optically thin and optically thick, and emitting in different bands, co-exist.

In this scenario, reprocessing of radiation, through absorption and re-emission, is expected (Calvet & Gullbring 1998; Lamzin 1998; Reale et al. 2013; Bonito et al. 2014; Revet et al. 2017) and may lead to complex profiles of emission lines. Costa et al. (2017), using an iterative approach, proved that the radiation emerging from the post-shock region is absorbed by the pre-shock accreting material, leading to a pre-shock heating of the accretion column (a radiative precursor). More recently, de Sá et al. (2019) described accretion impacts in CTTSs with an approach interpolating between LTE and optically thin regimes, and hypothesized that a full non-LTE modeling of radiation effects might improve the description of the phenomenon.

In this work, we investigate the effects of radiation on the structure of the accreting gas through a HD model of accretion impacts which includes self-consistently, for the first time, the effects of both radiative losses and absorption of radiation by matter in a non-LTE regime. We present the results for a typical accretion column which produces detectable X-ray emission at its impact (Argiroffi et al. 2007; Sacco et al. 2010).

This chapter is structured as follows: in Sect. 4.2 we describe the physical model and the numerical setup; in Sect. 4.3 we show and discuss the results of the modeling; in Sect. 4.4 we draw our conclusion.

This work has been accepted for publication in Astronomy & Astrophysics (Colombo et al. 2019b).

4.2 The radiation hydrodynamics model

The model describes the impact of an accretion stream with density $n = 10^{11}$ cm^{-3} and temperature $T = 2 \times 10^4$ K onto the chromosphere of a CTTS[1]. Fig. 4.1 shows the initial density profile along the accretion column. The chromosphere is assumed to be isothermal with temperature $T = 10^4$ K. The accreting plasma initially is also in radiative equilibrium, flows along the z-axis, and impacts onto the chromosphere with a velocity of $u = 500$ km s^{-1}, perpendicularly to the stellar surface.

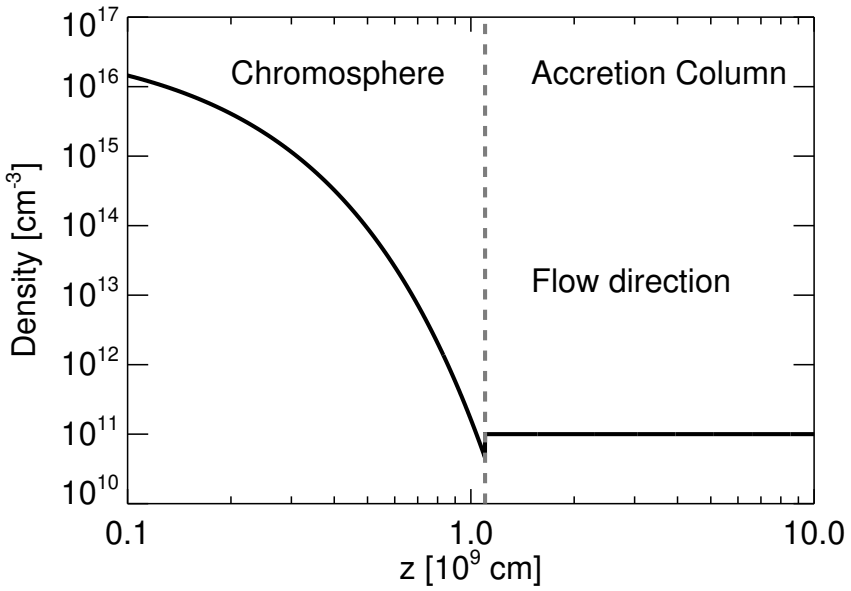

Figure 4.1 – Initial profile of density along the z-axis (in Log scale). The dashed grey line separates the chromosphere from the accretion column. The arrow shows the flow direction. Colombo et al. (2019b).

The model takes into account the gravity field g of the star, the thermal conduction F_c (including the classical and saturated regime as described in Colombo et al. 2016), the radiative losses L and the radiative gains. The model solves the time-dependent equations of conservation of mass, momentum and energy using the perfect gas equation of state

[1]Since the temperature of the pre-shock accreting gas is not constrained by observations, here we adopt the minimum temperature for which the opacities are defined (in look-up tables; see later in the text). Nevertheless, in photoionized plasmas, we expect that the opacities at lower temperatures (down to 10^3 K) are comparable with those at $T = 2 \times 10^4$ K (Marigo & Aringer 2009; Lykins et al. 2013).

$$\frac{\partial \rho}{\partial t} + \nabla \cdot (\rho \mathbf{u}) = 0 \tag{4.1}$$

$$\frac{\partial \rho \mathbf{u}}{\partial t} + \nabla \cdot (\rho \mathbf{u}\mathbf{u}) + \nabla p = \rho \mathbf{g} + \frac{\rho k_R}{c}\mathbf{F} \tag{4.2}$$

$$\frac{\partial (\mathbb{E} + \frac{1\rho \mathbf{u}^2}{2})}{\partial t} + \nabla \cdot [(\mathbb{E} + \frac{1\rho \mathbf{u}^2}{2} + p)\mathbf{u}] = \rho \mathbf{u} \cdot \mathbf{g} - \nabla \cdot \mathbf{F_c} + \frac{\rho k_R}{c}\mathbf{F} \cdot \mathbf{u} - L + k_P \rho c E \tag{4.3}$$

$$\frac{\partial E}{\partial t} + \nabla \cdot \mathbf{F} = L - k_P \rho c E \tag{4.4}$$

$$p = (\gamma - 1)\mathbb{E} = \rho \frac{k_B T}{\mu m_H} \qquad \mathbf{F} = -\lambda \frac{c}{k_R \rho} \nabla E \tag{4.5}$$

where ρ is the plasma mass density, k_R and k_P are, respectively, the Rosseland and Planck mean opacities, c the speed of light, $\mathbf{F}$ the comoving-frame radiation flux, $\mathbb{E}$ the internal plasma energy density, E the comoving-frame radiation energy, k_B the Boltzmann constant, T the plasma temperature, μ the mean particle weight (assuming solar abundances), m_H the hydrogen mass, λ the flux-limiter (Minerbo 1978), and $\gamma = 5/3$ the ratio of specific heats. In Chapter 3 we discussed the assumptions and the limits of these equations (see also Colombo et al. 2019a). The radiative calculations are not carried out in the chromosphere (i.e., $k_P = k_R = 0$ and $L = 0$ in Eqs. 1-4).

The calculations are performed using PLUTO (Mignone et al. 2007), a modular, Godunov-type parallel code for astrophysical plasma. The HD equations are solved using the HD module available in PLUTO for the linearized Roe Riemann solver based on characteristic decomposition of the Roe matrix (Roe 1981). We use second order method for the spatial reconstruction. The time evolution is solved using a second order Runge-Kutta method. The thermal conduction is treated with the super-time-stepping method (Alexiades et al. 1996). We use the monotonized central difference limiter.

The radiation effects are calculated by coupling PLUTO with a radiation module which was originally restrained to the LTE regime (Kolb et al. 2013), and which we have extended in order to take into account the non-LTE conditions. In Chapter 3, we describe the details of the implementation and the limits and assumptions of the new numerical module. The radiation quantities (k_P, k_R, L) are calculated at the temperature and density of interest using look-up tables (Rodríguez et al. 2018 see Chapter 3) and a bi-linear interpolation method. The radiation module makes use of the "Portable, Extensible Toolkit for Scientific Computation" (PETSc) library to solve the radiative part of the system (Balay et al. 2012). In particular, the PETSc library uses the Krylov subspace iterative method and a preconditioner to solve the matrix equation. For this work, the generalized minimal residual as iterative method and block Jacobi as preconditioner are used.

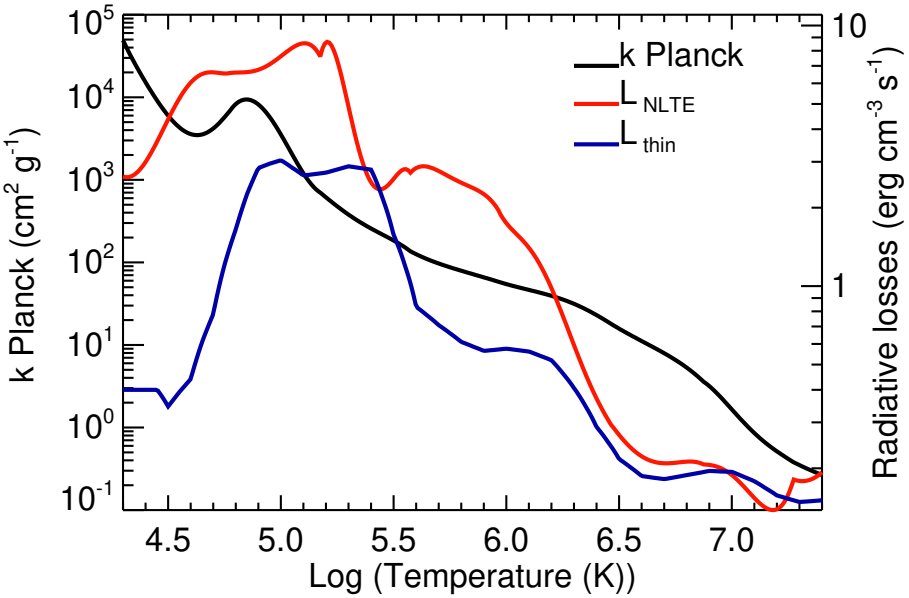

Figure 4.2 – Planck opacity (k_P, black) and radiative losses in non-LTE (L_{NLTE}, red) at the density of the accretion column (i.e., $n = 10^{11}$ cm^{-3}) versus temperature. For comparison, the figure shows also the radiative losses from optically thin plasma (L_{thin}, blue) used in models available in literature (e.g. Sacco et al. 2008). Colombo et al. (2019b).

We considered a non-LTE regime and used the frequency integrated approach, in which the radiation quantities k_P, k_R and L and radiation energy equation are integrated over all frequencies from 0 to ∞ (Rodríguez et al. 2018). As an example, Fig. 4.2 shows the value of k_P and L calculated at the density of the pre-shock accretion column (namely $n = 10^{11}$ cm^{-3}). In Sect. 3.2, we discuss the limits of our approach.

The radiation module works only in 3D (Kolb et al. 2013). To reduce the computational cost, we assume that the gas flows along the z-axis and that the domain consists of a 3D Cartesian grid with 3 cells for the x- and y-axes and 9048 cells for the z-axis (so the model can be considered as 1D). In other words, the model describes the flow dynamics along the axis of an accretion stream. The x- and y-axes are both covered with a uniform grid extending for 1.4×10^7cm. Along the z-axis, the grid is non-uniform and composed of 2 patches. The first covers the domain between 10^8 cm and 2×10^9 cm (thus fully including the chromosphere which extends up to 1.1×10^9 cm) with a uniform grid with spatial resolution of $\approx 9.7 \times 10^5$ cm (2048 cells); the second patch covers the domain between 2×10^9 cm and 10^{10} cm with a stretched grid, with a minimum spatial resolution of $\approx 9.7 \times 10^5$ cm close to the first patch, and a maximum spatial resolution of $\approx 13 \times 10^5$ cm at the end of the domain (7000 cells). The choice of this grid provides the best compromise between accuracy and efficiency of the calculation and allows to treat accurately the effects of thermal instability in the post-shock region. The bottom ($-z$) and top ($+z$) boundaries are fixed: the first to values

consistent with the chromosphere and the second to values describing an inflow of material with constant density, velocity and radiation energy, the latter chosen in such a way that the material is in radiative equilibrium with it. We set the lateral boundaries as periodic for both radiation and hydrodynamic quantities.

We present two simulations. The first one (run RHD) describes the impact of the accretion column, taking into account all the effects described above. The second one (run HD) describes the same impact, but in the optically thin regime, namely using the radiative losses adopted by Sacco et al. (2008) (see Fig. 4.2) and without radiative absorption; this simulation produces results analogous to those of previous models (e.g. Sacco et al. 2008, 2010), and it is used for comparison with run RHD to highlight the effects of absorption.

4.3 Results

4.3.1 Dynamics of the post-shock plasma

We follow the evolution of the system for $\approx$ 6 ks. Fig. 4.3 shows the space-time maps of density and temperature for the whole evolution of run RHD. Initially the accretion column hits the chromosphere with a speed of 500 km s^{-1} and sinks deeply onto the chromosphere, down to the position at which the ram pressure of the downflowing material equals the thermal pressure of the chromosphere. Then a shock develops at the base of the accretion column. The dynamics of the post-shock plasma is analogous in the two runs considered and to that of previous HD models that do not consider the effects of absorption of radiation (e.g. Sacco et al. 2008, 2010). The shock propagates upward through the accretion column (expanding phase), heating the plasma up to temperatures of a few million degrees and generating a hot and dense post-shock region (slab) that extends up to $\approx 2 \times 10^9$ cm (light blue regions in the top panel and yellow to orange regions in the bottom panel of Fig. 4.3). During the expansion of the post-shock, the density increases at the base of the slab due to accumulation of the accreting material. As a consequence, the radiative losses in that region rise. The expanding phase ends when the radiative losses in the slab reach a critical value that triggers the formation of cooling structures due to thermal instability. The plasma rapidly cools down at the base of the slab, its pressure decreases, and the slab is not able to sustain the material above. As a result, the region collapses (collapse phase). After the collapse, a new shock forms due to the continuous downflow and a new slab expands until it collapses under the action of radiative losses. The result of this evolution is shown in Fig. 4.3, where the alternating phases of expansion and collapse of the post-shock region are clearly visible.

4.3.2 Effects of radiation

The effects of radiation are evident in the pre-shock downflowing plasma. Fig. 4.4 shows the vertical profiles of temperature and density for the two runs considered, during one of the expansion phases. The temperature profile in run RHD presents two main features: the

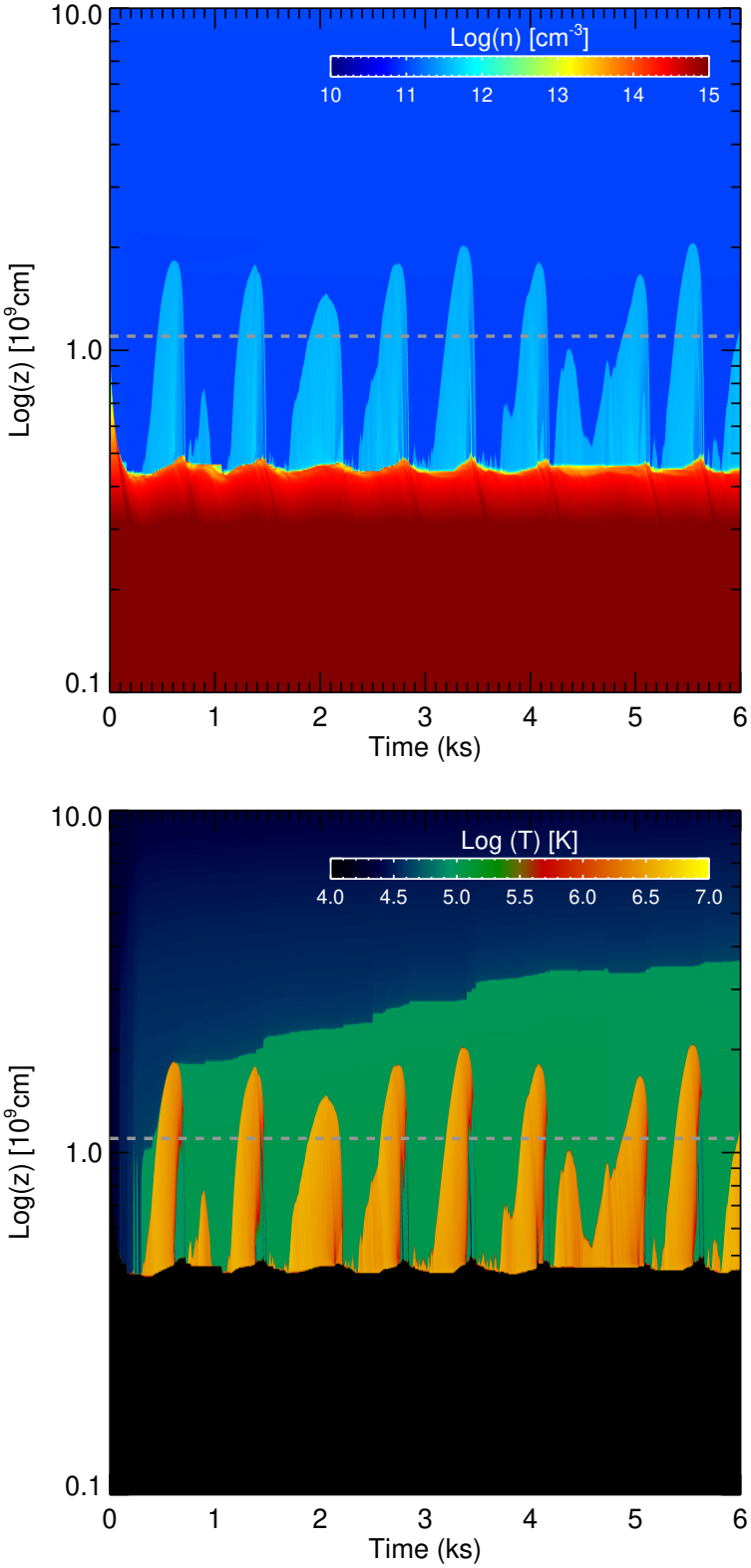

Figure 4.3 – Space-time maps, in logarithmic scale, of density (top panel, cm^{-3}) and temperature (bottom panel, K) for run RHD. The green region in the bottom panel corresponds to the hottest part of the precursor. The grey dotted lines in both panels mark the pre-impact position of the chromosphere. Colombo et al. (2019b).

hot post-shock with $T \approx 3$ MK located between $z = 0.5 \times 10^9$ cm and $z = 2 \times 10^9$ cm (present also in run HD and in previous HD models with no radiation effects included), and a precursor region with temperature ranging between 2×10^4 K and 10^5 K (up to $z = 10^{10}$ cm). The radiative precursor of the shock is not present in run HD (see bottom panel in Fig. 4.4) nor in previous HD models. In the density profile, the post-shock slab with a density a factor of 4 larger than that of the pre-shock material is clearly visible (as expected from the strong shock conditions Zel'dovich & Raizer 1967). Table 4.1 resumes the main physical properties of the pre-shock and post-shock region for runs HD and RHD.

Table 4.1 – Physical properties of the pre-shock and post-shock (ps) regions in runs RHD and HD.

Run	$n_{ps}(cm^{-3})$	$T_{ps}(K)$	$T_{\text{pre-shock}}(K)$	Max Extension$_{ps}$ cm
RHD	$\approx 4 \times 10^{11}$	$\approx 3 \times 10^6$	$\approx 10^5$	$\approx 2 \times 10^9$
HD	$\approx 4 \times 10^{11}$	$\approx 5 \times 10^6$	$\approx 2 \times 10^4$	$\approx 2.5 \times 10^9$

The precursor is the result of irradiation of the pre-shock material by the post-shock plasma (see 4.3.4). Since the pre-shock accreting material is optically thick, we found that it absorbs $\approx 70\%$ of radiation immediately above the slab at an height of $z = 4 \times 10^9$ cm from the chromosphere and heats up to maximum temperatures around 10^5 K (see Fig. 4.3).

We observe that the precursor is structured in temperature. After the early transient phase, i.e, when the hot part of the precursor does not evolve any more ($t > 3.5$ ks), the whole precursor in run RHD extends up to the limit of the domain at $z = 10^{10}$ cm. During the downflow, the accreting material (with an initial temperature of $T = 2 \times 10^4$ K) absorbs part of the radiation from the slab and, as a result, is gradually heated up to $T \approx 6 \times 10^4$ K at $z \approx 4 \times 10^9$ cm. At this point, an additional heating determines a sudden increase of temperature up to values around 10^5 K (see upper panel of Fig. 4.4). This is due to a peak in absorption of radiation by matter around $T \approx 7 \times 10^4$ K. In fact, at this temperature, the absorbed radiation energy, defined as $(k_P \rho c E)$ (see Eq. 4.3) has a maximum due to the peak in k_P (see Fig. 4.2), which generates the increase in the gas temperature.

After the heating at $z \approx 4 \times 10^9$ cm, the accreting material continues to fall with temperature around 10^5 K until it is shocked. We note that, at this temperature, the radiative losses have a maximum (see Fig. 4.2) that prevents the material to heat up more. The peak in absorption around $T = 7 \times 10^4$ K is due to helium (see Rodríguez et al. 2018) which, therefore, plays a critical role in determining the structure of the radiative precursor (see 4.3.5).

As mentioned before, we are using a frequency-integrated (or total) approach, and this may have some effects on the structure of the flow. However, Vaytet et al. (2013) performed simulations of stationary radiative shocks in Xenon, related to laboratory experiments (Bouquet et al. 2004), using a multigroup RHD scheme, and proved that such an approach, in comparison to the total approach, predicts the existence of the precursor but with larger size ($\approx 10\%$). We are, therefore, confident that the results presented here may change quantita-

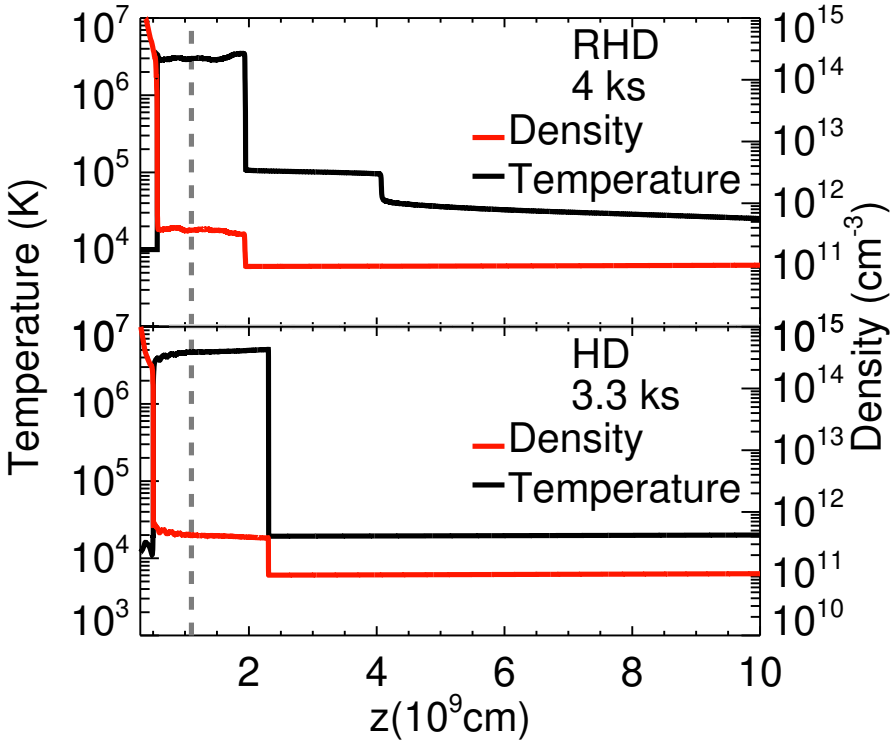

Figure 4.4 – Typical temperature (black line) and density (red line) profiles for runs RHD (top panel) and HD (bottom panel), during one of the expanding phases. The grey dotted line marks the initial position of the chromosphere. Colombo et al. (2019b).

tively but not qualitatively if a multigroup RHD scheme is adopted.

4.3.3 DISTRIBUTION OF EMISSION MEASURE VERSUS TEMPERATURE

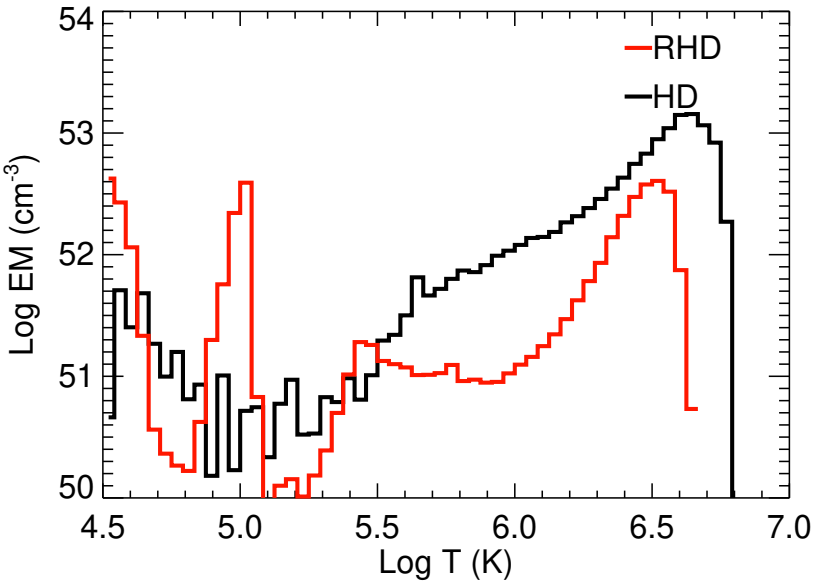

Figure 4.5 – EM synthesized from runs RHD (red histogram) and HD (black) versus temperature. Colombo et al. (2019b).

From the models, we derive the time-averaged distributions of emission measure versus temperature ($EM = \int_V n^2 dV$) which is useful to obtain information about the plasma components emitting at various temperatures. The distributions are derived by following the approach described by Colombo et al. (2016), assuming a stream with a mass accretion rate of $10^{-9.17}$ $M_\odot$ yr^{-1} as for TW Hya (e.g. Curran et al. 2011). This would require a column with a reasonable radius $r_s \approx 3.5 \times 10^{10}$ cm. Fig. 4.5 compares the distributions synthesized from runs RHD and HD to highlight the effects of radiation. The most striking difference between the two distributions is that the EM of RHD (red histogram in Fig. 4.5) shows three main peaks at $\log T = 4.5$, 5.0 and 6.5, whereas the EM of HD (black histogram in Fig. 4.5) has a prominent peak at $\log T = 6.6$ and a small peak at $\log T = 4.7$. The origin of the peaks in the EM of run RHD can be investigated by considering the bottom panel of Fig. 4.3. The orange regions in the figure mark the plasma with $\log T > 6$, belonging to the hot slab. Thus, the highest temperature peak in the two models considered is clearly due to the post-shock plasma of the slab. This peak is shifted at slightly lower temperatures and lower emission measure values in run RHD due to the radiative losses which are more efficient in run RHD than in HD (see Fig. 4.2).

The other two peaks at lower temperatures in the EM distribution of run RHD originate from blue and green regions in the bottom panel of Fig. 4.3 which mark the plasma with $4.5 < \log T < 4.8$ and $4.8 < \log T < 5.3$, respectively. These regions identify the precursor in run RHD: the peak at $\log T \approx 5$ in the EM distribution corresponds to the hottest part of the precursor. This feature is not present in run HD.

In addition, the EM distributions have a different slope in the region between $5.5 < \log T < 6.0$, again due to the differences in the radiative losses adopted in the two models (see Fig. 4.2). The EM of RHD shows also a small bump between $\log T = 5.3$ and $\log T = 5.9$ not present in run HD. This feature originates from the plasma cooling during the collapse phase (red regions in Fig.4.3) and is due to absorption of radiation by this plasma component.

4.3.4 Irradiation from the base of the slab

After its formation, the precursor region remains hot at temperatures $T \approx 10^5$ K for the entire simulation, and it seems not to be affected by the oscillations of the post-shock region.

We estimate the cooling time for the precursor and found that it needs $\approx$ 60 s to cool down to 10^4 K, i.e. a shorter time compared to the slab oscillations ($\approx$ 500 s. See Fig. 4.3.). The fact that the precursor does not follow the post-shock dynamics is an indication that the post-shock is not the only source of irradiation.

The region responsible to sustain the precursor during the whole simulation is the base of the slab. This region is very dense ($n \approx 10^{12}\mathrm{cm}^{-3}$) and remains hot, due to the shock, almost for the entire simulation (see Fig.4.3). Due to the high density, the radiative losses in this region are very high, and this results in a strong emission. The radiation energy arising from that region is able to sustain the precursor.

4.3.5 Role of helium in determining the precursor

To highlight the role played by helium in the absorption of radiation, we consider a simulation identical to run RHD but using a modified version of the opacity tables, where the helium effects are not taken into account (run RHD-He).

Fig.4.6 is analogous to Fig. 4.4 and shows the temperature and density profiles for the run RHD-He. In run RHD-He a precursor forms as in run RHD. However, at odds with run RHD, the downflowing plasma gradually increases its temperature, reaching a maximum temperature of 5×10^4 K before being shocked, and no sudden increase of temperature is present. We conclude, therefore, that helium is responsible for the high temperatures of the precursor in run RHD through the peak in k_P at $\log T = 4.8$ (See Fig. 4.2) that determines a sudden increase of absorption.

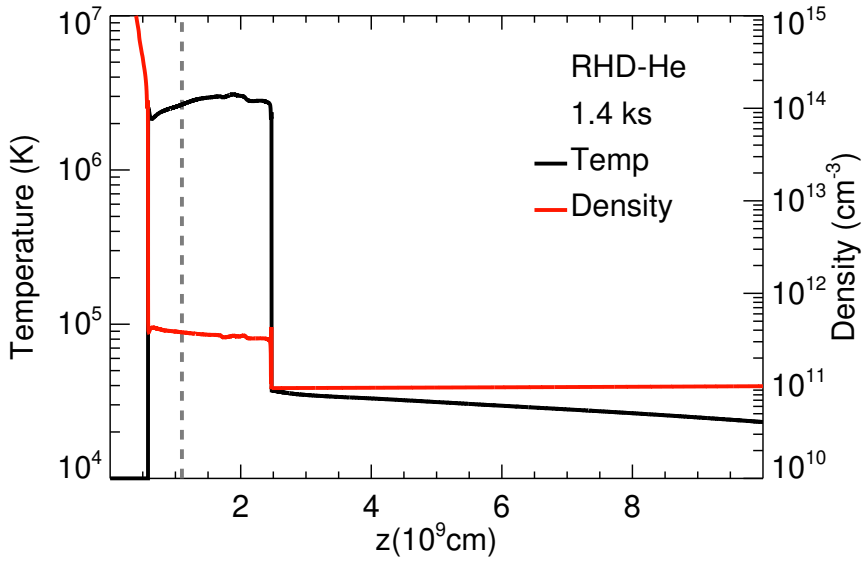

Figure 4.6 – Temperature (black line) and density (red line) profiles for the run RHD-He, during the expanding phase. The grey dotted line represents the initial position of the chromosphere. Colombo et al. (2019b).

4.4 Conclusions

We have developed a model which describes the radiation effects in the non-LTE regime during the impact of an accretion column onto the surface of a CTTS. Our model shows that a significant fraction ($\approx 70\%$ at a distance of 4×10^9 cm from the chromosphere) of radiation produced in the post-shock plasma is absorbed by the pre-shock material of the accretion column. As a result, this material is heated up to temperature of the order of 10^5 K, forming a radiative precursor. The precursor reaches the highest temperature in proximity of the shock. At $z \approx 4 \times 10^9$ cm, the temperature of the precursor decreases to values between 2×10^4 K and 5×10^4 K. The precursor is a strong source of UV emission. The partial absorption of X-ray emission from the slab and the contribution of UV emission from the precursor may explain why accretion rates derived from UV observations are systematically larger than accretion rates inferred from X-ray observations (Curran et al. 2011). In future works, we will extend the analysis by exploring the parameter space of the model with the aim of investigating how the structure and evolution of the radiative precursor depend on the physical conditions (density, downflow velocity, abundance) of the accretion stream.

CHAPTER 5

Conclusions and future prospects

5.1 Summary and Conclusions

Understanding the way CTTSs interact with their circumstellar disks and how they exchange mass and angular momentum is of crucial importance to investigate the star formation process and the formation of planetary systems.

The purpose of my PhD project was to study mass accretion processes in CTTSs, considering both the large scale star-disk interaction, evaluating the accreting plasma dynamics, and the small scale interaction, in the region where the disk material hits the stellar surface. In particular, we studied if a coronal activity characterized by intense flares on the disk surface, as the one commonly observed in CTTSs, is able to trigger accretion events (Colombo et al. 2019c). We also described the impacts of accretion columns onto the stellar surface, and studied the effects of irradiation from the post-shock plasma on the unshocked downfalling material in the accretion column (Colombo et al. 2019b). In this latter case, we developed a radiative module for the magnetohydrodynamic code PLUTO that handle a non-LTE regime (Colombo et al. 2019a). We validated it with several tests available in literature.

Our studies proved that an intense flaring activity is able to perturb the disk and to generate accretion phenomena comparable with those observed in CTTSs. As it concerns accretion impacts, we proved that the irradiation from the post-shock plasma is able to warm up the accretion column forming a precursor region that emits mainly in the UV band.

5.1.1 Effects of flaring activity on the disk stability

A relevant aspect for the accretion process in CTTSs and not fully explored up to date is the evidence of very energetic and frequent flares in these systems. In fact, flares may easily perturb the disk stability and possibly trigger accretion episodes as demonstrated by Orlando et al. (2011). In the framework of this PhD project, we investigated the effects of an intense flaring activity localized in proximity of the accretion disk of a CTTS (see Chapter 2). To this end, we developed a 3D MHD model describing a magnetized protostar surrounded by a Keplerian disk where flares with small-to-medium intensity occur.

Our model shows that the flares heat the plasma in the inner region of the disk up to temperatures of the order of tens millions degrees. Part of this hot plasma is channeled in hot loops that link the inner part of the disk to the protostar. The remaining part is poorly confined by the magnetic field and escapes from the system, carrying away mass and angular momentum. All the hot material, either confined in loops or escaping from the protostar, forms a tenuous hot corona extending from the central star to the inner part of the disk.

The flaring activity strongly perturbs the disk dynamics. The overpressure waves generated by the flares travel through the disk and perturb its structure. As a result, the material is

pushed out from equilibrium and funneled by the magnetic field into accretion columns that accrete onto the star.

The dynamics of the accretion columns is affected by flares. For instance, a flare that occurs close to an accretion column may disrupt it or otherwise increase the amount of downfalling plasma. Due to this dynamics, the streams are highly inhomogeneous, with a complex density structure, and clumped.

These findings support the idea that the persistent low-level hour-timescale variability observed in CTTSs reflects the inner clumpiness of the accretion streams (Gullbring et al. 1996; Safier 1998; Bouvier et al. 2007; Giardino et al. 2007; Cranmer 2009; Alencar et al. 2018). Moreover, Espaillat et al. (2019) observed a correlation between the accretion events and the X-ray luminosity due to flaring activity, giving a first observational evidence of this phenomenon.

This study suggests the presence of a hot extended corona that radiates the disk of a CTTSs from above. The extended corona is a source of high energy radiation (X-Ray, UV) and may significantly contribute to the chemical evolution of the disk. Moreover, the radiation may increase the ionization level of the disk material, increasing the coupling between matter and magnetic field. As a result, this would enhance the effects of magneto-rotational instabilities in the disk. In addition to that, the hot corona may also affect the formation and evolution of protoplanets. The ionizing radiation may change the chemical composition of protoplanetary atmospheres, and, also, may generate photoevaporation processes.
A snapshot of the simulation is available online for outreach purposes at this link: `https://sketchfab.com/3d-models/a-star-is-born-aa3aa69e953f4f80903157e02bb10be5`

5.1.2 Effects of radiation on the impact region of a CTTS

The region where the accretion column hits the stellar surface presents complex structures in density and velocity. Several studies suggest that the absorption of radiation plays a critical role in the impact region (Costa et al. 2017; Revet et al. 2017; de Sá et al. 2019). In this work, we studied the effects of the irradiation from shock-heated material at the base of an accretion column on the unshocked downfalling material.

To this purpose, we extended a previous LTE radiation module (Kolb et al. 2013) already implemented in the PLUTO code in order to handle a non-LTE regime (see Chapter 3). Our module is coupled to a database of radiative quantities tabulated as functions of density and temperature: radiation emission, Plank mean opacity, and Rosseland mean opacity. Such a database was generated in a non-LTE approach that follows the CRSS model (Rodríguez et al. 2018). In particular, the radiative quantities recover the LTE values in appropriate plasma conditions (i.e. rather at high density). We tested our new implementation by comparing our results with semi-analytical solutions available in the literature. In particular, we performed a matter-coupling test in order to check the correctness of the implementation of the radiation equations. Then, we performed a simple shock test used to check the good implementation of the radiation module within the PLUTO environment. These tests agree with the nominal solutions with a discrepancy lower than 7%.

Using our non-LTE radiation module we modeled the interior of an accretion column hitting the chromosphere of a CTTS. We assumed a uniform flow with density of $n = 10^{11}\mathrm{cm}^{-3}$ and velocity

of 500km/s, the typical values for an accretion column which produces detectable X-ray emission at its impact (Argiroffi et al. 2007; Sacco et al. 2010). We found a radiative precursor in the downfalling material accreting onto the surface of a CTTS. We identify the origin of this precursor in the irradiation of the post-shock X-ray emitting plasma (see Chapter 4). The precursor is structured in temperature: the hottest part at temperature around 10^5 K is located just above the post-shock plasma. In fact, the model predicts that part of the radiation ($\approx$ 70%) arising from the post-region is absorbed by the pre-shock material of the accretion column. The radiative precursor is a strong source of UV emission.

The partial absorption of X-ray emission from the slab and the contribution of UV emission from the precursor may explain why accretion rates derived from UV observations are systematically larger than those inferred from the X-ray band. In fact, in the radiation HD scenario the amount of UV emission produced by the accretion column is larger than the one emitted in the pure HD case. Moreover, this new scenario may suggest the origin of strong Doppler shifts observed in UV lines (Ardila et al. 2013): the dynamics of the precursor region has to be considered in the interpretation of UV line profiles.

5.2 Future prospects

The studies presented in this thesis allowed us, on the one hand, to investigate the role played by flares in perturbing the stability of accretion disks around CTTSs, and, possibly, in triggering accretion episodes, on the other hand, to study the radiation-matter interaction in regions where accretion columns hit the stellar surface.

A future improvement of our 3D MHD model of CTTSs that we plan to perform is to use a more realistic initial magnetic field configuration, that takes into account the rotational evolution of the system and the twisting and expansion of the field lines driven by the differential rotation of the disk. Such a complex magnetic field configuration is expected to change the dynamics of the accretion streams, leading to a more complex pattern of accretion.

As it concerns the flares, these have been included artificially in the model by prescribing random releases of energy in proximity of the disk surface. Future simulations should take into account self-consistently the development of flares as a result of magnetic reconnection episodes that might occur close to the disk surface because of the differential rotation of the disk. For the new model it will be necessary to add the resistivity effects in the calculation, and to consider high spatial resolution in order to describe properly the effects of the resistivity (Reale et al. 2016). To speed up the calculation we plan to run first a 2.5D model, without including the effects of resistivity, until the magnetic field configuration becomes more realistic. Then, we will map the 2.5D domain in a full 3D domain, and we will run the simulation including the resistivity effects. We expect to observe flares emerging naturally due to magnetic reconnection driven by the disk dynamics.

Concerning the modeling of the impact region, an important follow-up study is the exploration of the model parameter space to investigate how density, impact velocity and metallicity of the accretion column determine the structure of the impact region. As it concerns the density, on the one hand, a denser accretion column would produce a thinner post-shock region (Sacco et al. 2010), but on the other hand, the post-shock material would be denser and, as a consequence, would emit more radiation. A the same time, a denser accretion column absorbs more radiation arising from the impact region, and this may produce a strong UV-emitting precursor. The other important parameter to

take into account is the impact velocity. It is usually assumed that the accretion column hits the stellar surface at free fall velocity, so this parameter can not vary in a large range such as the density (Sacco et al. 2010). However, as showed in literature (e.g. Sacco et al. 2008, 2010) the post-shock temperature depends on the square of the velocity, so that even small variations have important consequences on the structure of the post-shock region. In particular, a *slow* accretion column ($\mathbf{u} = 300$km/s) would produce a cold post-shock region that would not emit in the X-rays. On the contrary, a *fast* accretion column ($\mathbf{u} = 600$km/s) would generate a hot post-shock that would emit in the X-rays. Thus, the downfalling velocity determines the temperature and emission of the post-shock plasma and, therefore, the structure of the radiative precursor in the pre-shock accretion column. In Chapter 4 we showed the importance of the role played by helium in the formation of the precursor region, in general we expect that metallicity plays a role in determining the Plank and Rosseland opacities and the radiative losses. We expect that higher metallicity will increase the absorption, but also the radiative losses of the plasma.

Another further improvement in the modeling of accretion impacts with radiation effects could be the introduction of the magnetic field. As shown by Orlando et al. (2010, 2013) the different strengths and topologies of the magnetic fields impact significantly the extension and the location of the post-shock region. So we expect that the strength and topology of the magnetic field may play an important role also in the determination of the existence, the location, and the shape of the precursor region. For example, a post-shock located high in the accretion column due to the magnetic field topology (Orlando et al. 2013) would generate two precursor regions, one above and one below, with different velocities and extensions.

In the near future, it will be important to synthesize spectral signatures emitted by our models. This is of paramount importance to develop a diagnostic tool that links the observations to our scenarios of accretion. Future studies could be devoted to synthesize spectral emission from our simulated accretion structures, using a 3D radiative transfer code in non-LTE regimes. We plan to use the new version of the IRIS code (see Ibgui et al. 2013) which is currently under development.

CHAPTER 6

Appendix

6.1 Role of the author

This manuscript follows from a collaboration between different research teams, as it involves several aspects of radiation HD and MHD simulations.

The work was done within a tight collaboration between 3 groups.

The LERMA team (Laboratoire d'Etudes du Rayonnement et de la Matière en Astrophysique et Atmosphères), at the Sorbonne campus Pierre et Marie Curie in Paris (France), was dedicated to the radiation effects in HD simulations. Within the group: Laurent Ibgui and Chantal Stéhle (my French supervisors).

The INAF (Istituto Nazionale di AstroFisica) group at the astronomical observatory of Palermo (Italy) was dedicated to the developing of HD and MHD setups and to the comparison of the results from the simulations with the observations. Within the team: Salvatore Orlando (my Italian supervisor), Fabio Reale, Giovanni Peres, Costanza Argiroffi and Sara Bonito.

The group leaded by Rafael Rodriguez at Universidad de las Palmas de Gran Canaria at Canary Island (Spain) was dedicated to the synthesis of optical properties of plasma. They provided us the look-up tables with the radiative powerlosses and Plank and Rosseland opacities of the plasma in non-LTE regime.

My PhD was a joint supervision between Sorbonne in France, and Università di Palermo in Italy. During my period in Italy I have worked closely with Salvatore Orlando to develop the HD and MHD setups. I have also developed the tools used to analyze the simulations. During my period in Paris, I have worked closely with Laurent Ibgui, and under the supervision of Chantal Stéhle, to develop the radiation HD module implemented in the PLUTO code, and the radiation HD simulations of impact regions. We worked also with Matthias González who helped us for the correct implementation of the non-LTE equations and for the interpretation of the non-LTE radiation hydrodynamic simulations.

Part of my work was also dedicated to the analysis and interpretation of the results obtained from the models; this and the link with observations were discussed with the LERMA and INAF teams together.

6.2 Experience

Local Organizing Committee of the conference: "Radiative signatures from the cosmos. A meeting in honor of Ivan Hubeny", 23-26 October 2018, Paris, France.

6.2.1 Scientific Publications

- Colombo, S.; Orlando, S.; Peres, G.; Reale, F.; Argiroffi, C.; Bonito, R.; Ibgui, L.; Stehlé, C., "New view of the corona of classical T Tauri stars: Effects of flaring activiy in circumstellar disks". Published in Astronomy & Astrophysics, Volume 624, id.A50, 12 pp. April 2019.

- Colombo, S.; Ibgui, L.; Orlando, S.; Rodriguez, R.; Espinosa, G.; Gonzàlez, M.; Stehlé, C.; Peres, G., "Non-LTE radiation hydrodynamics in PLUTO". Accepted for publication in Astronomy & Astrophysics, July 2019.

- Colombo S.; Ibgui, L.; Orlando, S.; Rodriguez, R.; Espinosa, G.; Gonzàlez, M.; Stehlé, C.; de Sà, L.; Argiroffi, C.; Bonito, R.; Peres, G., "Effects of radiation in accretion regions of classical T Tauri stars: pre-heating of accretion column in non-LTE regime". Accepted for publication in Astronomy & Astrophysics. August 2019.

- Colombo, S.; Ibgui, L.; Orlando, S.; Rodriguez, R.; González, M.; Stehlé, C.; de Sá, L., "Radiation Effects on Impact of Accretion Streams in Classical T Tauri Stars". In Radiative Signatures from the Cosmos, ASP Conference Series, Vol. 519, Proceedings of a conference held 23-26 October, 2018 at Sorbonne University, Paris, France. Edited by K. Werner, C. Stehle, T. Rauch, and T. Lanz. San Francisco: Astronomical Society of the Pacific, 2019, p.299.

- de Sá, L.; Stehlé, C.; Chièze, J.-P.; Hubeny, I.; Lanz, T.; Colombo, S.; Cayatte, V.; Ibgui, L.; Orlando, S., "Radiation Feedback in Accretion Shocks on Young Stars". In Radiative Signatures from the Cosmos, ASP Conference Series, Vol. 519, Proceedings of a conference held 23-26 October, 2018 at Sorbonne University, Paris, France. Edited by K. Werner, C. Stehle, T. Rauch, and T. Lanz. San Francisco: Astronomical Society of the Pacific, 2019, p.281.

- Ibgui, L; Hubeny, I.; Lanz, T.; González, M.; Stehlé, C.; Orlando, S.; Colombo, S., "3D Spectral Radiative Transfer and Perspectives for Spectroscopic Diagnostics". In Radiative Signatures from the Cosmos, ASP Conference Series, Vol. 519, Proceedings of a conference held 23-26 October, 2018 at Sorbonne University, Paris, France. Edited by K. Werner, C. Stehle, T. Rauch, and T. Lanz. San Francisco: Astronomical Society of the Pacific, 2019, p.21.

- Orlando, S.; Argiroffi, C.; Bonito, R.; Colombo, S.; Peres, G.; Reale, F.; Miceli, M.; Ibgui, L.; Stehlé, C.; Matsakos, T., "Mass Accretion Impacts in Classical T Tauri Stars: A Multidisciplinary Approach". In JET Simulations, Experiments, and Theory, Astrophysics and Space Science Proceedings, Volume 55. ISBN 978-3-030-14127-1. Springer Nature Switzerland AG, 2019, p. 43.

- Colombo, S.; Ibgui, L.; Rodriguez, R.; Orlando, S.; González, M.; Stehlé, C.; De Sá, L., "Radiation Magnetohydrodynamic Models and Spectral Signatures of Plasma Flows Accreting onto Classical T Tauri Stars". In JET Simulations, Experiments, and Theory, Astrophysics and Space Science Proceedings, Volume 55. ISBN 978-3-030-14127-1. Springer Nature Switzerland AG, 2019, p. 37.

- de Sá, L.; Stehlé, C.; Chièze, J. P.; Hubeny, I.; Lanz, T.; Colombo, S.; Ibgui, L.; Orlando, S., "Modelling the Accretion on Young Stars, Recent Results and Perspectives". In JET Simulations, Experiments, and Theory, Astrophysics and Space Science Proceedings, Volume 55. ISBN 978-3-030-14127-1. Springer Nature Switzerland AG, 2019, p. 29.

- Colombo, S.; Ibgui, L.; Orlando, S.; Rodriguez, R.; González, M.; Stehlé, C.; de, Sa L. "Radiative hydrodynamic models of accretion streams in Classical T Tauri Stars". SF2A-2018: Proceed-

ings of the Annual meeting of the French Society of Astronomy and Astrophysics. Eds.: P. Di Matteo, F. Billebaud, F. Herpin, N. Lagarde, J.-B. Marquette, A. Robin, O. Venot, pp.141-144.

- Colombo, S.; Orlando, S.; Peres, G.; Reale, F.; Argiroffi, C.; Bonito, R.; Ibgui, L.; Stehlé, C., "Flaring activity on the disk of Classical T Tauri Stars: effects on disk stability". SF2A-2018: Proceedings of the Annual meeting of the French Society of Astronomy and Astrophysics. Eds.: P. Di Matteo, F. Billebaud, F. Herpin, N. Lagarde, J.-B. Marquette, A. Robin, O. Venot, pp.121-123.

6.2.2 Schools

- XXIX Canary Islands Winter School of Astrophysics, La Laguna, Tenerife, Spain, 13-17 November 2017.

- Astrosim: Ecole numérique pour l'astrophysique, Hosted at center Blaise Pascal at ENS Lyon, Lyon, France, 26 June - 7 July 2017

6.2.3 Courses

- Seminars on star formation and exoplanets at INAF-Osservatorio Astronomico di Palermo. 2017.

- "Ethique de la recherche et intégrité scientifique: principes et pratique (IS)". Course for "Ethique et intégrité scientifique", Astronomie et Astrophysique d'Ile-de-France, Observatoire de Paris (France), April 2019.

- "Simulations numériques et calcul haute performance: Applications à l'hydrodynamique pour l'astrophysique". Course for "Formations scientifiques disciplinaires proposées par une école doctorale", Astronomie et Astrophysique d'Ile-de-France, Maison de la simulation - Commissariat à l'énergie atomique et aux énergies alternatives" (CEA), January 2018.

- French Course, Sorbonne - Campus Pierre et Marie Curie. 2018-2019.

6.2.4 Computing Resources Projects

- "Effects of intense flaring activity on accretion disk of Classical T Tauri Stars" Authors: S. Colombo. Proposal selected by the Italian SuperComputing Resource Allocation committee at CINECA (Italy)-INAF/Cineca HPC Resources 2017 First call - class B (2017).

- "3D MHD model of inclined accretion impacts in CTTSs : Effects on observability and perturbation of the surrounding stellar atmosphere." Authors: S. Colombo, S. Orlando, L. Ibgui, C.Stehle, C. Argiroffi, R. Bonito, G. Peres, F. Reale, A.Petralia. Proposal selected by the Italian SuperComputing Resource Allocation committee at CINECA (Italy)- class B (2017).

6.2.5 Funded Projects

- PLAS@PAR, Innovative research project call – 2017, title of the project : "New insights into the physics of accretion processes onto classical T Tauri stars : 3D MHD models, and inclusion of radiative transfer" team : Salvatore Colombo (100 % FTE),Laurent Ibgui(PI, 80 % FTE), Salvatore Orlando(Co-PI, 50% FTE), Stehlé Chantal (10%).
- Actions sur projets INSU - Appel d'offres 2018, title of the project: "Accretion processes onto classical T Tauri stars : 3D MHD models, exploration of radiative transfer effects; spectral signatures." team: Salvatore Colombo (100 % FTE),Laurent Ibgui(PI, 80% FTE), Salvatore Orlando(50% FTE), Stehlé Chantal (10%).
- Action fédératrice "étoile (AFE). Appel d'offre 2019. title of the project: " Influence of accretion conditions on the radiation feedback in flows impacting onto classical T Tauri stars". Team: Salvatore Colombo (PI), Laurent Ibgui, Chantal Stehlé, Salvatore Orlando, Rosaria Bonito.

6.2.6 Contributions at conferences

Talks

- Authors: S. Colombo, S. Orlando, F. Reale, C. Argiroffi, R. Bonito, L. Ibgui, C. Stehlé. Title: "Effects of intense coronal activity on the stability of disks of classical T Tauri stars", Invited talk at OrionLeiden, 2019, Leiden, Netherlands.
- Authors: S. Colombo, S. Orlando, F. Reale, C. Argiroffi, R. Bonito, L. Ibgui, C. Stehlé. Title: "Effects of intense coronal activity on the disk of a classical T Tauri star", EWASS, 2019, Lyon, France.
- Authors: S. Colombo, L. Ibgui, S. Orlando, R. Rodriguez, M. González, C. Stehlé. Title:" Radiative accretion shocks in classical T Tauri stars" - Zooming in on star formation, 2019, Nafplio, Greece.
- Authors: S. Colombo, S. Orlando, F. Reale, C. Argiroffi, R. Bonito, L. Ibgui, C. Stehlé. Title: "Effects of Intense Coronal Activity on the Disk of a Classical T Tauri Stars" - Star Planets Inner Disk Interaction (SPIDI) kick-off meeting, 2018, Grenoble, France.
- Authors: S. Colombo, L. Ibgui, S. Orlando, R. Rodriguez, M. González, C. Stehlé. Title: "Effects of Radiative Transfer in accretion impacts of Classical T Tauri Stars" - Accretion Atelier, 2018, Grenoble, France.
- Authors: S. Colombo, L. Ibgui, R. Rodriguez, S. Orlando, M. González, C. Stehlé, L. de Sá. Title: "Radiation magnetohydrodynamic models and spectral signatures of plasma flows accreting onto Classical T Tauri Stars" - JETSET FP6, "Jet Simulations, Experiments, Theory" 10 years later, what is next?, 2018, Meudon, France.
- Authors: S. Colombo, S. Orlando, L. Ibgui, C. Stehlé. Title: "Radiation MagnetoHydroDynamic Models and Spectral Signatures of Plasma Flows Accreting onto Young Stellar Objects " - LERMA pole 2 meeting, 2018, Observatoire de Paris, Paris, France.

- Authors: S. Colombo, L. Ibgui, S. Orlando, R. Rodriguez, M. González, C. Stehle, L. De Sá. Title: "Radiative hydrodynamic models of accretion streams in Classical T Tauri Stars". SF2A, 2018, Bordeaux, France.
- Authors: S. Colombo, S. Orlando, F. Reale, C. Argiroffi, R. Bonito, L. Ibgui, C. Stehlé. Title: "Flare-induced accretion events". SPIDI kik-off meeting, 2017, Montpellier, France.
- Authors: S. Colombo, S. Orlando, F. Reale, C. Argiroffi, R. Bonito, L. Ibgui, C. Stehlé. Title: "Effects of intense flaring activity on accretion disk of Classical T Tauri Stars". BCool 2017, Montpellier, France.

Posters

- Title: "Radiative effects on accretion shocks in classica T Tauri stars"; Authors: S. Colombo, L. Ibgui, S. Orlando, R. Rodriguez. M. Gonzàlez, C. Stehlé. EWASS, 2019, Lyon, France.
- Title: "Radiation effects on impact of accretion streams in Classical T - Tauri Stars"; Authors: S. Colombo, L. Ibgui, S. Orlando, R. Rodriguez, M. Gonzàlez, C. Stehlé, L. De Sà. Radiative signatures from the cosmos: A meeting in honor of Ivan Hubeny, 2018, Paris, France.
- Title: "Flaring activity on the disk of Classical T Tauri Stars: effects on disk stability"; Authors: S. Colombo, S. Orlando, G. Peres, F. Reale, A. Argiroffi, R. Bonito, L. Ibgui, C. Stehle. SF2A, 2018, Bordeaux, France.
- Title "Effects of intense flaring activities on the accretion disk of a classical T Tauri star"; Authors: S. Colombo, S. Orlando, G. Peres, F. Reale, L. Ibgui, C. Stehlé,C. Argiroffi, R. Bonito. XXIX Canary Islands Winter School of Astrophysics, 2017, La Laguna, Tenerife, Spain.

Aknowledgements

The completion of this project could not have been accomplished without the support of so many people that an entire thesis would not be enough to thanks them all.

I would like to express my special thanks of gratitude to my three supervisors. I cannot express enough thanks to Salvatore Orlando and Laurent Ibgui for their continued support and encouragement. Their expertise was invaluable and fundamental during all my PhD. I offer my sincere appreciation for the learning opportunities provided by them. I would like, also, to express my special thanks of gratitude to Chantal Stehlé for welcoming me into the French team and for her help and support during my PhD.

I would like to thank Rafael Rodriguez and Matthias González from which I have received a great deal of scientific support and assistance. I have to thanks also all the scientific team in OAPa for the useful discussions that considerably improve the scientific content of this project.

My heartfelt thanks to Annagrazia, Fiorella, Antonino, Riccardo, Valerio, Marta, Brisa, Maud, Mathilde and to all my parisian friends that sustained and support me more than they will ever imagine.They succeed in the hard task to make me feel at home in Paris. I will never stop to thank you all.

I am sorry for not Italian speakers but I have to thank my family and my Italian friends, so I will switch in Italian.

Non potró mai ringraziare abbastanza tutta la mia famiglia per avermi supportato (e sopportato!) durante questi 3 anni e per avermi permesso di studiare e raggiungere questo traguardo senza dovermi preoccupare di altro. Spero un giorno di potervi ripagare per tutto questo.

Un grazie va anche ai "Giampaoli", che nonostante la distanza mi hanno aiutato durante questi 3 anni regalandomi infinite risate e lunghe pause. Un grazie particolare a Jumpollo e Rex, il mio instacabile team di supporto tecnico e informatico.

Infine, il grazie più importante di tutti va alla mia ragazza, nonchè futura moglie, Alice: grazie per esserci sempre e per aver deciso di passare la tua vita insieme a me.

Bibliography

Alencar, S. H. P., Bouvier, J., Donati, J. F., et al. 2018, A&A, 620, A195

Alexiades, V., Amiez, G., & Gremaud, P. A. 1996, Communications in Numerical Methods in Engineering, 12, 31

Alme, M. L. & Wilson, J. R. 1973, ApJ, 186, 1015

Anders, E. & Grevesse, N. 1989, Acta, 53, 197

Andre, P. & Montmerle, T. 1994, ApJ, 420, 837

Ardila, D. R., Herczeg, G. J., Gregory, S. G., et al. 2013, ApJS, 207, 1

Argiroffi, C., Maggio, A., & Peres, G. 2007, A&A, 465, L5

Asplund, M., Grevesse, N., Sauval, A. J., & Scott, P. 2009, ARA&A, 47, 481

Aubert, D. & Teyssier, R. 2008, MNRAS, 387, 295

Audard, M., Briggs, K. R., Grosso, N., et al. 2007, A&A, 468, 379

Balay, S., Abhyankar, S., Adams, M. F., et al. 2012, PETSc Users Manual, Tech. Rep. ANL-95/11 - Revision 3.3, Argonne National Laboratory

Balbus, S. A. 2003, ARA&A, 41, 555

Balbus, S. A. & Hawley, J. F. 1991, ApJ, 376, 214

Balbus, S. A. & Hawley, J. F. 1998, Reviews of Modern Physics, 70, 1

Balsara, D. S. & Spicer, D. S. 1999, Journal of Computational Physics, 149, 270

Barbera, E., Orlando, S., & Peres, G. 2017, A&A, 600, A105

Bauche, J., Bauche-Arnoult,, C., & Klapisch, M. 1987, Advances in Atomic and Molecular Physics, 23, 131

Beloborodov, A. M. 1999, ApJ, 510, L123

Bertout, C., Basri, G., & Bouvier, J. 1988, ApJ, 330, 350

Bessolaz, N., Zanni, C., Ferreira, J., Keppens, R., & Bouvier, J. 2008, A&A, 478, 155

Blinova, A. A., Romanova, M. M., & Lovelace, R. V. E. 2016, MNRAS, 459, 2354

Bonito, R., Orlando, S., Argiroffi, C., et al. 2014, ApJ, 795, L34

Bonito, R., Orlando, S., Peres, G., Favata, F., & Rosner, R. 2007, A&A, 462, 645

Borkowski, K. J., Shull, J. M., & McKee, C. F. 1989, ApJ, 336, 979

Boss, A. P. 1997, Science, 276, 1836

Bouquet, S., Stéhlé, C., Koenig, M., et al. 2004, Physical Review Letters, 92, 225001

Bouvier, J., Alencar, S. H. P., Harries, T. J., Johns-Krull, C. M., & Romanova, M. M. 2007, Protostars and Planets V, 479

Brickhouse, N. S., Cranmer, S. R., Dupree, A. K., Luna, G. J. M., & Wolk, S. 2010, ApJ, 710, 1835

Bruch, A. 2015, A&A, 579, A50

Calvet, N. & Gullbring, E. 1998, ApJ, 509, 802

Castor, J. I. 2004, Radiation Hydrodynamics (Cambridge University Press), 368

Colombo, S., Ibgui, L., Orlando, S., et al. 2019a, A&A, accepted for publication

Colombo, S., Ibgui, L., Orlando, S., et al. 2019b, A&A, accepted for publication

Colombo, S., Orlando, S., Peres, G., Argiroffi, C., & Reale, F. 2016, A&A, 594, A93

Colombo, S., Orlando, S., Peres, G., et al. 2019c, A&A, 624, A50

Commerçon, B., Hennebelle, P., & Henning, T. 2011a, ApJ, 742, L9

Commerçon, B., Teyssier, R., Audit, E., Hennebelle, P., & Chabrier, G. 2011b, A&A, 529, A35

Costa, G., Orlando, S., Peres, G., Argiroffi, C., & Bonito, R. 2017, A&A, 597, A1

Cowie, L. L. & McKee, C. F. 1977, ApJ, 211, 135

Cranmer, S. R. 2009, ApJ, 706, 824

Curran, R. L., Argiroffi, C., Sacco, G. G., et al. 2011, A&A, 526, A104

Dalton, W. W. & Balbus, S. A. 1993, ApJ, 404, 625

Davis, S. W., Stone, J. M., & Jiang, Y.-F. 2012, ApJS, 199, 9

de Sá, L., Chièze, J.-P., Stehlé, C., et al. 2019, arXiv e-prints, arXiv:1904.09156

Dimitrijevic, M. S. & Konjevic, N. 1987, A&A, 172, 345

Donati, J.-F., Gregory, S. G., Montmerle, T., et al. 2011, MNRAS, 417, 1747

Donati, J.-F., Jardine, M. M., Gregory, S. G., et al. 2007, MNRAS, 380, 1297

Drake, J. J., Ercolano, B., Flaccomio, E., & Micela, G. 2009, ApJ, 699, L35

Dubroca, B. & Feugeas, J. 1999, Academie des Sciences Paris Comptes Rendus Serie Sciences Mathematiques, 329, 915

Edwards, S., Hartigan, P., Ghandour, L., & Andrulis, C. 1994, AJ, 108, 1056

Ensman, L. 1994, ApJ, 424, 275

Espaillat, C. C., Robinson, C., Grant, S., & Reynolds, M. 2019, ApJ, 876, 121

Espinosa, G., Rodríguez, R., Gil, J. M., et al. 2017, Phys. Rev. E, 95, 033201

Fadeyev, Y. A., Le Coroller, H., & Gillet, D. 2002, A&A, 392, 735

Favata, F., Flaccomio, E., Reale, F., et al. 2005, ApJS, 160, 469

Favata, F. & Micela, G. 2003, Space Sci. Rev., 108, 577

Feigelson, E. D. & Montmerle, T. 1999, ARA&A, 37, 363

Flaccomio, E., Micela, G., & Sciortino, S. 2003, A&A, 402, 277

Flock, M., Fromang, S., González, M., & Commerçon, B. 2013, A&A, 560, A43

Gehmeyr, M. & Mihalas, D. 1994, Physica D Nonlinear Phenomena, 77, 320

Getman, K. V., Feigelson, E. D., Broos, P. S., Micela, G., & Garmire, G. P. 2008a, ApJ, 688, 418

Getman, K. V., Feigelson, E. D., Grosso, N., et al. 2005, ApJS, 160, 353

Getman, K. V., Feigelson, E. D., Micela, G., et al. 2008b, ApJ, 688, 437

Giardino, G., Favata, F., Pillitteri, I., et al. 2007, A&A, 475, 891

Giuliani, Jr., J. L. 1984, ApJ, 277, 605

Gnedin, N. Y. & Abel, T. 2001, New A., 6, 437

González, M., Audit, E., & Huynh, P. 2007, A&A, 464, 429

González, M., Vaytet, N., Commerçon, B., & Masson, J. 2015, A&A, 578, A12

Goodson, A. P., Böhm, K.-H., & Winglee, R. M. 1999, ApJ, 524, 142

Goodson, A. P., Winglee, R. M., & Böhm, K.-H. 1997, ApJ, 489, 199

Gregory, S. G. & Donati, J.-F. 2011, Astronomische Nachrichten, 332, 1027

Gregory, S. G., Jardine, M., Gray, C. G., & Donati, J.-F. 2010, Reports on Progress in Physics, 73, 126901

Gregory, S. G., Wood, K., & Jardine, M. 2007, MNRAS, 379, L35

Griem, H. 1997, Principles of Plasma Spectroscopy (Cambridge University Press, Cambridge)

Gu, M. F. 2008, Canadian Journal of Physics, 86, 675

Gullbring, E., Barwig, H., Chen, P. S., Gahm, G. F., & Bao, M. X. 1996, A&A, 307, 791

Günther, H. M., Schmitt, J. H. M. M., Robrade, J., & Liefke, C. 2007, A&A, 466, 1111

Hartmann, L., Herczeg, G., & Calvet, N. 2016, ARA&A, 54, 135

Hayashi, M. R., Shibata, K., & Matsumoto, R. 1996, ApJ, 468, L37

Hayes, J. C. & Norman, M. L. 2003, ApJS, 147, 197

Hellier, C. 2001, Cataclysmic Variable Stars, Springer Praxis Books/Space Exploration (Springer)

Herczeg, G. J. & Hillenbrand, L. A. 2008, ApJ, 681, 594

Hirose, S., Uchida, Y., Shibata, K., & Matsumoto, R. 1997, Pub. Astron. Soc., 49, 193

Horne, K. & Stiening, R. F. 1985, MNRAS, 216, 933

Hubeny, I. & Burrows, A. 2007, ApJ, 659, 1458

Hubeny, I. & Mihalas, D. 2014, Theory of Stellar Atmospheres (Princeton University Press)

Ibgui, L., Hubeny, I., Lanz, T., & Stehlé, C. 2013, A&A, 549, A126

Jardine, M., Collier Cameron, A., Donati, J.-F., Gregory, S. G., & Wood, K. 2006, MNRAS, 367, 917

Jiang, Y.-F., Stone, J. M., & Davis, S. W. 2012, ApJS, 199, 14

Kashyap, V. L. & Drake, J. J. 2000, in Bulletin of the American Astronomical Society, Vol. 32, AAS/High Energy Astrophysics Division #5, 1227

Kastner, J. H., Huenemoerder, D. P., Schulz, N. S., Canizares, C. R., & Weintraub, D. A. 2002, ApJ, 567, 434

Klapisch, M. & Busquet, M. 2013, New Journal of Physics, 15, 015012

Klassen, M., Kuiper, R., Pudritz, R. E., et al. 2014, ApJ, 797, 4

Kley, W. 1989, A&A, 208, 98

Kley, W., Bitsch, B., & Klahr, H. 2009, A&A, 506, 971

Koenigl, A. 1991, ApJ, 370, L39

Kolb, S. M., Stute, M., Kley, W., & Mignone, A. 2013, A&A, 559, A80

Koldoba, A. V., Romanova, M. M., Ustyugova, G. V., & Lovelace, R. V. E. 2002, ApJ, 576, L53

Koldoba, A. V., Ustyugova, G. V., Romanova, M. M., & Lovelace, R. V. E. 2008, mnras, 388, 357

Kramers, H. A. 1923, The London, Edinburgh, and Dublin Philosophical Magazine and Journal of Science, 46, 836

Krumholz, M. R., Klein, R. I., McKee, C. F., & Bolstad, J. 2007, ApJ, 667, 626

Kulkarni, A. K. & Romanova, M. M. 2005, ApJ, 633, 349

Kulkarni, A. K. & Romanova, M. M. 2008, MNRAS, 386, 673

Kulkarni, A. K. & Romanova, M. M. 2009, MNRAS, 398, 701

Lada, C. J. 1987, in IAU Symposium, Vol. 115, Star Forming Regions, ed. M. Peimbert & J. Jugaku, 1

Lamzin, S. A. 1998, Astronomy Reports, 42, 322

Levermore, C. D. 1984, J. Quant. Spec. Radiat. Transf., 31, 149

Levermore, C. D. & Pomraning, G. C. 1981, ApJ, 248, 321

Long, M., Romanova, M. M., Kulkarni, A. K., & Donati, J.-F. 2011, MNRAS, 413, 1061

Long, M., Romanova, M. M., & Lovelace, R. V. E. 2005, ApJ, 634, 1214

Long, M., Romanova, M. M., & Lovelace, R. V. E. 2008, MNRAS, 386, 1274

López-Santiago, J., Crespo-Chacón, I., Flaccomio, E., et al. 2016, A&A, 590, A7

Lotz, W. 1968, Zeitschrift für Physik, 216, 241

Lykins, M. L., Ferland, G. J., Porter, R. L., et al. 2013, MNRAS, 429, 3133

Malzac, J., Beloborodov, A. M., & Poutanen, J. 2001, MNRAS, 326, 417

Marigo, P. & Aringer, B. 2009, A&A, 508, 1539

Matsakos, T., Chièze, J.-P., Stehlé, C., et al. 2013, A&A, 557, A69

McKee, C. F. & Ostriker, E. C. 2007, ARA&A, 45, 565

Melon Fuksman, J. D. & Mignone, A. 2019, arXiv e-prints, arXiv:1903.10456

Mignone, A., Bodo, G., Massaglia, S., et al. 2007, ApJS, 170, 228

Mignone, A., Zanni, C., Tzeferacos, P., et al. 2012, ApJS, 198, 7

Mihalas, D. & Auer, L. H. 2001, J. Quant. Spec. Radiat. Transf., 71, 61

Mihalas, D. & Klein, R. I. 1982, Journal of Computational Physics, 46, 97

Mihalas, D. & Mihalas, B. W. 1984, Foundations of radiation hydrodynamics (New York, Oxford University Press)

Miller, K. A. & Stone, J. M. 2000, ApJ, 534, 398

Minerbo, G. N. 1978, J. Quant. Spec. Radiat. Transf., 20, 541

Munier, A. & Weaver, R. 1986, Computer Physics Reports, 3, 165

Neuhaeuser, R., Sterzik, M. F., Schmitt, J. H. M. M., Wichmann, R., & Krautter, J. 1995, A&A, 297, 391

Orlando, S., Bocchino, F., Reale, F., Peres, G., & Pagano, P. 2008, ApJ, 678, 274

Orlando, S., Bonito, R., Argiroffi, C., et al. 2013, A&A, 559, A127

Orlando, S., Reale, F., Peres, G., & Mignone, A. 2011, MNRAS, 415, 3380

Orlando, S., Sacco, G. G., Argiroffi, C., et al. 2010, A&A, 510, A71

Pomraning, G. C. 1973, The equations of radiation hydrodynamics (Oxford: Pergamon Press)

Powell, K. G., Roe, P. L., Linde, T. J., Gombosi, T. I., & de Zeeuw, D. L. 1999, Journal of Computational Physics, 154, 284

Preibisch, T., Kim, Y.-C., Favata, F., et al. 2005, ApJS, 160, 401

Reale, F. 2003, Advances in Space Research, 32, 1057

Reale, F., Bocchino, F., & Peres, G. 2002, A&A, 383, 952

Reale, F., Lopez-Santiago, J., Flaccomio, E., Petralia, A., & Sciortino, S. 2018, ApJ, 856, 51

Reale, F., Orlando, S., Guarrasi, M., et al. 2016, ApJ, 830, 21

Reale, F., Orlando, S., Testa, P., et al. 2013, Science, 341, 251

Reale, F., Peres, G., Serio, S., Rosner, R., & Schmitt, J. H. M. M. 1988, ApJ, 328, 256

Revet, G., Chen, S. N., Bonito, R., et al. 2017, Science Advances, 3, no.11, e1700982

Rodríguez, R., Espinosa, G., & Gil, J. M. 2018, Phys. Rev. E, 98, 033213

Rodríguez, R., Florido, R., Gil, J., et al. 2008, Laser and Particle Beams, 26, 433–448

Rodríguez, R., Florido, R., Gil, J., et al. 2010, Commun. Comput. Phys, 8, 185

Roe, P. 1981, Journal of Computational Physics, 43, 357

Romanova, M. M., Kulkarni, A. K., & Lovelace, R. V. E. 2008, ApJ, 673, L171

Romanova, M. M., Long, M., Lamb, F. K., Kulkarni, A. K., & Donati, J.-F. 2011a, MNRAS, 411, 915

Romanova, M. M., Ustyugova, G. V., Koldoba, A. V., & Lovelace, R. V. E. 2002, ApJ, 578, 420

Romanova, M. M., Ustyugova, G. V., Koldoba, A. V., & Lovelace, R. V. E. 2004a, ApJ, 616, L151

Romanova, M. M., Ustyugova, G. V., Koldoba, A. V., & Lovelace, R. V. E. 2004b, ApJ, 610, 920

Romanova, M. M., Ustyugova, G. V., Koldoba, A. V., & Lovelace, R. V. E. 2005, ApJ, 635, L165

Romanova, M. M., Ustyugova, G. V., Koldoba, A. V., & Lovelace, R. V. E. 2011b, MNRAS, 416, 416

Romanova, M. M., Ustyugova, G. V., Koldoba, A. V., & Lovelace, R. V. E. 2012, MNRAS, 421, 63

Romanova, M. M., Ustyugova, G. V., Koldoba, A. V., Wick, J. V., & Lovelace, R. V. E. 2003, ApJ, 595, 1009

Rosdahl, J., Blaizot, J., Aubert, D., Stranex, T., & Teyssier, R. 2013, MNRAS, 436, 2188

Rose, S. J. 1992, Journal of Physics B: Atomic, Molecular and Optical Physics, 25, 1667

Rutten, R. J. 1995, Radiative Transfer in Stellar Atmospheres (Lecture Notes Utrecht University)

Sacco, G. G., Argiroffi, C., Orlando, S., et al. 2008, A&A, 491, L17

Sacco, G. G., Orlando, S., Argiroffi, C., et al. 2010, A&A, 522, A55

Safier, P. N. 1998, ApJ, 494, 336

Shakura, N. I. & Sunyaev, R. A. 1973, A&A, 24, 337

Shu, F. H., Shang, H., Glassgold, A. E., & Lee, T. 1997, Science, 277, 1475

Skinner, M. A., Dolence, J. C., Burrows, A., Radice, D., & Vartanyan, D. 2019, ApJS, 241, 7

Skinner, M. A. & Ostriker, E. C. 2013, ApJS, 206, 21

Spitzer, L. 1962, Physics of Fully Ionized Gases (New York: Wiley)

Stassun, K. G., Ardila, D. R., Barsony, M., Basri, G., & Mathieu, R. D. 2004, AJ, 127, 3537

Stewart, J. C. & Pyatt, Jr., K. D. 1966, ApJ, 144, 1203

Stone, J. M., Mihalas, D., & Norman, M. L. 1992, ApJS, 80, 819

Swesty, F. D. & Myra, E. S. 2009, ApJS, 181, 1

Tanaka, T. 1994, Journal of Computational Physics, 111, 381

Turner, N. J. & Stone, J. M. 2001, ApJS, 135, 95

van der Holst, B., Tóth, G., Sokolov, I. V., et al. 2011, ApJS, 194, 23

van Regemorter, H. 1962, ApJ, 136, 906

Vaytet, N., González, M., Audit, E., & Chabrier, G. 2013, J. Quant. Spec. Radiat. Transf., 125, 105

von Rekowski, B. & Brandenburg, A. 2004, A&A, 420, 17

Zanni, C. & Ferreira, J. 2009, A&A, 508, 1117

Zanni, C. & Ferreira, J. 2013, A&A, 550, A99

Zel'dovich, Y. B. & Raizer, Y. P. 1967, Physics of shock waves and high-temperature hydrodynamic phenomena (New York: Academic Press, 1966/1967, edited by Hayes, W.D.; Probstein, Ronald F.)

Zhang, W., Howell, L., Almgren, A., Burrows, A., & Bell, J. 2011, ApJS, 196, 20

Zhang, W., Howell, L., Almgren, A., et al. 2013, ApJS, 204, 7